NONLOCAL CONTINUUM MECHANICS AND DAMAGE PREDICTION IN SOLIDS

A Dissertation

by

PARISA KHODABAKHSHI

Submitted to the Office of Graduate and Professional Studies of
Texas A&M University
in partial fulfillment of the requirements for the degree of

DOCTOR OF PHILOSOPHY

Chair of Committee,	J.N. Reddy
Co-Chair of Committee,	Arun Srinivasa
Committee Members,	Mary Beth Hueste
	Anastasia Muliana
Head of Department,	Robin Autenrieth

December 2018

Major Subject: Civil Engineering

ABSTRACT

In this study a new computational framework by the name Graph-based Finite Element Approach (GraFEA) is developed for the study of fracture in solids. Conventional finite element method (FEM) is without doubt the most widely-used computational method in the field of solids and structures. However, in its conventional form it is not well-suited for the study of discontinuous displacement fields (e.g. fracture problems). Several remedies have been proposed in the literature, but the amount of complexity of these approaches limits and negatively impacts their integration into the commercial softwares. GraFEA on the other hand builds upon the robustness of conventional FEM, and it can be incorporated into the existing commercial softwares with minor effort. The two distinct features of GraFEA which make it an appealing choice for the study of fracture are:

1. Transformation of the conventional FEM into a nonlocal network: The goal of this transformation is to derive the forces and strains along the edges of the elements of the discretized continuum instead of determining them at the nodes. The network representation resembles the truss network to some extent, with the exception that the force along an edge of interest depends on the collective behavior of the strains along the neighboring edges of the edge of interest, and not only the strain along the edge of interest. Hence, the resulting network is not local as in a simple truss network.

2. Imposition of a nonlocal edge-based fracture criterion: The network representation allows us to study fracture on the discretized body instead of using a continuum approach. This treatment of failure is as simple as that of lattice models without suffering from the limited Poisson's ratio of 0.25. The nonlocal edge-based fracture criterion is motivated by the idea of weakest link statistics. In this approach, the nonlocal edge-based strain (or force) is compared with a critical value to determine whether the edge is broken or not. The nonlocal edge-based strain is the weighted-averaged value of the strain over a characteristic zone

mirrored along the edge of interest. Depending on the relative size of the characteristic zone and the elements, the nonlocal fracture criterion can turn into a local criterion (no averaging required).

The network representation of GraFEA is a reformulation of conventional FEM, and it simplifies to FEM for an intact medium. Progression of fracture is studied by incrementally increasing the values of the imposed boundary conditions, and monitoring the breakage of the edges.

DEDICATION

To my parents, Parivash and Ali Akbar,

for their unconditional love and support.

ACKNOWLEDGMENTS

I would like to express my sincere gratitude towards my advisor Professor J. N. Reddy for his guidance, support and mentoring throughout my dissertation. His passion towards research, and teaching has always motivated me to excel myself in both aspects. I cherished every meeting and the educational discussions we had. I would like to take this moment to thank Professor Reddy and his wife to consider us as family, and to welcome us to their home every now and then. It meant a lot to me as an international student living away from my family.

I would also like to thank my co–advisor, Professor A. R. Srinivasa for his support, and guidance. His inputs and suggestions made the path smoother, and it also helped me gain better insight into my area of research. I appreciate every meeting that I had with him which helped me to become a better researcher over time. I also thank Drs. Hueste and Muliana for serving on my dissertation advisory committee and providing me constructive comments. I would also like to thank Dr. Goenezen for serving as the substitute for Dr. Muliana on my defense date.

I would like to thank all my colleagues in the Advanced Computational Mechanics Laboratory. The discussions we had during our weekly group meetings have been very helpful for me. I would like to especially thank Dr. Michael Powell for helping me with the computer cluster in the Advanced Computational Mechanics Laboratory.

Finally, I would like to express my deep gratitude towards my parents, and my brothers for their love, support, and encouragement. Without their support I would not have been able to accomplish whatever I have to this day. I would like to thank my parents for bringing me up with the mindset of working hard, and believing in what I do.

CONTRIBUTORS AND FUNDING SOURCES

Contributors

This work was supported by a dissertation committee consisting of Professor J. N. Reddy (as the advisor), Professor Arun R. Srinivas (as the co–advisor), Professor Anastasia Muliana (as the member) of the Department of Mechanical Engineering, and Professor Mary Beth Hueste (as the member) of the Department of Civil Engineering.

All other work conducted for the dissertation was completed by the student independently.

Funding Sources

Financial support for this research was provided by Oscar S. Wyatt Endowed Chair from the Department of Mechanical Engineering at Texas A&M University, the Graduate Teaching Fellowship from the College of Engineering at Texas A&M University, and the Graduate Teaching Assistantship from the College of Engineering at Texas A&M University.

TABLE OF CONTENTS

Page

LIST OF FIGURES

FIGURE Page

LIST OF TABLES

1. INTRODUCTION

1.1 Fracture in Solids

The study of fracture in solids has gained the attention of many researchers since the seminal work of Griffith [1]. Several theoretical and experimental studies on brittle and ductile fracture of solids have been reported in the literature since then. Given the amount of uncertainties involved fracture mechanics is a complicated area of study, however, the level of complexity is even higher for brittle materials. One major issue with brittle materials is the dispersion of the fracture stress for different specimen size [2]. The scatter in fracture stress is more prominent for brittle materials [3, 4] as compared to ductile materials which undergo plastic deformation. As a result, the ability to predict and study initiation and propagation of fracture in brittle materials is more difficult.

Several methods have been proposed in the literature on the study of fracture and damage in solids. However, the existing methods suffer from shortcomings which limit their use in engineering applications. In general, the existing methods can be categorized into two groups, namely continuum-based approaches and bond-breakage approaches.

1. *Continuum-based approaches*: The strength point of this group of methods, which are based on continuum mechanics, is in the ability to incorporate FEM as a powerful computational framework. The significant methods in this category are continuum damage mechanics, extended finite element method (XFEM), and interelement crack method[1]. Continuum damage mechanics [5, 6] studies damage within materials by the introduction of a damage variable and its evolution law; and it does not deal with continuum separation and crack growth in a direct way. The interelement crack method [7, 8] adds a traction-displacement constitutive equation across the boundaries of the elements for the study of fracture. The major drawback of the interelement crack method is the limitation enforced on the crack path, that is the crack can only grow across the boundaries of the elements. Consequently, the results from the interelement

[1] Sometimes referred to as cohesive zone models. Since cohesive zone models are also used in other method (such as extended finite element method, this name can be misleading.

crack method are mesh dependent. XFEM [9–11], on the other hand, enriches the continuum with jump discontinuity functions, and it uses linear elastic fracture mechanics (LEFM) to study crack propagation. The main shortcomings of XFEM is the stress singularity induced by LEFM. Despite complying with the field equations, the singular stress field violates some of the underlying assumptions of the theory of elasticity (refer to the review paper by Sinclair [12]).

2. *Bond-breakage approaches*: These methods (including lattice models and bond-based peridynamic theory [13]) are based on a discrete representation of the continuum by replacing it with a set of links and nodes similar to a generalized truss network. Fracture is then introduced by breakage of the bonds. Despite the ease of introduction of fracture in these methods, they suffer from a major limitation in terms of modeling the material properties. The bond-breakage methods are not able to model even a simple continuum properly. A lattice network of two-force members is limited to a Poisson's ratio of 0.25 [14].

1.2 Motivation and Scope for the Present Study

The question to be answered in this dissertation is whether a new computational framework can be introduced to keep the best features of the above-mentioned approaches, while avoiding their limitations. To be specific, we want to answer whether we can retain the robustness of classical FEM, and still be able to employ the simplicity of the fracture criterion used in lattice models. The graph-based finite element approach (GraFEA) is a promising answer to this question [15]. In order to build GraFEA two existing ideas in the literature have been utilized.

GraFEA aims to reformulate the conventional FEM in the form of a nonlocal network using the idea introduced by Reddy and Srinivasa [16]. For any hyperelastic material, the displacement-based FEM can be written in terms of the strains along the edges of the elements [16]. The nodal forces are also shown to be directed along the edges of the elements and they can be written in terms of the edge-directed strains. Reddy and Srinivasa [16] proved that a network representation of FEM is possible; however, GraFEA is the first study on numerical implementation of the idea. This representation of conventional FEM makes it suitable for the integration of discrete edge-

based fracture criterion. The network representation of GraFEA, which consists only of nodes and the distance between them, appears similar to a local truss network. The main difference between the two lies in the locality of the forces. In a truss network the force along an edge only depends on the relative distance of the two end nodes (strain along that edge). Whereas in GraFEA, the force along edge i does not only depend on the strain along that edge, but on the collective behavior of the strain along the set of edges in the elements sharing edge i. Consequently, the force along the edges has a nonlocal sense in GraFEA, as opposed to the local forces in a truss network. This is the reason why the Poisson's ratio for the nonlocal network of GraFEA is not limited to 0.25, as is for bond-breakage approaches.

Considering the noticeable dispersion in the fracture stress of brittle materials, the use of only a single parameter, i.e. the fracture toughness (K_{Ic}), as the fracture criterion cannot provide us with reliable results for these materials. Weibull [17] proposed a statistical model to account for the dispersion of fracture stress for different specimen size. In Weibull's model, the continuum is divided into elements, each with a known probability of failure. The survival probability of the continuum is the product of the probability of survival of all elements. When the size of the elements becomes very small, the product will turn into an integral, and Weibull's equation is achieved. The elements can be thought of as links of a chain [18, 19], and the weakest link governs the strength of the continuum. This led to the birth of the theory of weakest link statistics.

Ritchie, Knott, and Rice [20] showed that for a brittle type of material (cleavage fracture in mild steel at very low temperatures) fracture does not only depend on the stress at the tip of the crack, but on the average stress over a characteristic distance ahead of the crack tip. This is a nonlocal approach to the study of crack growth (named as RKR criterion in [20])) where the value of the critical parameter, whether it be the strain or the stress, is averaged over a zone and not considered at a point. Ritchie, Knott, and Rice [20] also showed that the fracture toughness, K_{Ic}, resulting from employing this fracture criterion is compatible with those derived from experiments at low temperatures given a characteristic distance of two grain diameters. Later, Lin, Evans, and Ricthie [21] studied brittle fracture of steel by augmenting the RKR nonlocal damage criterion

with the weakest link statistics. In summary, the idea was that if the characteristic zone is chosen large enough to guarantee the existence of flaws, fracture propagates when the local stress in the characteristic region exceeds the critical value σ_f.

The idea of weakest link statistics is used as the motivation to introduce a nonlocal fracture criterion into the nonlocal network of GraFEA. The graph-based representation of the continuum allows for the implementation of a fracture criterion similar to what is done for conventional truss networks. In this approach an edge is considered broken if the averaged edge-directed strain over a characteristic zone exceeds a critical value. Depending on the mesh density this criterion can introduce high level of nonlocality (where the strain is averaged over a large number of elements), or it can simplify to a local criterion where only the strain along one edge is considered. The introduced integral type nonlocal criterion is shown to eliminate the mesh dependency induced by strain localization.

The proposed approach has a number of good features as compared to the existing methods. Since GraFEA is a reformulation of conventional FEM, it can build upon the robustness of FEM, and can be easily integrated into already existing commercial FEM softwares. Therefore, one need not start from scratch. In addition, the discrete approach of GraFEA to fracture circumvents the need for dealing with the incorporation of a discontinuity into a continuum. Finally, GraFEA has the ability to incorporate probabilistic methods to provide a contour of damage probability as opposed to deterministic approaches with a definite crack path (e.g. XFEM). Due to the level of uncertainty involved (geometry, material properties, etc.), this is a more realistic approach to the study of damage and fracture.

1.3 Objectives

The following items are identified as the objectives of this dissertation:

1. *Construction of the network representation of GraFEA from conventional FEM*: In this study, the theoretical basis for GraFEA is constructed in two steps. First, the network formulation for an arbitrary linear triangular element in a plane elasticity condition is determined. It is shown that in the case of no damage this network formulation will yield the same results as

conventional FEM. This study is the first numerical implementation of the idea proposed by Reddy and Srinivasa [16].

2. *Integration of an edge-based local fracture criterion into the network representation*: A local fracture variable is integrated into GraFEA by imposing a strain-based criterion over the edges. The effect of the edge-based fracture criterion on the stiffness matrix is observed. For a damaged continuum the results of GraFEA will no longer be similar to conventional FEM for an undamaged material. It is shown through force-displacement relations that the brittle type fracture in this study will cause an abrupt changes in the force-carrying capacity of the continuum, causing a sharp decrease in the tangent modulus.

3. *Implementation of nonlocality in the fracture criterion*: The fracture criterion is upgraded to an integral-type nonlocal criterion with the introduction of a length scale parameter. The difference between the nonlocality of the fracture criterion and the one from the reformulation of FEM is discussed. It is shown that the introduction of a length scale parameter in the fracture criterion will result in a diffuse damage in addition to the fracture along a certain path.

4. *Studying the effect of the length scale parameter on mesh dependency*: It is shown that the results from the local fracture criterion show mesh dependency caused by the strain softening behavior for the brittle fracture. In other words, the peak force that can be carried continues decreasing by further mesh refinement. The effect of the nonlocal fracture criterion in eliminating the above-mentioned mesh dependency is evaluated through a set of numerical results.

1.4 Organization of the Text

The rest of the dissertation is organized as follows. In Chapter 2, the nonlocal network representation of GraFEA is constructed for the case of a discretized medium consisting of linear triangular elements. Utilizing a local fracture criterion, numerical examples are provided to demonstrate the capability of GraFEA in studying fracture in solids. In Chapter 3, the local fracture criterion used in the original formulation of GraFEA is updated to a nonlocal fracture criterion, and its effect on the numerical results is studied. It is shown that the introduction of a nonlocality in the fracture

criterion will eliminate the mesh dependency caused by strain localization in fracture. Chapter 4 and Chapter 5 are two other projects which I worked on during my doctoral studies giving me a better insight in choosing the proper measure for resolving the issue of mesh dependency of GraFEA. In Chapter 4 a unified integro-differential nonlocal model is introduced for the study of size-dependent features. In this regard the tw-phase integro-differential form of Eringen nonlocal model [22] is revisited by using a new Kernel function for the integral part. The formulation is derived for a general three-dimensional problem, and then simplified to the case of one-dimensional Euler-Bernoulli beam. It is shown that the proposed model settles the paradoxical case of cantilever beams for the differential form of Eringen model. In Chapter 5 a micro-structure dependent unified beam theory with the von Kármán nonlinearity is introduced. The size dependent features are taken into account using the classical strain gradient theory. The unified beam theory includes three familiar beam theories (namely Euler-Bernoulli beam theory, Timoshenko beam theory, and third-order Reddy beam theory) as special cases. The individual and combined effects of nonlinearity, nonlocality, and shear strains are studied. Finally, Chapter 6 summarizes the concluding remarks and lists the suggestions for future studies.

2. GRAFEA: A GRAPH–BASED FINITE ELEMENT APPROACH FOR STUDY OF DAMAGE AND FRACTURE IN BRITTLE MATERIALS*

2.1 Introduction

2.1.1 Damage and Failure

Given the importance of predicting structural integrity and failure, and the fact that the conventional finite element method (FEM) is without doubt the most widely–used computational framework in the field of solid and structural mechanics, the ability to integrate damage and fracture into conventional FEM is of great importance. Since the seminal work of Griffith [1], and its extensions and clarifications [23–29] that continue to this day in the mechanics literature, there has been much work done in the area of brittle fracture to gain insight into the fracture process both experimentally and theoretically. This has led to various criteria that have made their way into handbooks (e.g., for example, [30]), which can be used to design for individual cracks. Nevertheless, the ability to *simulate* the growth of multiple cracks for the purpose of large scale design evaluations (especially for the purposes of impact and blast protection for example) has been a great challenge. On one hand, the physics of local fracture processes are extremely complicated and reach down to atomic length scales. On the other hand, the result of a fracture fundamentally alters the topology of the body, making it a challenging simulation problem.

In spite of these difficulties, the engineering significance of the problem is such that two drastically different approaches have been developed to provide engineers with a tool for the evaluation of structures:

1. Continuum–based models (including continuum damage mechanics, extended finite element methods, cohesive zone models)

2. Bond–breakage models (including lattice models and peridynamics)

*Reprinted with permission from "GraFEA: A Graph–based Finite Element Approach for the Study of Damage and Fracture in Brittle Materials" by P. Khodabakhshi, J. N. Reddy, and A. R. Srinivasa, 2016. *Meccanica*, 51(12), 3129–3147, Copyright 2016 by Springer.

2.1.1.1 Continuum–based models

Continuum damage mechanics (CDM) [5, 6, 31–34], replaces the actual fracture and material separation with a diffuse "damage" variable (which can be scalar, vector or tensorial), and evolution equations are provided for this variable. This allows for a modified plasticity–like model that can be implemented in FEM, but does not actually show crack growth, only "damage zones". This has also been extended to nonlocal approaches (see e.g. [35]).

In contrast to CDM, there exists a different approach that is based on the incorporation of fracture criteria directly into a discrete formulation of the problem and in this approach material separation is included. The most common versions of these being the extended finite element method –XFEM (refer to [9–11, 36]), and cohesive zone models.

The core idea of XFEM is to enrich the local polynomial approximations in classical FEM with non–smooth functions that are chosen to incorporate jumps, discontinuities or other local phenomena. Depending upon whether these special functions complement or replace the regular FEM interpolations, we may or may not have additional degrees of freedom. The resulting methods are extremely complex and need to be tailored to individual problems of crack growth.

A different approach is to retain the conventional FEM approach but assume that the interface between any two elements represents a region of discontinuity and this is modeled by a "gap" or a cohesive element [7, 37, 38]. When the gap becomes sufficiently large, the cohesive element separates. This has the advantage of a reasonably simple approach that can be relatively simply implemented. On the other hand, care must be taken to prevent gaps from opening up between the elements even before fracture. Furthermore, the cracks can only grow along the element interfaces and thus the paths are limited. One other shortcoming of this method is that the crack path should be known in advance to enrich the elements located on the crack path with cohesive zones. One solution to overcome this issue is to enrich all elements with cohesive zones, however, according to Needleman [38] this solution might result in convergence issues with an increase in mesh refinement. Cohesive zone models are suitable for use in finite element modeling of fracture studies in which one can specify the surfaces where cracking takes place a priori.

2.1.1.2 Bond–breakage models

In contrast to the methods mentioned in the previous section, bond–breakage methods rely on discretization of a continuum into a truss network. Lattice models (see e.g [39–43]) simply replace the original body with a discrete lattice, resulting in a simple truss–like model. Fracture is simply modeled by the failure of the individual links of the truss. More recently, an approach referred to as peridynamics [13, 44–46], which entirely upends the foundations of local response of continua, has found favor to a great extent to deal with fracture (see e.g. [47–50]). Here, there are no partial differential equations, but only "bond forces" which are forces between a given particle and other particles in its "horizon". Fracture is then simulated by assuming special forms for the bond forces as a function of bond distance (e.g. they drop to zero and the bond is broken when the bond forces exceed a critical value). Bond–breakage methods are simple and easier to implement, but are not fully physically realistic, because for solids composed of a local lattice network of two–force members the Poisson's ratio is limited to 0.25 [14].

2.1.2 Present Study

The major question in this study is the following: Is it possible to retain the simplicity and physical realism of a conventional FEM, but allow for a treatment of fracture that is as simple as that for lattice models or peridynamics, hence allowing us to simulate complex fracture problems in a simple discrete format (i.e., can we eat our cake and have it too)? The surprising answer to this is yes, if we are able to reformulate classical FEM to be more like a truss model without any simplification.

Recently, Reddy and Srinivasa [16] presented an idea to reformulate conventional finite element method (FEM) such that it becomes more suitable for the study of damage. In their study [16], it is shown that for a hyperelastic material the forces of a discretized system can be written in terms of the strains along the edges of the elements[2]. It is also shown that the forces are directed along the edges of the element. Proof is provided for any choice of element (although in this study we will

[2] An edge is any line between two individual nodes of an element.

focus only on constant strain triangular (CST) elements as a proof of concept). Although Reddy and Srinivasa [16] proved that this could be done, this is the first study to develop a numerical scheme based on this idea.

The central idea of this study is to reformulate conventional FEM which its focus is on the elements, to a modified version in which the focus is on nodes and edges (or links). This modified version is named as graph–based finite element framework, or GraFEA in short. The difference between this idea and a conventional truss system is that the force along each edge depends on the properties of the whole element and not only displacements along a specific edge. GraFEA allows us to approach fracture in a discrete way (rather than the existing continuum methods) which is more conforming to the nature of fracture. The damage criterion used in this study is based on the nonlocal damage criterion initially proposed by Ritchie, Knott, and Rice [20] which was successful in predicting cleavage cracking in mild steel at low temperatures. It was stated in their study [20] that crack in brittle materials does not proceed when the stress at the crack tip exceeds a critical value, but when local stress at a microstructurally significant length (known as the *characteristic distance*) exceeds the critical fracture stress. Later, Lin, Evans, and Ritchie [21] added the idea of the weakest link statistics, saying that if a characteristic zone large enough is considered ahead of the crack tip to guarantee the existence of a flaw, the crack propagates when the local stress in the zone exceeds the critical stress.

In summary, the novel elements of this work are

1. Development of a nonlocal network based on numerical formulation for the discretization of a continuum.
2. Introduction of a purely discrete edge–based damage variable, ϕ_i, which describes the state of damage of any link in the network. This is quite different from the damage variable used in damage mechanics which is based on location alone and not on connectivity.
3. Development of a nonlocal criterion for the failure of a link based on the weakest link statistics idea introduced by Lin, Evans, and Ritchie [21].
4. Showing that such an approach is capable of studying fracture propagation in brittle materi-

als.

The structure of this study is as follows: In section 2.2 the formulation provided by Reddy and Srinivasa [16] for a right triangular element is generalized to an arbitrary triangular element using strain transformation. It is shown that for the arbitrary triangular element the forces act along the edges of the element. The stiffness matrix is derived to show that it matches that of the conventional FEM. In section 2.3 an edge–based damage criterion for brittle failure is introduced into the graph–based model derived in section 2.2 using the ideas proposed by Ritchie, Knott, and Rice [20], and Lin, Evans, and Ritchie [21]. It is also shown how this failure criterion influences the forces along the edges, and the stiffness matrix. The formulation is such that it simplifies to conventional FEM when no damage is considered. In section 2.4 the methodology of integrating GraFEA with conventional FEM is delivered, and two numerical examples are studied. Finally concluding remarks and future directions are brought in section 2.5.

2.2 Theoretical Formulation

2.2.1 Strain Transformation

Suppose a triangular element of arbitrary edge lengths of the form shown in figure 2.1. In this study, the element is chosen to be a linear triangular element with constant strains. One can determine the normal strain in a direction making an angle φ with the positive x direction simply by using a transformation equation and the constant elasticity strains $\varepsilon_{xx},\ \varepsilon_{yy},\ \gamma_{xy}$:

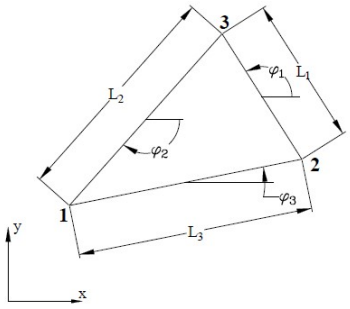

Figure 2.1: Arbitrary linear triangular element.

$$\varepsilon = \varepsilon_{xx}\cos^2\varphi + \varepsilon_{yy}\sin^2\varphi + \gamma_{xy}\sin\varphi\cos\varphi \tag{2.1}$$

Therefore, a relation can be written between the sets of strains $(\varepsilon_{xx},\, \varepsilon_{yy},\, \gamma_{xy})$, and $(\varepsilon_1,\, \varepsilon_2,\, \varepsilon_3)$, where ε_i, $i = 1, 2, 3$ is the normal strain along the edge formed by nodes j and k ($j, k \neq i$, and assuming positive permutation between i, j, and k). The strain is taken positive if elongation occurs along the edge, and vice versa. The relation between the two sets of strains is:

$$\begin{Bmatrix} \varepsilon_1 \\ \varepsilon_2 \\ \varepsilon_3 \end{Bmatrix} = \begin{bmatrix} \cos\varphi_1^2 & \sin\varphi_1^2 & \cos\varphi_1\sin\varphi_1 \\ \cos\varphi_2^2 & \sin\varphi_2^2 & \cos\varphi_2\sin\varphi_2 \\ \cos\varphi_3^2 & \sin\varphi_3^2 & \cos\varphi_3\sin\varphi_3 \end{bmatrix} \begin{Bmatrix} \varepsilon_{xx} \\ \varepsilon_{yy} \\ \gamma_{xy} \end{Bmatrix} = \mathbf{T} \begin{Bmatrix} \varepsilon_{xx} \\ \varepsilon_{yy} \\ \gamma_{xy} \end{Bmatrix} \tag{2.2}$$

where $\cos\varphi_i = \frac{x_k - x_j}{L_i}$ and $\sin\varphi_i = \frac{y_k - y_j}{L_i}$ (i, j, and k permute in a natural order). $\mathbf{T}$ is the transformation matrix between the set of elasticity strains $(\varepsilon_{xx},\, \varepsilon_{yy},\, \gamma_{xy})$ and the set of normal strains along the edges $(\varepsilon_1,\, \varepsilon_2,\, \varepsilon_3)$. Equation (2.2) can be rewritten using the interpolation functions for a linear triangular element in conventional FEM [51]:

$$\psi_i^e = \frac{1}{2A_e}\left(\alpha_i^e + \beta_i^e x + \gamma_i^e y\right), \qquad i = 1, 2, 3 \tag{2.3}$$

where

$$\begin{aligned} &\alpha_i^e = x_j y_k - x_k y_j, \qquad \beta_i^e = y_j - y_k, \qquad \gamma_i^e = -\left(x_j - x_k\right) \\ &\sum_{i=1}^{3} \alpha_i^e = 2A^e = x_2 y_3 - x_3 y_2 + x_3 y_1 - x_1 y_3 + x_1 y_2 - x_2 y_1 \end{aligned} \tag{2.4}$$

Using the definitions of β_i and γ_i in Eq. (2.4), the transformation matrix of Eq. (2.2) is rewritten as

$$\mathbf{T} = \begin{bmatrix} \frac{1}{L_1^2} & 0 & 0 \\ 0 & \frac{1}{L_2^2} & 0 \\ 0 & 0 & \frac{1}{L_3^2} \end{bmatrix} \begin{bmatrix} \gamma_1^2 & \beta_1^2 & -\gamma_1\beta_1 \\ \gamma_2^2 & \beta_2^2 & -\gamma_2\beta_2 \\ \gamma_3^2 & \beta_3^2 & -\gamma_3\beta_3 \end{bmatrix} \tag{2.5}$$

The inverse of matrix $\mathbf{T}$ is the matrix which relates the strains $(\varepsilon_1,\, \varepsilon_2,\, \varepsilon_3)$ to the strains $(\varepsilon_{xx},\, \varepsilon_{yy},\, \gamma_{xy})$. Performing some calculations and using the definition of A^e from Eq. (2.4), the

inverse of the transformation matrix is derived to be:

$$\mathbf{T}^{-1} = -\frac{1}{4A^2}\begin{bmatrix} \beta_2\beta_3 & \beta_1\beta_3 & \beta_1\beta_2 \\ \gamma_2\gamma_3 & \gamma_1\gamma_3 & \gamma_1\gamma_2 \\ \beta_2\gamma_3+\beta_3\gamma_2 & \beta_1\gamma_3+\beta_3\gamma_1 & \beta_1\gamma_2+\beta_2\gamma_1 \end{bmatrix}\begin{bmatrix} L_1^2 & 0 & 0 \\ 0 & L_2^2 & 0 \\ 0 & 0 & L_3^2 \end{bmatrix}$$
$$\begin{Bmatrix} \varepsilon_{xx} \\ \varepsilon_{yy} \\ \gamma_{xy} \end{Bmatrix} = \mathbf{T}^{-1}\begin{Bmatrix} \varepsilon_1 \\ \varepsilon_2 \\ \varepsilon_3 \end{Bmatrix} \tag{2.6}$$

ε_1, ε_2, and ε_3 can also be written in terms of the axial displacements mirrored along the edges of the triangular element (figure 2.2), where d_i corresponds to the increase in length of the edge located in front of node i.

$$d_i = (\mathbf{u}_k - \mathbf{u}_j)\,.\mathbf{e}_i, \qquad \varepsilon_i = \frac{d_i}{L_i} \tag{2.7}$$

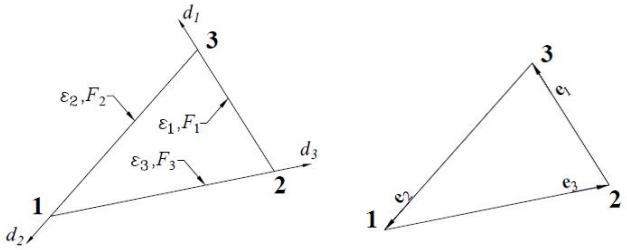

(a) (b)

Figure 2.2: (a) Nodal Displacements mirrored along the edges (b) Unit vectors along the edges of the triangular element. The edge in front of node i is locally named as edge i, and its unit vector is determined heading from node j to node k (with i, j, and k in a natural order).

Unit vectors $\mathbf{e}_i$ are shown in figure 2.2b. The unit vectors along d_1, d_2, and d_3 are named $\mathbf{e}_1$, $\mathbf{e}_2$, and $\mathbf{e}_3$, respectively which are defined in the following equation (Figure 2.2b):

$$\mathbf{e}_i = \left\langle \cos\varphi_i \quad \sin\varphi_i \right\rangle^T \tag{2.8}$$

2.2.2 Strain Energy Function

For linear elasticity problems, the strain energy density for a continuum is written as:

$$U_0^e = \frac{1}{2}\sigma_{ij}\varepsilon_{ij} \tag{2.9}$$

For a two–dimensional isotropic plane elasticity problem, the stress–strain relationship is

$$\begin{Bmatrix} \sigma_{xx} \\ \sigma_{yy} \\ \sigma_{xy} \end{Bmatrix} = \begin{bmatrix} c_{11} & c_{12} & 0 \\ c_{12} & c_{22} & 0 \\ 0 & 0 & c_{66} \end{bmatrix} \begin{Bmatrix} \varepsilon_{xx} \\ \varepsilon_{yy} \\ \gamma_{xy} \end{Bmatrix} \rightarrow \boldsymbol{\sigma} = \mathbf{C}\boldsymbol{\varepsilon} \tag{2.10}$$

where coefficients c_{ij} differ for plane strain and plane stress problems (Table 2.1). For isotropic materials, $E_1 = E_2 = E$, $G_{12} = G = \frac{E}{2(1+\nu)}$, $\nu_{12} = \nu_{21} = \nu$.

Table 2.1: Coefficients for plane elasticity problems.

	c_{11}	c_{22}	c_{12}	c_{66}
Plane Strain	$\frac{E_1(1-\nu_{12}\nu_{21})}{(1+\nu_{12})(1-\nu_{12}-2\nu_{12}\nu_{21})}$	$\frac{E_2(1-\nu_{12}\nu_{21})}{(1+\nu_{12})(1-\nu_{12}-2\nu_{12}\nu_{21})}$	$\frac{\nu_{12}E_2}{1-\nu_{12}-2\nu_{12}\nu_{21}}$	G_{12}
Plane Stress	$\frac{E_1}{1-\nu_{12}\nu_{21}}$	$\frac{E_2}{1-\nu_{12}\nu_{21}}$	$\frac{\nu_{12}E_2}{1-\nu_{12}\nu_{21}}$	G_{12}

The strain energy density function for a plane elasticity problem is obtained by substituting from the constitutive equation (Eq. (2.10)):

$$2U_0^e = \sigma_{xx}\varepsilon_{xx} + \sigma_{yy}\varepsilon_{yy} + \sigma_{xy}\gamma_{xy} = c_{11}\varepsilon_{xx}^2 + c_{22}\varepsilon_{yy}^2 + 2c_{12}\varepsilon_{xx}\varepsilon_{yy} + c_{66}\gamma_{xy}^2 \tag{2.11}$$

Using Eq. (2.6) one can rewrite Eq. (2.11) in terms of strains $(\varepsilon_1,\ \varepsilon_2,\ \varepsilon_3)$:

$$2U_0^e = \frac{1}{16A^4}\Bigg\{ c_{11}\left(-\beta_2\beta_3 L_1^2\varepsilon_1 - \beta_1\beta_3 L_2^2\varepsilon_2 - \beta_1\beta_2 L_3^2\varepsilon_3\right)^2$$

$$
\begin{aligned}
&+ c_{22}\left(-\gamma_2\gamma_3 L_1^2\varepsilon_1 - \gamma_1\gamma_3 L_2^2\varepsilon_2 - \gamma_1\gamma_2 L_3^2\varepsilon_3\right)^2 \\
&+ 2c_{12}\left(-\beta_2\beta_3 L_1^2\varepsilon_1 - \beta_1\beta_3 L_2^2\varepsilon_2 - \beta_1\beta_2 L_3^2\varepsilon_3\right) \\
&\times \left(-\gamma_2\gamma_3 L_1^2\varepsilon_1 - \gamma_1\gamma_3 L_2^2\varepsilon_2 - \gamma_1\gamma_2 L_3^2\varepsilon_3\right) \\
&+ c_{66}\Big[-\left(\beta_2\gamma_3 + \beta_3\gamma_2\right) L_1^2\varepsilon_1 - \left(\beta_1\gamma_3 + \beta_3\gamma_1\right) L_2^2\varepsilon_2 - \left(\beta_1\gamma_2 + \beta_2\gamma_1\right) L_3^2\varepsilon_3\Big]^2\Bigg\}
\end{aligned} \tag{2.12}
$$

Equation (2.12) is summarized to the following form with coefficients A_{ij} defined in Eq. (2.14). One should note that coefficients A_{ij} depend not only on elasticity constants c_{ij}, but also on geometric properties of the constant strain triangular element.

$$
U_0^e = A_{11}\varepsilon_1^2 + A_{22}\varepsilon_2^2 + A_{33}\varepsilon_3^2 + A_{12}\varepsilon_1\varepsilon_2 + A_{23}\varepsilon_2\varepsilon_3 + A_{31}\varepsilon_3\varepsilon_1 \tag{2.13}
$$

$$
\begin{aligned}
A_{11} =& \frac{L_1^4}{32A^4}\Big\{\beta_2^2\beta_3^2 c_{11} + \gamma_2^2\gamma_3^2 c_{22} + 2\beta_2\beta_3\gamma_2\gamma_3 c_{12} + \left(\beta_2\gamma_3 + \beta_3\gamma_2\right)^2 c_{66}\Big\} \\
A_{22} =& \frac{L_2^4}{32A^4}\Big\{\beta_1^2\beta_3^2 c_{11} + \gamma_1^2\gamma_3^2 c_{22} + 2\beta_1\beta_3\gamma_1\gamma_3 c_{12} + \left(\beta_1\gamma_3 + \beta_3\gamma_1\right)^2 c_{66}\Big\} \\
A_{33} =& \frac{L_3^4}{32A^4}\Big\{\beta_1^2\beta_2^2 c_{11} + \gamma_1^2\gamma_2^2 c_{22} + 2\beta_1\beta_2\gamma_1\gamma_2 c_{12} + \left(\beta_1\gamma_2 + \beta_2\gamma_1\right)^2 c_{66}\Big\} \\
A_{12} =& \frac{L_1^2 L_2^2}{16A^4}\Big\{\beta_1\beta_2\beta_3^2 c_{11} + \gamma_1\gamma_2\gamma_3^2 c_{22} + \beta_3\gamma_3\left(\beta_1\gamma_2 + \beta_2\gamma_1\right) c_{12} \\
&\qquad + \left(\beta_2\gamma_3 + \beta_3\gamma_2\right)\left(\beta_1\gamma_3 + \beta_3\gamma_1\right) c_{66}\Big\} \\
A_{23} =& \frac{L_2^2 L_3^2}{16A^4}\Big\{\beta_1^2\beta_2\beta_3 c_{11} + \gamma_1^2\gamma_2\gamma_3 c_{22} + \beta_1\gamma_1\left(\beta_2\gamma_3 + \beta_3\gamma_2\right) c_{12} \\
&\qquad + \left(\beta_1\gamma_3 + \beta_3\gamma_1\right)\left(\beta_1\gamma_2 + \beta_2\gamma_1\right) c_{66}\Big\} \\
A_{31} =& \frac{L_1^2 L_3^2}{16A^4}\Big\{\beta_1\beta_2^2\beta_3 c_{11} + \gamma_1\gamma_2^2\gamma_3 c_{22} + \beta_2\gamma_2\left(\beta_1\gamma_3 + \beta_3\gamma_1\right) c_{12} \\
&\qquad + \left(\beta_1\gamma_2 + \beta_2\gamma_1\right)\left(\beta_2\gamma_3 + \beta_3\gamma_2\right) c_{66}\Big\}
\end{aligned} \tag{2.14}
$$

The total strain energy of an element is obtained by integrating the strain energy density over the volume of the element. Since in this study we are only concerned with constant strain triangular elements, normal strains ε_i will be constant and the integration over the element becomes very

simple:

$$U^e = \int_\Omega U_0^e dV = A^e h^e U_0^e$$
$$= A^e h^e \left(A_{11}\varepsilon_1^2 + A_{22}\varepsilon_2^2 + A_{33}\varepsilon_3^2 + A_{12}\varepsilon_1\varepsilon_2 + A_{23}\varepsilon_2\varepsilon_3 + A_{31}\varepsilon_3\varepsilon_1 \right) \tag{2.15}$$

2.2.3 Nodal Forces

In this section proof is brought to show that for a discretized plane elasticity problem the forces will be directed along the edges of the arbitrary triangular element. Using Castigliano's theorem I, the forces at each node of the triangular element (contributions from one particular element) is derived from the strain energy of that element:

$$F_i = \frac{\partial U^e}{\partial u_i} = h^e A^e \frac{\partial U^e}{\partial \boldsymbol{\varepsilon}} . \frac{\partial \boldsymbol{\varepsilon}}{\partial u_i} = h^e A^e \left(\frac{\partial U^e}{\partial \varepsilon_{xx}} \frac{\partial \varepsilon_{xx}}{\partial u_i} + \frac{\partial U^e}{\partial \varepsilon_{yy}} \frac{\partial \varepsilon_{yy}}{\partial u_i} + \frac{\partial U^e}{\partial \gamma_{xy}} \frac{\partial \gamma_{xy}}{\partial u_i} \right) \tag{2.16}$$

where F_i and u_i are nodal forces and nodal displacements, respectively. Since there are two sets of strains in this study ($\varepsilon_{xx}, \varepsilon_{yy}, \gamma_{xy}$ and $\varepsilon_1, \varepsilon_2, \varepsilon_3$), contracted notation cannot be used in Eq. (2.16). $\varepsilon_i,\ i = 1, 2, 3$ corresponds to the strains along the edges of the triangular element. To be able to use contracted notation and distinguish the two sets of strains, the notation of $\varepsilon_i^*(\sigma_i^*)$ is used to refer to $(\varepsilon_{xx}, \varepsilon_{yy}, \gamma_{xy})$ and the corresponding stresses. Therefore, Eq. (2.16) can be restated as follows:

$$F_i = hA \frac{\partial U_0}{\partial \varepsilon_j^*} \frac{\partial \varepsilon_j^*}{\partial u_i} \tag{2.17}$$

where for the sake of brevity the superscript e is omitted from h and A. Note that one can further simplify Eq. (2.17) by noting that $\frac{\partial U_0}{\partial \varepsilon_j^*} = \sigma_j^*$. For a linear triangular element 6 components of forces and displacements exist:

$$\mathbf{F} = \left\langle F_x^1 \quad F_y^1 \quad F_x^2 \quad F_y^2 \quad F_x^3 \quad F_y^3 \right\rangle^T, \quad \mathbf{u} = \left\langle u_x^1 \quad u_y^1 \quad u_x^2 \quad u_y^2 \quad u_x^3 \quad u_y^3 \right\rangle^T \tag{2.18}$$

Using the chain rule, one can express $\frac{\partial \varepsilon_j^*}{\partial u_i}$ in terms of d_i (displacements along the edges of the triangular element as shown in figure 2.2).

$$F_i = hA\sigma_j^* \frac{\partial \varepsilon_j^*}{\partial d_k} \frac{\partial d_k}{\partial u_i} \tag{2.19}$$

Using d_i from Eq. (2.7), Eq. (2.13) can also be written in terms of deformation along the edges of the elements, where $d_i = \varepsilon_i L_i$. Using Eqs. (2.6), and (2.7), one gets:

$$\begin{aligned}
\begin{Bmatrix} \varepsilon_{xx} \\ \varepsilon_{yy} \\ \gamma_{xy} \end{Bmatrix} &= \mathbf{T}^{-1} \begin{Bmatrix} \varepsilon_1 = \frac{d_1}{L_1} \\ \varepsilon_2 = \frac{d_2}{L_2} \\ \varepsilon_3 = \frac{d_3}{L_3} \end{Bmatrix} \\
&= -\frac{1}{4A^2} \begin{bmatrix} \beta_2\beta_3 & \beta_1\beta_3 & \beta_1\beta_2 \\ \gamma_2\gamma_3 & \gamma_1\gamma_3 & \gamma_1\gamma_2 \\ \beta_2\gamma_3 + \beta_3\gamma_2 & \beta_1\gamma_3 + \beta_3\gamma_1 & \beta_1\gamma_2 + \beta_2\gamma_1 \end{bmatrix} \begin{bmatrix} L_1 & 0 & 0 \\ 0 & L_2 & 0 \\ 0 & 0 & L_3 \end{bmatrix} \begin{Bmatrix} d_1 \\ d_2 \\ d_3 \end{Bmatrix}
\end{aligned} \tag{2.20}$$

Finally, Eq. (2.19) is written in matrix form as

$$\mathbf{F} = hA\mathbf{A}_1\mathbf{A}_2\boldsymbol{\sigma}^* \tag{2.21}$$

where $\mathbf{F}$ is defined in Eq. (2.18), $\boldsymbol{\sigma}^*$, $\mathbf{A}_1$, and $\mathbf{A}_2$ are defined in the following:

$$\boldsymbol{\sigma}^* = \begin{Bmatrix} \sigma_1^* & \sigma_2^* & \sigma_3^* \end{Bmatrix}^T = \begin{Bmatrix} \sigma_{xx} & \sigma_{yy} & \sigma_{xy} \end{Bmatrix}^T \tag{2.22}$$

$$\mathbf{A}_1 = \begin{bmatrix} \frac{\partial d_1}{\partial u_x^1} & \frac{\partial d_2}{\partial u_x^1} & \frac{\partial d_3}{\partial u_x^1} \\ \frac{\partial d_1}{\partial u_y^1} & \frac{\partial d_2}{\partial u_y^1} & \frac{\partial d_3}{\partial u_y^1} \\ \frac{\partial d_1}{\partial u_x^2} & \frac{\partial d_2}{\partial u_x^2} & \frac{\partial d_3}{\partial u_x^2} \\ \frac{\partial d_1}{\partial u_y^2} & \frac{\partial d_2}{\partial u_y^2} & \frac{\partial d_3}{\partial u_y^2} \\ \frac{\partial d_1}{\partial u_x^3} & \frac{\partial d_2}{\partial u_x^3} & \frac{\partial d_3}{\partial u_x^3} \\ \frac{\partial d_1}{\partial u_y^3} & \frac{\partial d_2}{\partial u_y^3} & \frac{\partial d_3}{\partial u_y^3} \end{bmatrix} = \begin{bmatrix} 0 & \cos\varphi_2 & -\cos\varphi_3 \\ 0 & \sin\varphi_2 & -\sin\varphi_3 \\ -\cos\varphi_1 & 0 & \cos\varphi_3 \\ -\sin\varphi_1 & 0 & \sin\varphi_3 \\ \cos\varphi_1 & -\cos\varphi_2 & 0 \\ \sin\varphi_1 & -\sin\varphi_2 & 0 \end{bmatrix}$$

$$= \begin{bmatrix} 0 & \gamma_2 & -\gamma_3 \\ 0 & -\beta_2 & \beta_3 \\ -\gamma_1 & 0 & \gamma_3 \\ \beta_1 & 0 & -\beta_3 \\ \gamma_1 & -\gamma_2 & 0 \\ -\beta_1 & \beta_2 & 0 \end{bmatrix} \begin{bmatrix} \frac{1}{L_1} & 0 & 0 \\ 0 & \frac{1}{L_2} & 0 \\ 0 & 0 & \frac{1}{L_3} \end{bmatrix} \tag{2.23}$$

$$\mathbf{A}_2 = \begin{bmatrix} \frac{\partial \varepsilon_1^*}{\partial d_1} & \frac{\partial \varepsilon_2^*}{\partial d_1} & \frac{\partial \varepsilon_3^*}{\partial d_1} \\ \frac{\partial \varepsilon_1^*}{\partial d_2} & \frac{\partial \varepsilon_2^*}{\partial d_2} & \frac{\partial \varepsilon_3^*}{\partial d_2} \\ \frac{\partial \varepsilon_1^*}{\partial d_3} & \frac{\partial \varepsilon_2^*}{\partial d_3} & \frac{\partial \varepsilon_3^*}{\partial d_3} \end{bmatrix} = \begin{bmatrix} \frac{\partial \varepsilon_{xx}}{\partial d_1} & \frac{\partial \varepsilon_{yy}}{\partial d_1} & \frac{\partial \gamma_{xy}}{\partial d_1} \\ \frac{\partial \varepsilon_{xx}}{\partial d_2} & \frac{\partial \varepsilon_{yy}}{\partial d_2} & \frac{\partial \gamma_{xy}}{\partial d_2} \\ \frac{\partial \varepsilon_{xx}}{\partial d_3} & \frac{\partial \varepsilon_{yy}}{\partial d_3} & \frac{\partial \gamma_{xy}}{\partial d_3} \end{bmatrix}$$

$$= -\frac{1}{4A^2} \begin{bmatrix} L_1 & 0 & 0 \\ 0 & L_2 & 0 \\ 0 & 0 & L_3 \end{bmatrix} \begin{bmatrix} \beta_2\beta_3 & \gamma_2\gamma_3 & \beta_2\gamma_3 + \beta_3\gamma_2 \\ \beta_1\beta_3 & \gamma_1\gamma_3 & \beta_1\gamma_3 + \beta_3\gamma_1 \\ \beta_1\beta_2 & \gamma_1\gamma_2 & \beta_1\gamma_2 + \beta_2\gamma_1 \end{bmatrix} \tag{2.24}$$

Note that $\mathbf{A}_1\mathbf{A}_2 = \mathbf{B}^T$, where $\mathbf{B}$ is the matrix relating the strains to the displacements for constant strain triangular element in plane elasticity problems (refer to Reddy [51]):

$$\mathbf{B} = \frac{1}{2A} \begin{bmatrix} \beta_1 & 0 & \beta_2 & 0 & \beta_3 & 0 \\ 0 & \gamma_1 & 0 & \gamma_2 & 0 & \gamma_3 \\ \gamma_1 & \beta_1 & \gamma_2 & \beta_2 & \gamma_3 & \beta_3 \end{bmatrix} \tag{2.25}$$

Finally, F_i can be written as follows:

$$\mathbf{F} = hA \begin{Bmatrix} (a_{21}\sigma_{xx} + a_{22}\sigma_{yy} + a_{23}\sigma_{xy})\cos\varphi_2 - (a_{31}\sigma_{xx} + a_{32}\sigma_{yy} + a_{33}\sigma_{xy})\cos\varphi_3 \\ (a_{21}\sigma_{xx} + a_{22}\sigma_{yy} + a_{23}\sigma_{xy})\sin\varphi_2 - (a_{31}\sigma_{xx} + a_{32}\sigma_{yy} + a_{33}\sigma_{xy})\sin\varphi_3 \\ (a_{31}\sigma_{xx} + a_{32}\sigma_{yy} + a_{33}\sigma_{xy})\cos\varphi_3 - (a_{11}\sigma_{xx} + a_{12}\sigma_{yy} + a_{13}\sigma_{xy})\cos\varphi_1 \\ (a_{31}\sigma_{xx} + a_{32}\sigma_{yy} + a_{33}\sigma_{xy})\sin\varphi_3 - (a_{11}\sigma_{xx} + a_{12}\sigma_{yy} + a_{13}\sigma_{xy})\sin\varphi_1 \\ (a_{11}\sigma_{xx} + a_{12}\sigma_{yy} + a_{13}\sigma_{xy})\cos\varphi_1 - (a_{21}\sigma_{xx} + a_{22}\sigma_{yy} + a_{23}\sigma_{xy})\cos\varphi_2 \\ (a_{11}\sigma_{xx} + a_{12}\sigma_{yy} + a_{13}\sigma_{xy})\sin\varphi_1 - (a_{21}\sigma_{xx} + a_{22}\sigma_{yy} + a_{23}\sigma_{xy})\sin\varphi_2 \end{Bmatrix} \tag{2.26}$$

where, a_{ij} are the components of the matrix $\mathbf{A}_2$. Note that the sum of the forces of the three nodes is equal to zero. The unit vectors are chosen such that they give a CCW rotation (using the right hand rule) from the node of interest. For instance, unit vector $\mathbf{e}_1$ will be from node 2 to node 3 (Figure 2.2b). From observation of Eq. (2.26), one can notice that the force vector can be summarized as:

$$\mathbf{F} = \begin{Bmatrix} \mathbf{F}_1 \\ \mathbf{F}_2 \\ \mathbf{F}_3 \end{Bmatrix} = hA \begin{Bmatrix} (a_{21}\sigma_{xx} + a_{22}\sigma_{yy} + a_{23}\sigma_{xy})\,\mathbf{e}_2 - (a_{31}\sigma_{xx} + a_{32}\sigma_{yy} + a_{33}\sigma_{xy})\,\mathbf{e}_3 \\ (a_{31}\sigma_{xx} + a_{32}\sigma_{yy} + a_{33}\sigma_{xy})\,\mathbf{e}_3 - (a_{11}\sigma_{xx} + a_{12}\sigma_{yy} + a_{13}\sigma_{xy})\,\mathbf{e}_1 \\ (a_{11}\sigma_{xx} + a_{12}\sigma_{yy} + a_{13}\sigma_{xy})\,\mathbf{e}_1 - (a_{21}\sigma_{xx} + a_{22}\sigma_{yy} + a_{23}\sigma_{xy})\,\mathbf{e}_2 \end{Bmatrix} \tag{2.27}$$

This shows that the forces are directed along the edges of the triangular element, and it also gives an explicit expression of how they relate to the stresses. One could use the constitutive equation for plane elasticity problems (Eq. (2.10)) and the transformation equation (Eq. (2.6)) to substitute for the stresses in Eq. (2.27) and rewrite the forces in terms of the strains along the edges:

$$\boldsymbol{\sigma}^* = \mathbf{C}\boldsymbol{\varepsilon}^* = \mathbf{C}\mathbf{T}^{-1}\boldsymbol{\varepsilon} \tag{2.28}$$

The idea behind GraFEA is to transform the continuum to a network of links, where the edges of the elements of the discretized continuum serve as the links. However, it should be noted that although the nodal forces can be written in terms of the strains along the edges of the element, this dependence is not local as in the case of a conventional truss network. The force along edge i does not only depend on the strain along edge i, but on the strains along the edges of all elements sharing edge i (as well as material and geometric properties of the element). Consequently, the resulting network is nonlocal and the force along each edge depends on a collective behavior of that specific edge and all the neighboring edges. Figure 2.3a shows nonlocality of the forces within one element. For edges shared between more than one element (Figure 2.3b) the force along the edge common between two elements depends on the strains of all edges of the two elements. In figure 2.3b global node numbering and edge numbering is shown for the assembly of two elements.

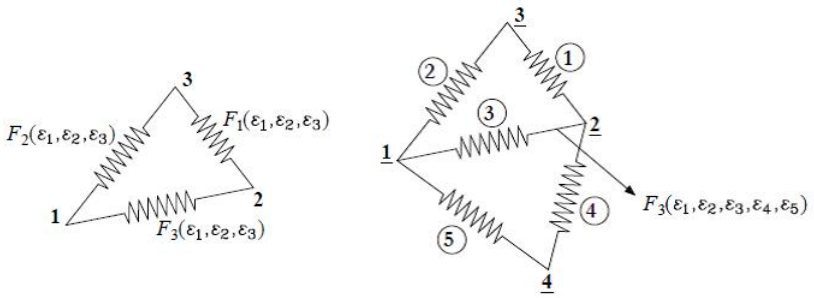

(a) (b)

Figure 2.3: Nonlocal forces comprising to a nonlocal network (a) One constant strain triangular element (b) An edge shared between two elements.

Note that although the present formulation is provided for the case of a constant–strain linear triangular element, Reddy and Srinivasa [16] proved that for any hyperelastic material in the discretized form the magnitude of the nodal forces can be written in terms of the strains along the edges of the element.

2.2.4 Stiffness Matrix

The stiffness matrix is derived to compare the results with that of conventional FEM for further verification. Previously, nodal forces were derived in Eq. (2.19) using Castigliano's theorem I. Stiffness matrix is determined next:

$$F_i = \frac{\partial U}{\partial u_i} = hA\sigma_n^* \frac{\partial \varepsilon_n^*}{\partial d_m}\frac{\partial d_m}{\partial u_i}, \quad K_{ij} = \frac{\partial F_i}{\partial u_j} = hA\frac{\partial d_m}{\partial u_i}\frac{\partial \varepsilon_n^*}{\partial d_m}.\frac{\partial \sigma_n^*}{\partial u_j} \tag{2.29}$$

The last term in K_{ij} can be further simplified using the elasticity matrix in Eq. (2.10).

$$\frac{\partial \sigma_n^*}{\partial u_j} = C_{np}\frac{\partial \varepsilon_p^*}{\partial u_j} = C_{np}\frac{\partial \varepsilon_p^*}{\partial d_q}\frac{\partial d_q}{\partial u_j} \tag{2.30}$$

Finally, the equation for K_{ij} can be written as:

$$K_{ij} = hA\frac{\partial F_i}{\partial u_j} = hA\frac{\partial d_m}{\partial u_i}\frac{\partial \varepsilon_n^*}{\partial d_m}C_{np}\frac{\partial \varepsilon_p^*}{\partial d_q}\frac{\partial d_q}{\partial u_j} \tag{2.31}$$

The above equation can also be expressed in matrix form. Note that the stiffness matrix is symmetric ($\mathbf{K} = \mathbf{K}^T$).

$$\mathbf{K} = hA\mathbf{A}_1\mathbf{A}_2\mathbf{C}\mathbf{A}_2^T\mathbf{A}_1^T = hA\mathbf{B}^T C\mathbf{B} \tag{2.32}$$

It is apparent that the stiffness matrix is the same as that of the conventional FEM.

2.3 Introduction of Damage

2.3.1 Nonlocal Damage Criterion

Ritchie, Knott, and Rice [20] stated that cleavage fracture in mild steel at very low temperatures (brittle type of fracture) does not only depend on the stress at the tip of the crack. According to Ritchie, Knott, and Rice [20]:

> "If the fracture criterion in a sharp–cracked specimen were simply that σ_{yy} should be sufficiently large to exceed a critical value σ_f, it is apparent that fracture could be produced, very close to the crack tip, by vanishingly small applied loads. Hence, it seems necessary to supplement such a criterion by the additional requirement that the critical stress be achieved over some microstructurally significant distance (the *characteristic distance*) ahead of the tip."

Consequently, it is necessary to impose a nonlocal damage criterion (named as RKR criterion) over the characteristic distance ahead of the tip. They have shown that this fracture criterion can be analytically related to the fracture toughness of the material, K_{Ic}. Ritchie, Knott, and Rice [20] showed that the agreement between the analytically derived values for K and those from experiments at very low temperatures is good for a characteristic distance of two grain diameters.

Later, Lin, Evans, and Ritchie [21] studied brittle fracture of steel at low temperatures by augmenting the RKR nonlocal damage criterion with the weakest link statistics (a probabilistic

approach). In summary, the idea was that if the characteristic zone is chosen large enough to guarantee the existence of flaws, fracture propagates when the local stress in the region exceeds the critical value σ_f. By assuming a region ahead of the crack tip, the competition between the far–field behavior (where more cracked particles are available but the stress values are lower) with that of the near–tip behavior (where the number of eligible particles is less, but stresses are higher) can be accounted for. Using the idea of weakest link statistics, Lin, Evans, and Ritchie [21] proposed a relation for the characteristic distance which is statistically equivalent to the location ahead of the tip where the cracking is most probable.

The idea of weakest link statistics is implemented in this study to introduce damage criterion into GraFEA. The graph–based representation of the continuum allows for the introduction of damage similar to what is done for conventional truss networks. The core idea is that the weighted averaged strain in any given direction over the characteristic distance (related to the fracture toughness of the material) has to exceed a critical value, $\varepsilon_{\text{critical}}$. In other words, a link in the network will fail if:

$$\bar{\varepsilon}_i = \mathbf{e}_i \cdot \left[\int_{\Omega_{\|\mathbf{r}\| \leq d}} \phi\left(\mathbf{x} - \mathbf{x}_0\right) \boldsymbol{\varepsilon}\left(\mathbf{x}_0\right) d\Omega \right] \mathbf{e}_i \geq \varepsilon_{\text{critical}} \tag{2.33}$$

where $\mathbf{e}_i$ is the unit vector along the edge of interest, and the weighting function $\phi\left(\mathbf{x} - \mathbf{x}_0\right)$ is such that:

$$\int_{\Omega_{\|\mathbf{r}\| \leq d}} \phi\left(\mathbf{x} - \mathbf{x}_0\right) d\Omega = 1 \tag{2.34}$$

Damage variable, ϕ_i, is imposed to the weighted averaged normal strain, $\bar{\varepsilon}_i$, along edge i if the averaged strain for edge i exceeds the critical strain value. In other words ϕ_i (varying between values 0 and 1) represents the extent of damage across edge i. A value of $\phi_i = 1$ corresponds to the undamaged case, and $\phi_i = 0$ denotes failure of the edge. One can place a damage criterion on either strains or forces. This simple damage criterion is representative of brittle failure.

$$\phi_i = \begin{cases} \bar{\varepsilon}_i < \varepsilon_{\text{critical}} & \phi_i = 1 \\ \bar{\varepsilon}_i \geq \varepsilon_{\text{critical}} & \phi_i = 0 \end{cases} \tag{2.35}$$

This type of nonlocal damage criterion have previously been used in the literature [35] in finite element formulation of continuum damage mechanics.

Equations (2.33), and (2.35) correspond to the situation in which the element size is significantly smaller than the zone size (case (1) in figure 2.4a). If the element size happens to be on the order of the zone size (case (2) in figure 2.4a), then the Eq. (2.33) reduces to the strain along the edge and the nonlocal damage criterion reduces to a local damage criterion.

$$\varepsilon_i = \mathbf{e}_i \cdot \boldsymbol{\varepsilon}\, \mathbf{e}_i \geq \varepsilon_{\text{critical}} \tag{2.36}$$

Figure 2.4b shows an edge for which the strain has exceeded the critical value and crack has already formed. If the strain in the neighboring edges also exceeds the critical value the crack can propagate into the neighboring edges.

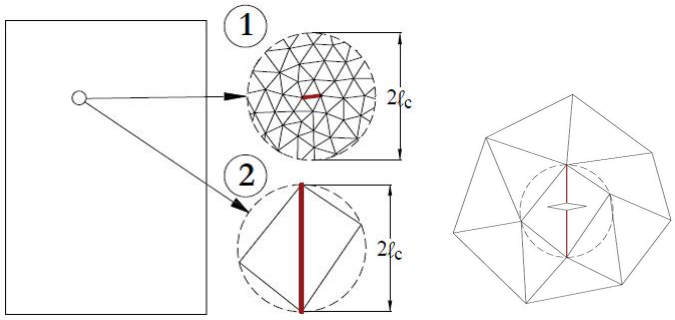

(a) (b)

Figure 2.4: (a) The figure shows the relative value of the element size to the zone size. If the element size is smaller than the zone size, nonlocal damage criterion and weighted averaged strain should be used. If, on the other hand, the element size is equal or larger than the zone size, the nonlocal damage criterion reduces to a local criterion, (b) The figure shows an edge failing when imposed to the local damage criterion.

One could apply a stress–based damage criterion for the study of damage. The reason why a strain–based damage criterion is chosen in this preliminary result is to avoid the possibility of healing after crack propagation.

2.3.2 Damage Criterion Imposed on GraFEA

In this proof of concept study it is assumed that the element size is of the same order of the zone size, and a local damage criterion is utilized to assess the feasibility of studying damage using GraFEA. The nonlocal damage criterion of Eq. (2.35) simplifies as

$$\phi_i = \begin{cases} \varepsilon_i < \varepsilon_{\text{critical}} & \phi_i = 1 \\ \varepsilon_i \geq \varepsilon_{\text{critical}} & \phi_i = 0 \end{cases} \tag{2.37}$$

This damage criterion will cause softening in the material until it it becomes unstable (the displacement increases with no further increase in the force).

In section 2.2, the strain energy density for an element in a discretized continuum was derived in terms of the strains along the edges of the element (Eq. (2.13)). One can use $U_0(\varepsilon_1, \varepsilon_2, \varepsilon_3)$ and impose the damage criterion ϕ_i along the edges to construct the strain energy density in the damaged state:

$$\begin{aligned} U_0^d &= U_0^d(\phi_1\varepsilon_1, \phi_2\varepsilon_2, \phi_3\varepsilon_3) \\ &= A_{11}(\phi_1\varepsilon_1)^2 + A_{22}(\phi_2\varepsilon_2)^2 + A_{33}(\phi_3\varepsilon_3)^2 \\ &\quad + A_{12}\phi_1\varepsilon_1\phi_2\varepsilon_2 + A_{23}\phi_2\varepsilon_2\phi_3\varepsilon_3 + A_{31}\phi_3\varepsilon_3\phi_1\varepsilon_1 \end{aligned} \tag{2.38}$$

where coefficients A_{ij} were previously defined in Eq. (2.14). Superscript "d" corresponds to the damaged state. Using Eq. (2.38) the stresses are derived to be a quadratic function of ϕ_i.

$$\sigma_i^{*d} = \frac{\partial U_0}{\partial \varepsilon_i^*} = \frac{\partial U_0}{\partial \varepsilon_j}\frac{\partial \varepsilon_j}{\partial \varepsilon_i^*} \tag{2.39}$$

with

$$\frac{\partial U_0}{\partial \varepsilon_j} = 2A_{jj}\phi_j^2\varepsilon_j + \sum_{k=1,k\neq j}^{3} A_{jk}\phi_j\phi_k\varepsilon_k, \quad A_{ij} = A_{ji} \tag{2.40}$$

where no summation on repeated indices is assumed. $\frac{\partial \varepsilon_j}{\partial \varepsilon_i^*}$ is derived using Eq. (2.2). Finally, one

gets:

$$\boldsymbol{\sigma}^{*d} = \mathbf{T}^T \frac{\partial U_0}{\partial \boldsymbol{\varepsilon}} \tag{2.41}$$

where $\mathbf{T}$ is the transformation matrix of Eq. (2.5), $\boldsymbol{\sigma}^{*d}$, and $\frac{\partial U}{\partial \varepsilon_i}$ are elaborated in the following:

$$\boldsymbol{\sigma}^{*d} = \begin{Bmatrix} \sigma^d_{xx} \\ \sigma^d_{yy} \\ \sigma^d_{xy} \end{Bmatrix}, \quad \frac{\partial U_0}{\partial \boldsymbol{\varepsilon}} = \begin{Bmatrix} 2A_{11}\phi_1^2\varepsilon_1 + A_{12}\phi_1\phi_2\varepsilon_2 + A_{13}\phi_1\phi_3\varepsilon_3 \\ 2A_{22}\phi_2^2\varepsilon_2 + A_{12}\phi_1\phi_2\varepsilon_1 + A_{23}\phi_2\phi_3\varepsilon_3 \\ 2A_{33}\phi_3^2\varepsilon_3 + A_{13}\phi_1\phi_3\varepsilon_1 + A_{23}\phi_2\phi_3\varepsilon_2 \end{Bmatrix} \tag{2.42}$$

This can be rewritten in matrix form as follows:

$$\boldsymbol{\sigma}^{*d} = \mathbf{T}^T \boldsymbol{\Phi} \mathbf{H} \boldsymbol{\varepsilon}^d \tag{2.43}$$

where

$$\boldsymbol{\Phi} = \begin{bmatrix} \phi_1 & 0 & 0 \\ 0 & \phi_2 & 0 \\ 0 & 0 & \phi_3 \end{bmatrix}, \quad \mathbf{H} = \begin{bmatrix} 2A_{11} & A_{12} & A_{13} \\ A_{12} & 2A_{22} & A_{23} \\ A_{13} & A_{23} & 2A_{33} \end{bmatrix}, \quad \boldsymbol{\varepsilon}^d = \boldsymbol{\Phi}\boldsymbol{\varepsilon} = \begin{Bmatrix} \phi_1\varepsilon_1 \\ \phi_2\varepsilon_2 \\ \phi_3\varepsilon_3 \end{Bmatrix} \tag{2.44}$$

It can be shown that $\mathbf{H}$ can be written as:

$$\mathbf{H} = \mathbf{T}^{-T} \mathbf{C} \mathbf{T}^{-1} \tag{2.45}$$

Therefore, Eq. (2.43) will simplify to:

$$\boldsymbol{\sigma}^{*d} = \mathbf{T}^T \boldsymbol{\Phi} \mathbf{T}^{-T} \mathbf{C} \mathbf{T}^{-1} \boldsymbol{\Phi} \boldsymbol{\varepsilon} \tag{2.46}$$

2.3.3 Nodal Forces in the Damaged State

Equations (2.21) and (2.41) can be combined to derive the forces along the edges in the case of the damaged element. Note that the definition of the forces follows Eq. (2.19). It is assumed that

the term $\frac{\partial \varepsilon_j^*}{\partial d_k}\frac{\partial d_k}{\partial u_i}$ is not affected by damage variables ϕ_i. Therefore, using Eqs. (2.21) and (2.41) the relation between the forces and the strains in the edges in damaged condition will be:

$$\begin{aligned}\mathbf{F}^d =& hA\mathbf{B}^T\mathbf{T}^T\mathbf{\Phi}\mathbf{H}\varepsilon^d \\ =& hA\mathbf{B}^T\mathbf{T}^T\mathbf{\Phi}\mathbf{H}\mathbf{\Phi}\boldsymbol{\varepsilon} \\ =& hA\mathbf{B}^T\mathbf{T}^T\mathbf{\Phi}\mathbf{H}\mathbf{\Phi}\mathbf{T}\boldsymbol{\varepsilon}^*\end{aligned} \tag{2.47}$$

Finally, the force matrix can be written as:

$$\mathbf{F}^d = hA\mathbf{B}^T\mathbf{T}^T\mathbf{\Phi}\mathbf{T}^{-T}\mathbf{C}\mathbf{T}^{-1}\mathbf{\Phi}\boldsymbol{\varepsilon} = hA\mathbf{B}^T\mathbf{T}^T\mathbf{\Phi}\mathbf{T}^{-T}\mathbf{C}\mathbf{T}^{-1}\mathbf{\Phi}\mathbf{T}\boldsymbol{\varepsilon}^* \tag{2.48}$$

where $\mathbf{B} = \mathbf{A}_2^T\mathbf{A}_1^T$.

2.3.4 Stiffness Matrix in the Damaged State

Similar to the derivations of subsection 2.2.4, the stiffness matrix can be derived in damaged state to be:

$$\mathbf{K}^d = hA\mathbf{B}^T\mathbf{T}^T\mathbf{\Phi}\mathbf{T}^{-T}\mathbf{C}\mathbf{T}^{-1}\mathbf{\Phi}\mathbf{T}\mathbf{B} \tag{2.49}$$

One can see that the damaged stiffness matrix ($\mathbf{K}^d$) is quadratically dependent on the damage variables ($\phi_\mathbf{i}$).

It is worth mentioning that if $\mathbf{\Phi}$ is set to the identity matrix $\mathbf{I}$ (no damage), Eqs. (2.46), (2.48), and (2.49) –for damaged stress, damaged force vector, and damaged stiffness matrix, respectively –will simplify to the corresponding equations in conventional FEM (Eqs. (2.28), (2.21), and (2.32), respectively).

2.3.4.1 Damage in a right triangular element

As an example, the effect of the changes in the damage variable ϕ_i on the stiffness matrix of a right triangular element is studied. Consider the right triangle of Figure 2.5. The stiffness matrix in original condition (no damage, $\phi_i = 1$, $i = 1, 2, 3$) is determined according to Eq. (2.50) (refer

to [51]). Equation (2.50) can also be derived by using Eq. (2.49) and setting $\mathbf{\Phi} = \mathbf{I}$.

$$\mathbf{K} = \begin{bmatrix} \frac{1}{2}\left(\frac{b}{a}c_{11} + \frac{a}{b}c_{66}\right) & \frac{1}{2}\left(c_{12} + c_{66}\right) & -\frac{1}{2}\frac{b}{a}c_{11} & -\frac{1}{2}c_{66} & -\frac{1}{2}\frac{a}{b}c_{66} & -\frac{1}{2}c_{12} \\ \frac{1}{2}\left(c_{12} + c_{66}\right) & \frac{1}{2}\left(\frac{a}{b}c_{22} + \frac{b}{a}c_{66}\right) & -\frac{1}{2}c_{12} & -\frac{1}{2}\frac{b}{a}c_{66} & -\frac{1}{2}c_{66} & -\frac{1}{2}\frac{a}{b}c_{22} \\ -\frac{1}{2}\frac{b}{a}c_{11} & -\frac{1}{2}c_{12} & \frac{1}{2}\frac{b}{a}c_{11} & 0 & 0 & \frac{1}{2}c_{12} \\ -\frac{1}{2}c_{66} & -\frac{1}{2}\frac{b}{a}c_{66} & 0 & \frac{1}{2}\frac{b}{a}c_{66} & \frac{1}{2}c_{66} & 0 \\ -\frac{1}{2}\frac{a}{b}c_{66} & -\frac{1}{2}c_{66} & 0 & \frac{1}{2}c_{66} & \frac{1}{2}\frac{a}{b}c_{66} & 0 \\ -\frac{1}{2}c_{12} & -\frac{1}{2}\frac{a}{b}c_{22} & \frac{1}{2}c_{12} & 0 & 0 & \frac{1}{2}\frac{a}{b}c_{22} \end{bmatrix} \tag{2.50}$$

Next, the evolution of the stiffness matrix is determined in Table 2.2 for different combinations

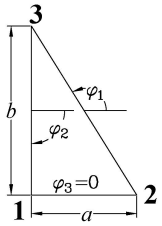

Figure 2.5: Arbitrary right triangle.

of ϕ_is (setting them either equal to one or zero). When all links are broken $\phi_1 = \phi_2 = \phi_3 = 0$, all of the terms of the stiffness matrix will turn to zero. The parametric equations for the damaged stiffness matrix of an arbitrary triangle can also be derived, but it will be parametrically very involved.

2.4 Numerical Examples

In this section, first the methodology of integrating GraFEA into conventional FEM is introduced. Next, two numerical examples are provided as the proof of concept. These are only preliminary results to examine the feasibility of using GraFEA to study of damage in brittle materials. More rigorous results are going to be studied in the future.

Table 2.2: Evolution of the stiffness matrix with the damage variable.

One Damaged Edge	**Two Damaged Edges**
$\phi_1 = 0,\ \phi_2 = \phi_3 = 1$	$\phi_1 = \phi_2 = 0,\ \phi_3 = 1$
$\mathbf{K}^d = \begin{bmatrix} \frac{1}{2}\left(\frac{b}{a}c_{11} + \frac{a}{b}c_{66}\right) & \frac{1}{2}\left(c_{12} + c_{66}\right) & -\frac{1}{2}\left(\frac{b}{a}c_{11} + \frac{a}{b}c_{66}\right) & 0 & 0 & -\frac{1}{2}\left(c_{12} + c_{66}\right) \\ \frac{1}{2}\left(c_{12} + c_{66}\right) & \frac{1}{2}\left(\frac{a}{b}c_{22} + \frac{b}{a}c_{66}\right) & -\frac{1}{2}\left(c_{12} + c_{66}\right) & 0 & 0 & -\frac{1}{2}\left(\frac{a}{b}c_{22} + \frac{b}{a}c_{66}\right) \\ -\frac{1}{2}\left(\frac{b}{a}c_{11} + \frac{a}{b}c_{66}\right) & -\frac{1}{2}\left(c_{12} + c_{66}\right) & \frac{1}{2}\left(\frac{b}{a}c_{11} + \frac{a}{b}c_{66}\right) & 0 & 0 & \frac{1}{2}\left(c_{12} + c_{66}\right) \\ 0 & 0 & 0 & 0 & 0 & 0 \\ 0 & 0 & 0 & 0 & 0 & 0 \\ -\frac{1}{2}\left(c_{12} + c_{66}\right) & -\frac{1}{2}\left(\frac{a}{b}c_{22} + \frac{b}{a}c_{66}\right) & \frac{1}{2}\left(c_{12} + c_{66}\right) & 0 & 0 & \frac{1}{2}\left(\frac{a}{b}c_{22} + \frac{b}{a}c_{66}\right) \end{bmatrix}$	$\mathbf{K}^d = \begin{bmatrix} \frac{1}{2}\left(\frac{b}{a}c_{11} + \frac{a}{b}c_{66}\right) & 0 & -\frac{1}{2}\left(\frac{b}{a}c_{11} + \frac{a}{b}c_{66}\right) & 0 & 0 & 0 \\ 0 & 0 & 0 & 0 & 0 & 0 \\ -\frac{1}{2}\left(\frac{b}{a}c_{11} + \frac{a}{b}c_{66}\right) & 0 & \frac{1}{2}\left(\frac{b}{a}c_{11} + \frac{a}{b}c_{66}\right) & 0 & 0 & 0 \\ 0 & 0 & 0 & 0 & 0 & 0 \\ 0 & 0 & 0 & 0 & 0 & 0 \\ 0 & 0 & 0 & 0 & 0 & 0 \end{bmatrix}$
$\phi_2 = 0,\ \phi_1 = \phi_3 = 1$	$\phi_2 = \phi_3 = 0,\ \phi_1 = 1$
$\mathbf{K}^d = \begin{bmatrix} \frac{1}{2}\left(\frac{b}{a}c_{11} + \frac{a}{b}c_{66}\right) & 0 & -\frac{1}{2}\frac{b}{a}c_{11} & -\frac{1}{2}c_{66} & -\frac{1}{2}\frac{a}{b}c_{66} & \frac{1}{2}c_{66} \\ 0 & 0 & 0 & 0 & 0 & 0 \\ -\frac{1}{2}\frac{b}{a}c_{11} & 0 & \frac{1}{2}\frac{b}{a}c_{11} & 0 & 0 & 0 \\ -\frac{1}{2}c_{66} & 0 & 0 & \frac{1}{2}\frac{b}{a}c_{66} & \frac{1}{2}c_{66} & -\frac{1}{2}\frac{b}{a}c_{66} \\ -\frac{1}{2}\frac{a}{b}c_{66} & 0 & 0 & \frac{1}{2}c_{66} & \frac{1}{2}\frac{a}{b}c_{66} & -\frac{1}{2}c_{66} \\ \frac{1}{2}c_{66} & 0 & 0 & -\frac{1}{2}\frac{b}{a}c_{66} & -\frac{1}{2}c_{66} & \frac{1}{2}\frac{b}{a}c_{66} \end{bmatrix}$	$\mathbf{K}^d = \begin{bmatrix} 0 & 0 & 0 & 0 & 0 & 0 \\ 0 & 0 & 0 & 0 & 0 & 0 \\ 0 & 0 & \frac{1}{2}\frac{a}{b}c_{66} & -\frac{1}{2}c_{66} & -\frac{1}{2}\frac{a}{b}c_{66} & \frac{1}{2}c_{66} \\ 0 & 0 & -\frac{1}{2}c_{66} & \frac{1}{2}\frac{b}{a}c_{66} & \frac{1}{2}c_{66} & -\frac{1}{2}\frac{b}{a}c_{66} \\ 0 & 0 & -\frac{1}{2}\frac{a}{b}c_{66} & \frac{1}{2}c_{66} & \frac{1}{2}\frac{a}{b}c_{66} & -\frac{1}{2}c_{66} \\ 0 & 0 & \frac{1}{2}c_{66} & -\frac{1}{2}\frac{b}{a}c_{66} & -\frac{1}{2}c_{66} & \frac{1}{2}\frac{b}{a}c_{66} \end{bmatrix}$
$\phi_3 = 0,\ \phi_1 = \phi_2 = 1$	$\phi_1 = \phi_3 = 0,\ \phi_2 = 1$
$\mathbf{K}^d = \begin{bmatrix} 0 & 0 & 0 & 0 & 0 & 0 \\ 0 & \frac{1}{2}\left(\frac{a}{b}c_{22} + \frac{b}{a}c_{66}\right) & \frac{1}{2}c_{66} & -\frac{1}{2}\frac{b}{a}c_{66} & -\frac{1}{2}c_{66} & -\frac{1}{2}\frac{a}{b}c_{22} \\ 0 & \frac{1}{2}c_{66} & \frac{1}{2}\frac{a}{b}c_{66} & -\frac{1}{2}c_{66} & -\frac{1}{2}\frac{a}{b}c_{66} & 0 \\ 0 & -\frac{1}{2}\frac{b}{a}c_{66} & -\frac{1}{2}c_{66} & \frac{1}{2}\frac{b}{a}c_{66} & \frac{1}{2}c_{66} & 0 \\ 0 & -\frac{1}{2}c_{66} & -\frac{1}{2}\frac{a}{b}c_{66} & \frac{1}{2}c_{66} & \frac{1}{2}\frac{a}{b}c_{66} & 0 \\ 0 & -\frac{1}{2}\frac{a}{b}c_{22} & 0 & 0 & 0 & \frac{1}{2}\frac{a}{b}c_{22} \end{bmatrix}$	$\mathbf{K}^d = \begin{bmatrix} 0 & 0 & 0 & 0 & 0 & 0 \\ 0 & \frac{1}{2}\left(\frac{a}{b}c_{22} + \frac{b}{a}c_{66}\right) & 0 & 0 & 0 & -\frac{1}{2}\left(\frac{a}{b}c_{22} + \frac{b}{a}c_{66}\right) \\ 0 & 0 & 0 & 0 & 0 & 0 \\ 0 & 0 & 0 & 0 & 0 & 0 \\ 0 & 0 & 0 & 0 & 0 & 0 \\ 0 & -\frac{1}{2}\left(\frac{a}{b}c_{22} + \frac{b}{a}c_{66}\right) & 0 & 0 & 0 & \frac{1}{2}\left(\frac{a}{b}c_{22} + \frac{b}{a}c_{66}\right) \end{bmatrix}$

2.4.1 Methodology

The methodology of integrating GraFEA into conventional FEM is graphically shown in Figure 2.6, where N_{broke} is the total number of broken edges at each step, N_{new} is the number of new broken edges produced in the current step, and I is the step counter.

In the numerical examples provided next, the mesh is generated using a 2D mesh generator by the name *distmesh*. Distmesh makes use of the analogy between a simplex mesh and a truss structure to build the mesh[3]. The edges of the triangles are assumed to be the truss elements and the vertices are the corresponding nodes. The truss structure is then solved by assuming a suitable force–displacement relationship at each step to reach equilibrium. Delaunay triangulation is also used to avoid generation of problematic elements with narrow geometries and to adjust the topology. The mesh generator code has the ability to produce high quality meshes with triangular elements with nearly equal edge lengths.

2.4.2 Rectangular Plate with a Circular Hole

A rectangular plate of dimensions $W \times L$ made of a homogeneous isotropic material is considered (Figure 2.7a) under plane stress conditions (with unit thickness). The plate is constrained in the vertical direction at the bottom, and tensile displacement boundary conditions ($v_y = v_0 > 0$) are applied to the top. To maintain the symmetry of the problem, the node located at the center–line of the bottom of the plate is constrained in the horizontal direction. The left and right side of the plate are traction free. A circular hole of radius r is assumed at the center of the plate (Figure 2.7a). The geometric and material properties used in this numerical examples are listed in the following:

$$W = 4, \quad L = 6, \quad r = 0.8, \quad E = 3 \times 10^6, \quad \nu = 0.25, \quad \varepsilon_{critical} = 0.005 \tag{2.51}$$

Figure 2.7 represents the evolution of the broken edges for the plate under consideration. The figure shows the original symmetric mesh[4] with black lines, and the broken edges are represented

[3] *Distmesh* mesh generator. Available from `http://persson.berkeley.edu/distmesh`.

[4] Symmetry with respect to the vertical axis.

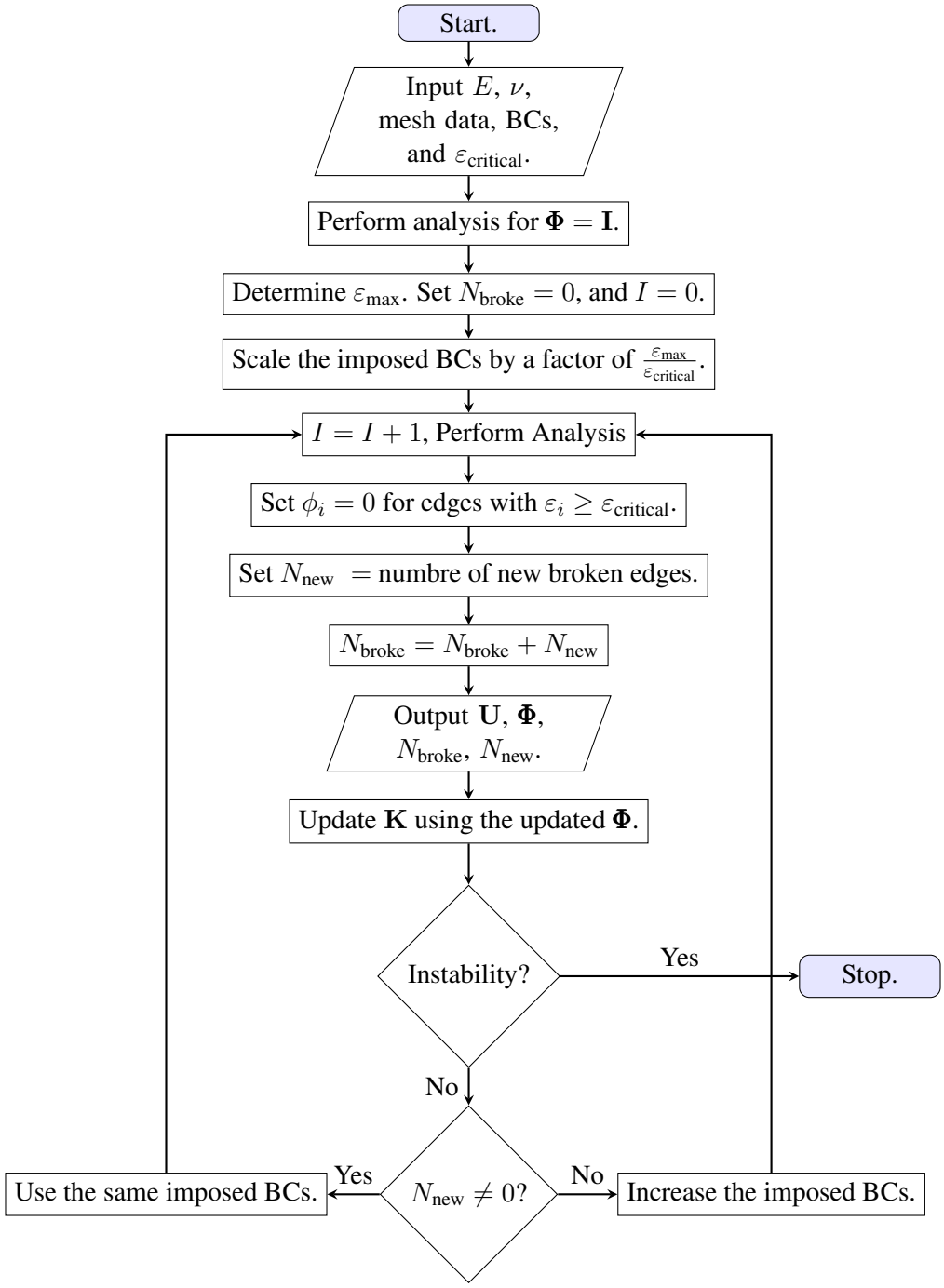

Figure 2.6: Flowchart for performing damage analysis using GraFEA with N_{broke} as the total number of broken edges at each step, N_{new} as the number of new broken edges produced in the current step, and I as the step counter.

as white lines. It is worth mentioning that crack grows perpendicular to the broken edges. Figure 2.7b corresponds to the first step in the analysis in which $\varepsilon_{\max}$ reaches $\varepsilon_{\text{critical}}$ in the first edge/set of edges (after scaling the imposed boundary conditions). The subsequent figures are for increasing I, where I was introduced in Subsection 2.4.1 as the step counter (rounds of analysis). As it can be seen, the crack initiates at the zones with highest stress intensity and propagates towards the edges of the plate. The crack path should not necessarily be a smooth line.

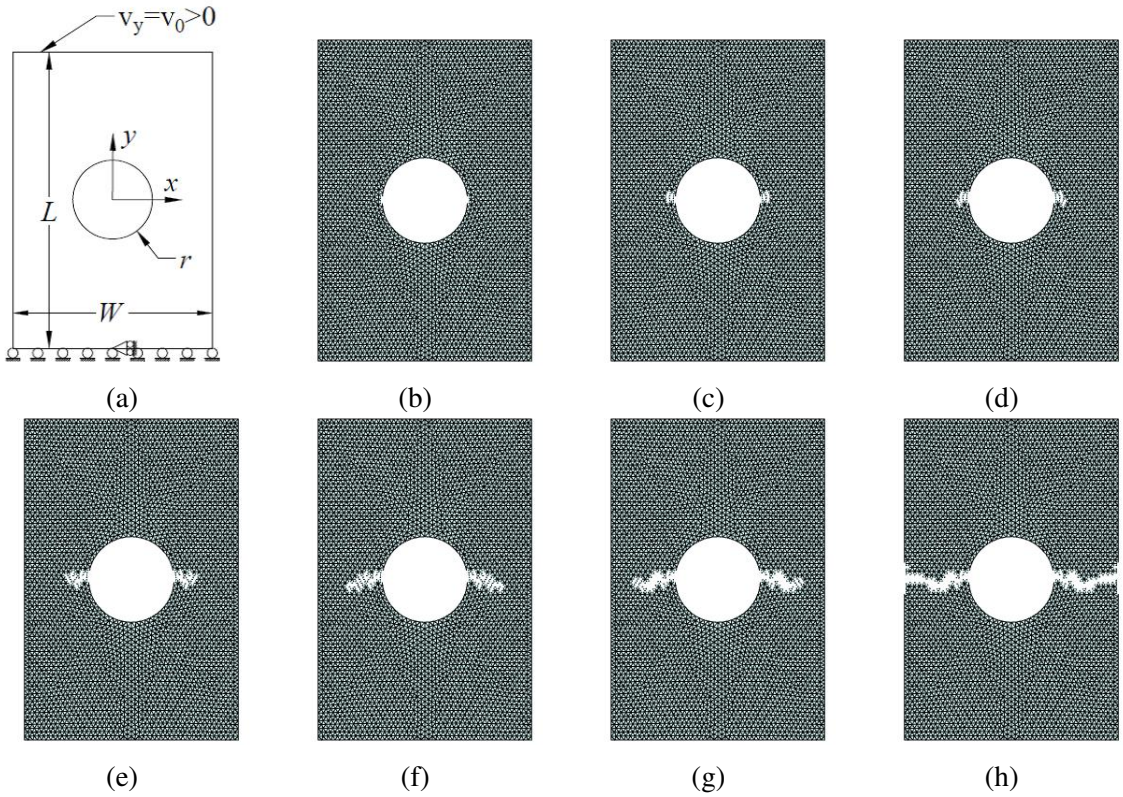

Figure 2.7: Evolution of the broken edges for a rectangular plate with a circular hole, (a) The plate under the application of increasing tensile displacement boundary conditions (b) $I = 1$ (c) $I = 6$ (d) $I = 11$ (e) $I = 16$ (f) $I = 21$ (g) $I = 26$ (h) $I = 41$.

Evolution of the force–displacement curve at the top boundary of the plate is shown in Figure 2.8. The top boundary of the plate is imposed to a specified tensile displacement boundary condition, the corresponding force is determined by summing up the nodal forces calculated at

the nodes located at the top boundary. The red dot shown on Figure 2.8 corresponds to the point where the first set of edges are broken. It can be seen that when new edges are broken at a specific step, a visible reduction on the force–displacement curve is noticed. This reduction is higher if the number of the additional broken edges is larger. Figure 2.8 shows two significant reductions in the force–carrying capacity (during which the number of broken edges is increased) of the plate before total failure (force getting to zero). After these reductions, the force continues increasing with the increase in the imposed tensile displacement boundary condition, however, the slope of the force–displacement curve (which is to some extent representative of the stiffness of the plate) in the second portion has significantly reduced (about 43%) as compared to the first portion. This shows a substantial decline in the force–carrying capacity upon the increase in the number of broken edges.

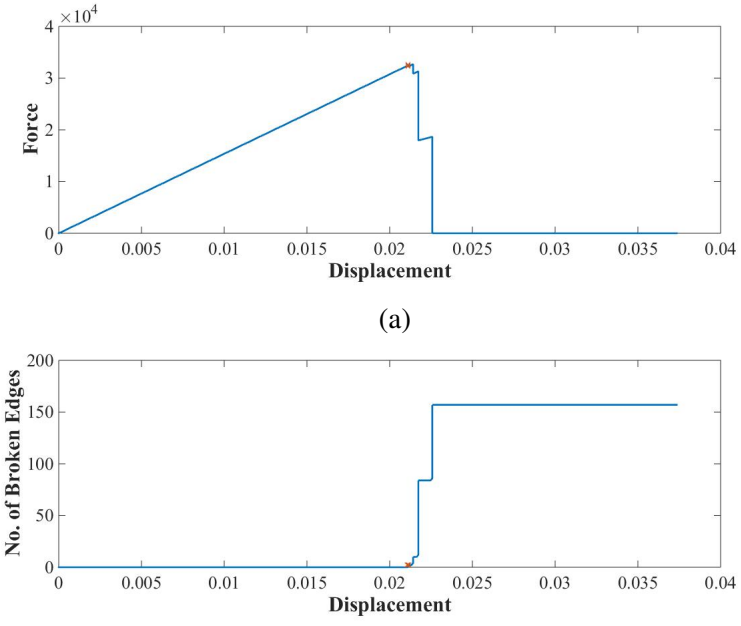

Figure 2.8: (a) Force–displacement curve, (b) Number of broken edges for a rectangular plate with a circular hole imposed to increasing tensile displacement boundary conditions applied at the top boundary.

2.4.3 Rectangular Plate with an Elliptic Hole

A rectangular plate with material properties, and geometric dimensions similar to those mentioned in section 2.4.2 is considered, the difference is that in this case an elliptic hole is assumed at the center of the plate. The constraints and the imposed boundary conditions are similar to those for the circular hole. Figure 2.9a shows the notation used for the dimensions of the elliptic hole. For this numerical example the following values are assumed for a and b. The rest of the parameters (material parameters, dimensions, and critical strain) are chosen to be the same as that of the plate with a circular hole (Eq. (2.51)).

$$a = 0.8, \quad b = 0.2 \tag{2.52}$$

Figure 2.9b–h displays the evolution of cracks for the rectangular plate of Figure 2.9a. The figures show that as the crack reaches the ends of the plate, some form of crack branching initiates near the ends.

Finally the force–displacement curve for the top boundary of the rectangular plate in consideration is pictured in Figure 2.10. Once again the evolution of the force–carrying capacity is studied under the imposition of the increasing tensile displacement boundary condition. One can see that for the case of a plate with an elliptic hole the failure happens more abruptly. The number of broken edges increase significantly at some point to the extent that the plate gets to total failure.

2.5 Chapter Summary and Conclusions

In this study, using the idea presented by Reddy and Srinivasa [16] first conventional FEM is transformed into a nonlocal network named as the graph–based finite element approach (in short GraFEA). Reddy and Srinivasa [16] proved that this could be done, but this is the first study in numerical implementation of this idea. A nonlocal strain–based fracture criterion is integrated into GraFEA for the study of damage in brittle materials which is based on the idea of weakest link statistics proposed by Ritchie, Knott, and Rice [20], and Lin, Evans, and Ritchie [21]. The damage criterion simplifies to a local criterion when the element size is almost of the order of the

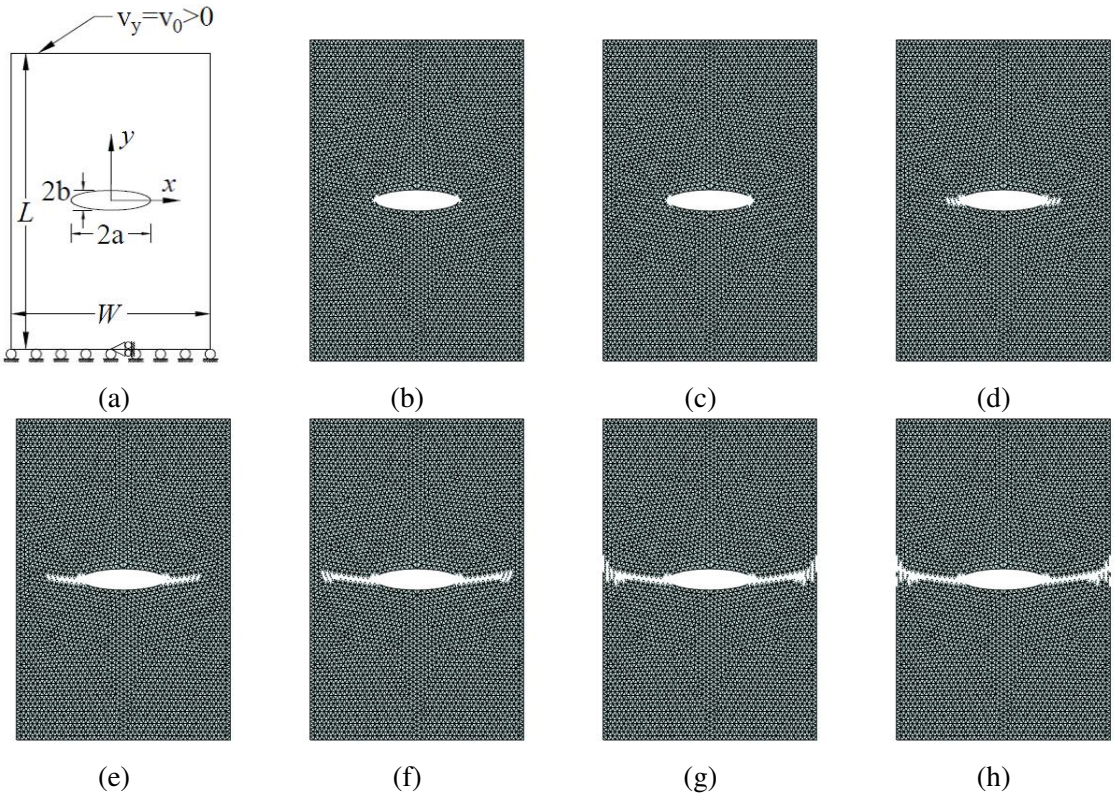

Figure 2.9: Evolution of the broken edges for a rectangular plate with an elliptic hole (a) The plate under the application of displacement boundary conditions (b) $I = 1$ (c) $I = 101$ (d) $I = 114$ (e) $I = 118$ (f) $I = 122$ (g) $I = 124$ (h) $I = 126$.

fracture zone size. This strategy of individual edge failure (while retaining the nonlocal nature of the network) as opposed to element failure will significantly simplify the study of damage within materials compared to the existing continuum–based methods in the literature. The fact that the failure criterion is imposed directly on the discrete body without inheriting it from a continuum is one of the important features of GraFEA.

Two numerical examples are presented for the case of rectangular plates with a circular and an elliptic hole as a means to illustrate the capability of GraFEA to study damage in brittle materials. The results show that GraFEA has a potential to predict damage within materials in a straightforward manner.

The aim of the present study is a proof of concept for this approach (integrating link–based damage into a nonlocal network presentation of a continuum, GraFEA). A detailed study on mesh

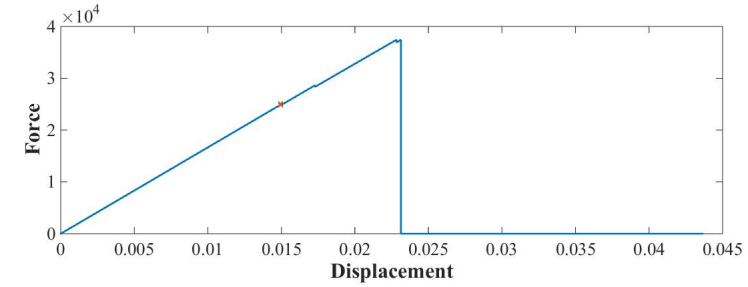

(a)

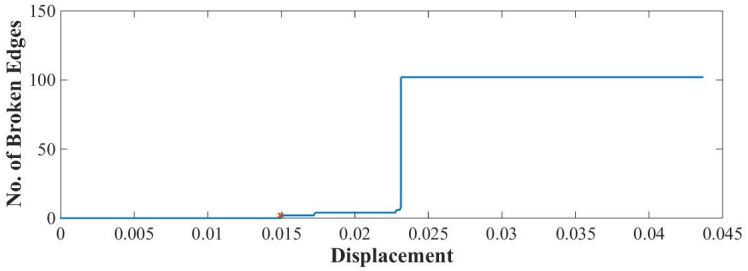

(b)

Figure 2.10: (a) Force–displacement curve, (b) Number of broken edges for a rectangular plate with an elliptic hole imposed to the increasing tensile displacement boundary conditions applied at the top boundary.

dependency and validation of the results with experimental results will be addressed in future works. However, in a slightly different context Reusch, Svendsen, and Klingbiel [52] have shown that a nonlocal fracture criterion similar to the one used in the present study results in a mesh independent behavior. The authors plan to carry out similar mesh–independency studies in near future, but their expectation is that with the new length scale introduced to the model, the findings will be similar to those of Reusch, Svendsen, and Klingbiel [52].

As already known to the readers, even for nominally similar experimental samples, the crack paths do not completely coincide due to the randomness of flaws within the materials. Therefore, the authors believe that the existing deterministic approaches to damage and fracture do not provide the engineers with useful results. On the other hand, with a probabilistic approach the probability of failure can be mapped for a problem, which is a more valuable information. The proposed method has the potential to incorporate a probabilistic approach as opposed to the deterministic methods proposed in the literature.

3. A NONLOCAL FRACTURE CRITERION AND ITS EFFECT ON MESH DEPENDENCY OF GRAFEA

3.1 Introduction

One of the important features to be investigated for any computational method proposed for the study of fracture in solids is the convergence of the numerical results with mesh refinement and whether or not the results are independent of the underlying mesh (both in terms of refinement and orientation). Several studies have been performed for over 30 years to identify the causes and the measures of eliminating the mesh sensitivity of the numerical methods.

Continuum damage mechanics gained popularity in the numerical implementation of fracture due to the appealing features of using a continuum approach and its ability to study the emerge and growth of multiple cracks at the same time as opposed to dealing with the cracks in a discrete segment-by-segment one-crack-at-a-time manner (i.e. cohesive zone models, or XFEM). One major concern in damage problems is the strain localization which is the direct result of the strain-softening-induced instability caused by the loss of ellipticity of the governing equations in static problems[1]. As a result, the strain softening problems will show physically meaningless results, where the damage localizes to a zero-volume surface and the energy dissipated in fracture converges to zero. One of the first studies on the effect of the loss of stability and strain localization on the finite element implementation of a strain softening problem dates back to 1975 [54] in which Bažant showed that the results exhibited strong dependence on the size of the elements in the finite element mesh. In this study, the fracture in the finite element models of strain softening materials localizes to one element irrespective of its size, and the amount of dissipated energy decreases correspondingly with further reduction in the element size.

The new computational framework by the name graph-based finite element approach (GraFEA) was proposed [15] for the study of fracture in solids. The key feature about GraFEA is that it pictures the discretized finite element problem as a network of nodes with the edges of the elements

[1] and the change from hyperbolic equations to elliptic equations in wave propagation problems [53].

serving as the links between the nodes [16]. This representation of the finite element scheme enables the imposition of a discrete fracture criterion on the edges. Consequently, GraFEA benefits from the simplicity of using a continuum approach in modeling the problem, and at the same time it circumvents the issues of the existing continuum methods on dealing with discontinuities caused by fracture by adopting a straightforward discrete approach. The original formulation of GraFEA [15] was built upon a local fracture criterion which is well-known to lead to mesh dependency in most numerical frameworks. It is shown through a set of numerical examples that the mesh dependency is also true about GraFEA when using a local fracture criterion.The *purpose* of this study is to incorporate an integral-type nonlocal fracture criterion into GraFEA to examine its efficiency in resolving the mesh sensitivity induced by strain localization. It is demonstrated that adopting a nonlocal fracture criterion will eliminate the mesh dependency in a global sense.

Several studies were devoted to the clarification of the strain localization phenomena in fracture problems in materials with strain softening constitutive equation studied via continuum damage mechanics. Some of the proposed approaches to eliminate the mesh dependency induced by strain localization are listed in the following:

1. Imposing a lower limit on the size of the elements: this remedy was first discussed in a paper by Bažant [54] and later employed in the crack band model [55, 56]. The crack band model is capable of predicting the global force-displacement relationship without convergence to zero energy dissipation with mesh refinement, however, the fracture volume will localize to a surface with further mesh refinement [35].

2. Introduction of strain-rate dependence (artificial viscosity): this method (as proposed by Needleman [57]) introduces a length scale into the problem in an indirect manner. The method is successful in retaining the ellipticity of the governing equations, however, it is only applicable for problems within short periods of time [35, 58] and it cannot be used as a remedy in a general sense.

3. Use of weakly nonlocal theories, i.e. higher order gradients [53, 59]: the methods falling into

this approach can generally be divided into two categories: namely explicit gradient models, and implicit gradient models. In the explicit models the stress at each point depends not only on the strain at that point, but also on a set of higher order gradients of the strain. The gradient terms in the explicit models will result in weak nonlocality where the nonlocal interactions are limited to an infinitesimal domain. On the other hand, implicit gradient models are such that the nonlocal stress is determined by the solution of a boundary value problem. In fact, implicit models can be written in the form of an integral-type nonlocal model where the weight function is the Green's function of the boundary value problem [60]. According to a study by Peerlings et al. [61], the results from implicit gradient models are similar to integral-type nonlocal models, and the implicit models are successful at resolving the issues with strain localization. However, the results from explicit gradient models are problematic in the sense that they give unbounded wave velocity and the crack growth rate is instantaneous (i.e. singular) [60, 61]. Also explicit gradient models introduce additional boundary conditions which are not physically tangible introducing further implications in the numerical modeling.

4. Use of strongly nonlocal theories, i.e. integral theories: this method for resolving the issue of strain localization in fracture problems was initially introduced in the works of Bažant and his coworkers [58, 62, 63]. In this approach the strain localization is removed by imposing nonlocal averaging on a parameter over a characteristic zone. Jirásek [64] showed that depending on the choice of the variable for nonlocal averaging the results can be different. Therefore, the level of effectiveness of the nonlocal averaging depends on the chosen variable [64].

It is worth mentioning that explicit higher order gradient models in terms of strains can be written in a form similar to integral-type nonlocal models in terms of stress, whereas, integral-type nonlocal models in terms of strain can be written in a form similar to explicit higher order gradient models in terms of stress (refer to [61, 65, 66] for further information).

The extended finite element method (XFEM) [9–11] and the interelement crack method (sometimes referred to as cohesive zone models[2]) [7, 8] are two other major computational methods for

[2]Cohesive zone models can be a misleading terminology, because cohesive zone models are also utilized in other

the study of fracture. There is little published data on mesh sensitivity of the fracture results from XFEM, yet it has a significant drawback: the enrichment is only applied to the nodes influenced by the crack, therefore, by the end of each step the crack should be monitored to update the enrichment of the new nodes. Also the nodes have different degrees of freedom depending on their location. The interelement crack method on the other hand is shown to be mesh sensitive [67]. In this method the cracks are only allowed to propagate across the edges of the elements, therefore, the crack path cannot be arbitrary in nature. Consequently, the interelement crack method is only suitable for the cases when the crack path is known in advance and the body is meshed such that the edges of the elements coincide with the crack path [68].

During the past decade, a new integral-type nonlocal model has gained popularity among researchers. Peridynamic theory [13, 69] is a nonlocal theory which is capable of addressing continuous displacement and spontaneous discontinuity through a single equation of motion. Therefore, it was assumed a suitable computational framework for the study of fracture in solids. Its original form (i.e. bond-based peridynamic theory [13]) suffers from a serious limitation: the Poisson's ratio is limited to 0.25[3]. Later, state-based peridynamic theory [69] was introduced to eliminate this shortcoming[4]. Several studies demonstrated that perdiynamics can result in mesh dependent or spurious cracks depending on the choice of the horizon (i.e. radius of the nonlocal zone) to the grid size ratio (δ/h), and a minimum δ/h is required to retain mesh independency in PD simulations [75–81]. This issue, which is observed in both bond-based and state-based peridynamics, is a serious drawback for peridynamics considering that the method was originally introduced as a replacement for conventional continuum mechanics for the study of problems with existing or spontaneous discontinuity. Later, Seleson, Du, and Parks [73] showed that even in the absence

methods (e.g. XFEM [11]).

[3]To further elucidate the seriousness of this shortcoming assume an isotropic elastic material with two independent material parameters: Poisson's ratio ν, and modulus of elasticity E. In the case of linear elasticity, one can non-dimensionalize the response with respect to E, however, this is not feasible for ν. Therefore, in the case of linear elasticity the parameter which distinguishes the responses of different materials is the Poisson's ratio which cannot be varied using bond-breakage models.

[4]At the continuum level, peridynamics theoretically reduces to conventional continuum mechanics in the limit of the zero characteristic zone [70–72]; however, the existence of such a correspondence at the discrete level is debatable [73]. Tian and Du [74] demonstrated that in general the results of discretized peridynamics do not automatically converge to those of local continuum mechanics.

of cracks the accuracy of the results of nearest-neighbor discretized peridynamics depends on the choice of quadrature weights, otherwise mesh dependent results will be achieved.

In the introductory paper on GraFEA [15] a local fracture criterion was implemented on the network representation of FEM to demonstrate the feasibility of studying fracture in solids using GraFEA. The present chapter has two primary goals: 1. to investigate the influence of augmenting a nonlocal fracture criterion in GraFEA, 2. to examine whether or not the nonlocal fracture criterion eliminates mesh dependency. The remainder of this chapter proceeds as follows: section 2 provides a brief introduction on the theoretical background of GraFEA and the method of integration of a discrete fracture criterion into the network representation of FEM. In section 3 the local fracture criterion of the original formulation is upgraded to a nonlocal fracture criterion. Because of the ease of integrating an integral-type nonlocal model into a computational framework (without the need for imposing further constrains in the form of boundary conditions) and its efficiency in resolving the strain localization issue (with the proper choice of the variable), an integral nonlocality has been chosen in this study as the means of eliminating the mesh dependency in GraFEA. Section 4 presents numerical examples to address the above-mentioned main goals of this study. Finally, section 5 summarizes the concluding remarks.

3.2 Theoretical Background of GraFEA

Reddy and Srinivasa [16] proved that for any hyperelastic material the nodal forces of a discretized domain are directed along the edges of the element, and the value of the edge-directed forces can be expressed in terms of the strains along the edges. This representation of conventional FEM resembles a network where only the nodes and the distance between them (edge length) is of interest. It is worth noting that any line connecting two distinct nodes of an element is called an edge (Figure 2.2). The network representation of GraFEA is nonlocal in the sense that the force along edge i does not only depend on the strain along that edge, but also on the collective behavior of the strains along the set of edges in the elements sharing edge i. This is the reason why the nonlocal network of GraFEA, unlike the existing bond-breakage models in the literature, places no limitations on the Poisson's ratio of the material to be modeled.

The idea of weakest link statistics [20, 21] is used to impose an edge-based discrete fracture criterion on the nonlocal network representation of GraFEA. Ritchie, Knott, and Rice [20] showed that for a brittle type of material (cleavage fracture in mild steel at very low temperatures) fracture does not only depend on the stress at the tip of the crack, but on the average stress over a characteristic distance ahead of the crack tip. By assuming a region ahead of the crack tip, the competition between the far-field behavior (where more cracked particles are available but the stress values are lower) with that of the near-tip behavior (where the number of eligible particles is less, but stresses are higher) is accounted for [21]. Recently, Mao, Talamini, and Anand [82] stated that fracture in elastomeric materials is a nonlocal phenomenon, and crack propagation occurs when the fracture criterion is met at a distance ℓ ahead of the crack tip, and not the crack tip itself. This is a similar argument to the one by Ritchie, Knott, and Rice [20] on the study of mild steel. Note that a nonlocal criterion is not equivalent to crack propagating from an isolated point ahead of the crack tip [82].

The damaged stiffness matrix in GraFEA is determined according to Eq. (3.1) (refer to reference [15] for further information). Note that Eq. (3.1) corresponds to a plane elasticity problem and a linear triangular element with constant strains. However, GraFEA in general is not limited to a certain constitutive equation (as long as the material is hyperelastic) or element type (refer to the general proof in reference [16]).

$$\mathbf{K}^d = hA\mathbf{B}^T\mathbf{T}^T\mathbf{\Phi}\mathbf{T}^{-T}\mathbf{C}\mathbf{T}^{-1}\mathbf{\Phi}\mathbf{T}\mathbf{B} \tag{3.1}$$

where h and A are the thickness, and the area of the element, respectively. $\mathbf{B}$ is the matrix relating the elasticity strains to the nodal displacement of the finite element mesh [51], and $\mathbf{C}$ is the elasticity matrix. $\mathbf{T}$ serves as the transformation matrix between the set of linearized strains $(\varepsilon_{xx}, \varepsilon_{yy}, \gamma_{xy})$

and the set of edge-directed normal strains $(\varepsilon_1, \varepsilon_2, \varepsilon_3)$ which is determined to be [15]:

$$\begin{Bmatrix} \varepsilon_1 \\ \varepsilon_2 \\ \varepsilon_3 \end{Bmatrix} = \mathbf{T} \begin{Bmatrix} \varepsilon_{xx} \\ \varepsilon_{yy} \\ \gamma_{xy} \end{Bmatrix}, \qquad \mathbf{T} = \begin{bmatrix} \frac{1}{L_1^2} & 0 & 0 \\ 0 & \frac{1}{L_2^2} & 0 \\ 0 & 0 & \frac{1}{L_3^2} \end{bmatrix} \begin{bmatrix} \gamma_1^2 & \beta_1^2 & -\gamma_1\beta_1 \\ \gamma_2^2 & \beta_2^2 & -\gamma_2\beta_2 \\ \gamma_3^2 & \beta_3^2 & -\gamma_3\beta_3 \end{bmatrix} \tag{3.2}$$

in which ε_i is the strain along edge i connecting nodes j and k (Figure 2.2), and γ_i and β_i are the terms used in FE interpolation functions for a linear triangular element [51].

$$\beta_i = y_j - y_k, \qquad \gamma_i = -\left(x_j - x_k\right) \tag{3.3}$$

The remaining variable in Eq. (3.1) to be introduced is $\mathbf{\Phi}$ which is a diagonal matrix containing the edge-based damage variables [15]. The damage variable for edge i only acquires two values: 1 corresponding to an intact edge, and 0 corresponding to a broken edge. Note that by setting $\mathbf{\Phi} = \mathbf{I}$ Eq. (3.1) simplifies to the stiffness matrix for conventional FEM, therefore, GraFEA in undamaged situation yields the same results as FEM. One can notice that the stiffness matrix is symmetric and it is quadratically dependent on the damage variables, Φ_i.

3.3 Nonlocal Fracture Criterion

In the original formulation of GraFEA [15] a local fracture criterion was used, i.e. the answer to the question that whether edge i is broken or not was answered solely based on the comparison of the strain along that edge with a critical strain. An edge was considered broken as soon as the strain along that edge exceeded the critical strain.

In this chapter a nonlocal edge-directed strain-based fracture criterion is introduced to eliminate the mesh dependecy observed in the results from the local fracture criterion. The core idea is that if the weighted averaged strain in any given direction over a characteristic zone exceeds a critical value, $\varepsilon_{\text{critical}}$, fracture happens. In other words, a link in the network will fail if:

$$\bar{\varepsilon}_i = \mathbf{e}_i \cdot \left[\int_{\|\mathbf{x}-\mathbf{x}_0\| \leq \ell_c} \omega\left(\mathbf{x} - \mathbf{x}_0\right) \boldsymbol{\varepsilon}^*\left(\mathbf{x}_0\right) d\Omega \right] \mathbf{e}_i \geq \varepsilon_{\text{critical}} \tag{3.4}$$

where $\mathbf{e}_i$ is the unit vector along the edge of interest (Figure 2.2.b), ℓ_c is the characteristic distance (Figure 2.4.a), $\omega(\mathbf{x}-\mathbf{x}_0)$ is the averaging weight function, $\boldsymbol{\varepsilon}^*(\mathbf{x}_0)$ is the vector of linearized strains, and $\bar{\varepsilon}_i$ is the weighted-averaged normal strain for edge i. Existence of a characteristic length in the fracture criterion results in a size effect which can serve as the transition between micro to macro fracture [19]. The weight function must satisfy the following constraint over the characteristic zone of radius ℓ_c:

$$\int_{\|\mathbf{x}-\mathbf{x}_0\|\leq\ell_c} \omega(\mathbf{x}-\mathbf{x}_0)\, d\Omega = 1 \tag{3.5}$$

A uniform weight function is chosen in this study, therefore, equation (3.5) is simplified as follows. One could also use distance-decaying weight functions to consider the decrease in the influence of the elements over each other with increasing distance.

$$\omega(\mathbf{x}-\mathbf{x}_0) = \frac{1}{A_{\text{Nonlocal}}}, \qquad \text{where} \quad A_{\text{Nonlocal}} = \Omega_{\|\mathbf{x}-\mathbf{x}_0\|\leq\ell_c} \tag{3.6}$$

As it is common with any other nonlocal theory, the boundary layer (the layer of thickness $2\ell_c$ from the boundaries of the body) will not satisfy the constraint of Eq. (3.5). This inconsistency is resolved by adopting the treatment proposed in the study by Bažant and Pijaudier-Cabot [83]: the integral of Eqs. (3.4) and (3.5) is taken only over the part of the characteristic zone which is located within the body (neglecting the part that lies outside of the body).

The level of nonlocality of $\bar{\varepsilon}_i$ (Eq. (3.4)) depends upon the ratio of the element size to the zone size. In the situations in which the element size is significantly smaller than the zone size Eq. (3.4) will introduce a high level of nonlocality, and $\bar{\varepsilon}_i$ is a weighted-averaged strain over a large number of elements. On the other hand, if the element size happens to be on the order of the zone size, the nonlocal fracture criterion reduces to a local fracture criterion and Eq. (3.4) simplifies to the strain along the edge (ε_i):

$$\bar{\varepsilon}_i = \varepsilon_i = \mathbf{e}_i \cdot \boldsymbol{\varepsilon}^*\, \mathbf{e}_i \geq \varepsilon_{\text{critical}} \tag{3.7}$$

In this chapter in order to determine the nonlocal zone for each element, a circle of radius ℓ_c is built about the circumcenter of each triangular element. The elements whose circumcenter lies within the circle built about element i's circumcenter contribute to the nonlocal zone of the edges of element i. In the extreme case that $\ell_c \to 0$, the circle goes to zero, and the nonlocal fracture criterion reduces to the local criterion of Eq. (3.7).

The edge-based nonlocal fracture criterion has the ability to predict crack propagation and branching. Assume an intact continuum for which the weighted-averaged strain along one edge exceeds the critical strain and crack initiates (Figure 3.1). If the strain in the neighboring edges also exceeds the critical value the crack can propagate into the neighboring edges. The link-based failure is also observed in the transgranular fracture of mild steel at low temperatures as shown in Fig. 1 of the study by Lin, Evans, and Ritchie [21] which shows a ferrite matrix with carbide sediments across the grain boundaries. One can notice from the figure [21] that fracture propagates in a zig-zag manner, and it does not necessarily run across the boundaries of the grain. In fact the figure shows a transgranular fracture crossing the edges of the boundaries bringing an edge-based fracture into mind.

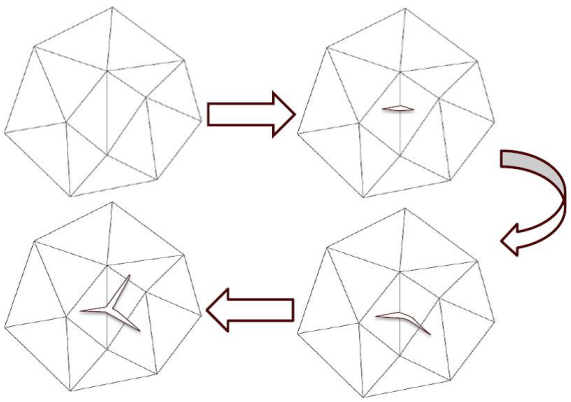

Figure 3.1: Edge-based crack initiation and propagation.

The damage variable is introduced into GraFEA to keep record of the broken edges,. The damage variable, ϕ_i, is imposed on the weighted averaged normal strain along edge i, $\bar{\varepsilon}_i$, if it

exceeds the critical strain value. As already mentioned ϕ_i (acquiring only values of 0 and 1) represents the extent of damage across edge i. A value of $\phi_i = 1$ corresponds to the undamaged case, and $\phi_i = 0$ denotes a failed edge. Note that cracks cross the failed edges, and they are not parallel to those edges. The strain-based fracture criterion chosen in this study is representative of brittle failure.

$$\phi_i = \begin{cases} 1 & \bar{\varepsilon}_i < \varepsilon_{\text{critical}} \\ 0 & \bar{\varepsilon}_i \geq \varepsilon_{\text{critical}} \end{cases} \tag{3.8}$$

3.4 Numerical Results

In this section numerical examples are provided to demonstrate the ability of GraFEA in studying fracture. The examples are aimed to answer the following questions:

1. What is the effect of the incorporation of a length scale parameter in the fracture criterion used in GraFEA?

2. Are the results obtained from GraFEA mesh dependent? Do the results vary noticeably with the changes in the mesh?

3.4.1 The Effect of Length Scale Parameter

The numerical results provided in the recent paper on GraFEA [15] were obtained using a local fracture criterion where the decision on the failure of each edge was made solely on the strain along that particular edge. In this study we consider a nonlocal fracture criterion, where fracture of an edge is dependent upon the collective behavior of all of the edges located within a certain distance (ℓ_c) of the edge of interest. An Examples is provided to examine the effect of considering a nonlocal fracture criterion (including a length scale parameter) on the response.

A rectangular plate of width $W = 4$ units, and length $L = 6$ units with a central circular hole of radius $r = 0.5$ units is considered (Figure 3.2). The plate is assumed to be made of steel with $E = 29 \times 10^6$ and $\nu = 0.3$, and it is considered to be in plane stress condition (with unit thickness). The bottom boundary of the plate is fixed in the vertical direction, and the central node

of the bottom boundary is constrained in the horizontal direction to eliminate rigid body motion. The top boundary of the plate is subjected to increasing tensile displacement boundary condition performing a quasistatic analysis. As discussed in the previous section, the existing bond-breakage models in the literature (such as lattice models or bond-based peridynamic theory) are limited to the Poisson's ratio of 0.25. Whereas GraFEA places no limitations on the material properties.

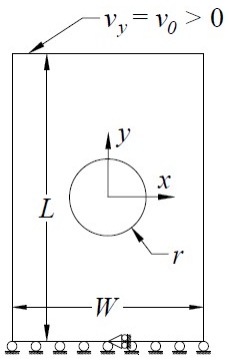

Figure 3.2: Rectangular plate configuration with a circular hole.

The results for 5 values of the length scale parameter are provided to study the effect of non-locality. Figure 3.3 summarizes the results for all cases, $\ell_c/r = 0\%,\ 10\%,\ 20\%,\ 30\%$ and 40%. The same non-uniform mesh is used for all cases (Figure 3.3.a). One can see that by increasing the magnitude of the length scale parameter the width of the diffuse damage band increases. However, as it is demonstrated in Figure 3.4 the changes in the width of the diffuse damage will not be influential on the global force-displacement relation. Figure 3.3.(b-f) illustrate the nodes of the FE mesh in their current configuration (by removing the edges for presentation purposes) for different values of ℓ_c/r. The blue dots correspond to the nodes that remain intact after failure (none of the edges originally attached to these nodes are broken). The yellow dots on the other hand represent the nodes for which less than $2/3$ of the attached edges have failed. Finally, the red dots correspond to the nodes for which over $2/3$ of the edges are broken.

A point is to be made about the quasistatic analysis. If all of the edges connected to a node are broken ($\phi_j = 0$ for all edges j connected to node i), point i will become an isolated point detached

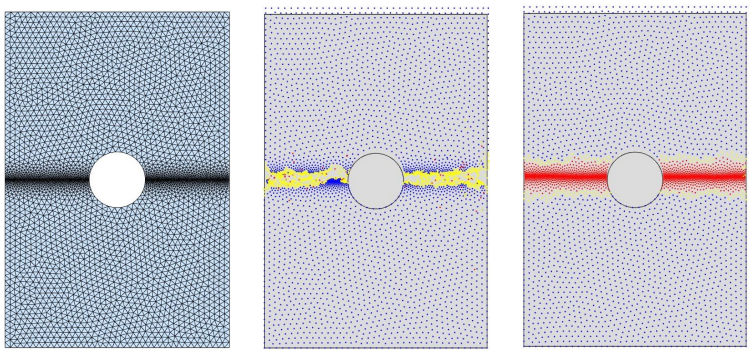

(a) Original Mesh (b) $\ell_c/r = 0\%$ (c) $\ell_c/r = 10\%$

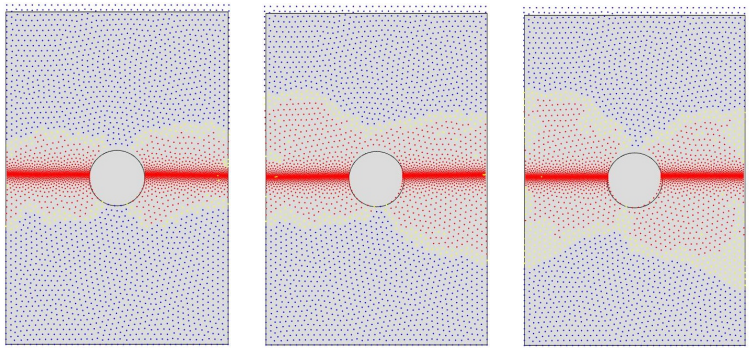

(d) $\ell_c/r = 20\%$ (e) $\ell_c/r = 30\%$ (f) $\ell_c/r = 40\%$

Figure 3.3: The figure demonstrates the effect of the change in the level of nonlocality, ℓ_c on the fracture pattern. The dots represent the nodes in the FE mesh in their current configuration. The blue dots correspond to intact nodes (no broken edges), the yellow dots correspond to the nodes for which less than $2/3$ of the attached edges are broken, and finally the red dots correspond to the nodes for which over $2/3$ of the attached edges are broken.

from the rest of the plate. This will cause a singularity in the global stiffness matrix, unless the stiffness matrix is condensed off the rows and columns corresponding to node i. In this study the ϕ value for the broken edges is set to a very small value (e.g. 0.0001) instead of zero in order to resolve this issue without having to condense the stiffness matrix. A similar approach in a slightly different context was also discussed in a study by Peerlings, de Borst, Brekelmans, and Geers [60]. It is worth mentioning that performing a dynamic analysis would automatically resolve this issue.

The force-displacement diagram of Figure 3.4 highlights the change in the amount of load that can be sustained by the plate with the changes in the length scale parameter (five different values). As ℓ_c increases, the magnitude of the maximum force also increases. This is due to the fact that the averaging is performed over a larger characteristic zone.

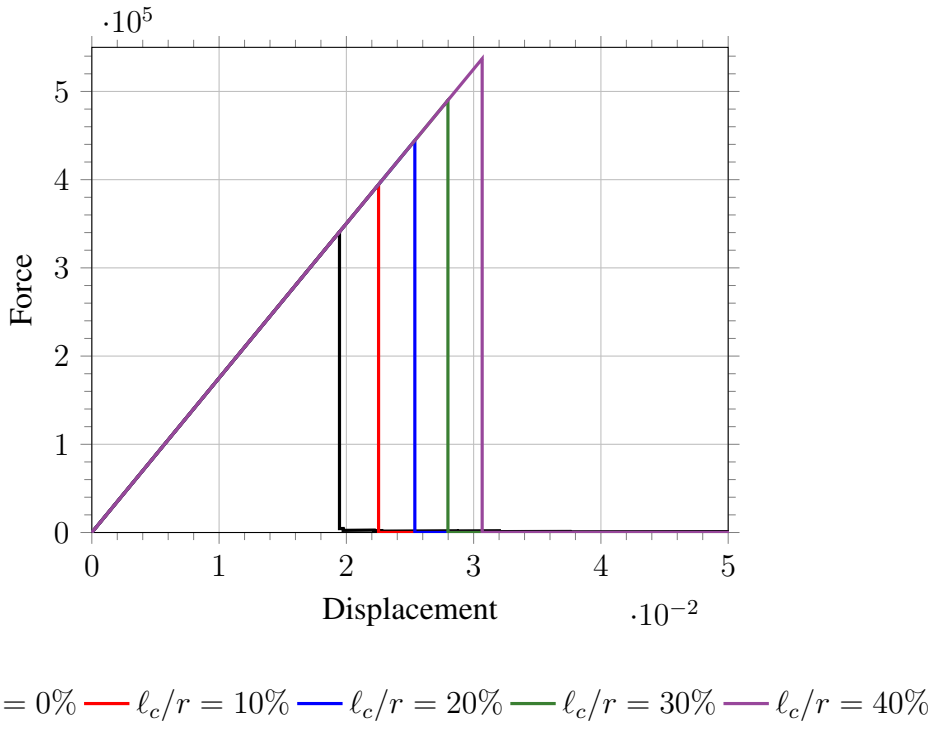

Figure 3.4: Force-displacement results for different values of the length scale parameter.

3.4.2 Mesh Sensitivity Studies

One of the main concerns about any numerical approach is whether or not the results are mesh dependent. The coarseness and fineness of the mesh introduce a length scale into the problem. Therefore, the numerical approaches based on an underlying mesh are in most cases to some extent dependent on the mesh, and a certain degree of fineness of the mesh is required to guarantee the convergence to the solution. The question to be answered in this study is beyond this point, and the aim is to test whether the results from GraFEA are mesh independent providing that the underlying mesh is not very coarse. In order to demonstrate this, two sets of examples are provided:

1. The rectangular plate of the example provided in Subsection 3.4.1 is studied with three meshes of different densities. The force displacement results are compared for the three meshes and the three values of ℓ_c/r to analyze the consistency between them.

2. Mesh sensitivity studies are performed using a hierarchical mesh analysis. In this approach

the analysis starts with a given mesh. Then the mesh is refined through a hierarchical procedure in which each subsequent mesh contains the previous mesh as a subset. This is a methodical approach to studying mesh sensitivity, because one can check whether or not the pattern of a finer mesh is a refined version of the coarser mesh or if the results are completely different.

3.4.2.1 Variation of the mesh density

The example of Subsection 3.4.1 is revisited in this section for three different mesh densities. To be specific the three meshes will have 5716, 6409, and 7654 elements (The results of Subsection 3.4.1 correspond to the mesh of 7654 elements). To examine whether or not the results are mesh dependent, the force-displacement results are compared for the three cases. The shape of the force-displacement diagram for all cases is similar to Figure 3.4, therefore, only the force and displacement at the peak point of the diagram are summarized in Table 3.1. The results are provided for five values of the length scale parameter. The error listed in the last column of the table is the maximum error obtained from the three meshes computed with respect to the average value between the three mesh densities. One can see that the computed error for all cases is very small, and the force-displacement results for all mesh densities are compatible.

Table 3.1: Maximum force and the corresponding displacement of the $F - \delta$ diagram for three mesh densities and five values of the length scale parameter.

	5716 Elements		6409 Elements		7654 Elements		Error(%)	
	F	δ	F	δ	F	δ	F	δ
$\ell_c/r = 0\%$	336163.42	0.01919	339462.27	0.01938	340850.28	0.01946	0.79	0.81
$\ell_c/r = 10\%$	393944.88	0.02248	392033.70	0.02238	394561.51	0.02253	0.38	0.38
$\ell_c/r = 20\%$	439168.27	0.02506	440850.22	0.02517	444406.92	0.02538	0.66	0.69
$\ell_c/r = 30\%$	489976.39	0.02796	491989.07	0.02808	487515.02	0.02784	0.47	0.45
$\ell_c/r = 40\%$	535897.82	0.03059	537005.80	0.03065	537110.94	0.03067	0.17	0.14

Table 3.2 contains the damage pattern for the three mesh densities and five ratios of ℓ_c/r. Each figure demonstrates the nodes of the FE mesh in their deformed configuration which are color-coded as previously described. It can be seen that the diffuse damage pattern of the mesh densities for a specific ℓ_c value differ slightly due to the differences in the mesh. However, according to Table 3.1 these slight variations do not cause discrepancies in a global sense.

Table 3.2: The table contains figures for three different mesh densities and five values of the length scale parameter. Each figure displays the nodes of the FE mesh in current configuration with the color-code described in Figure 3.3.

	$\ell_c/r = 0\%$	$\ell_c/r = 10\%$	$\ell_c/r = 20\%$	$\ell_c/r = 30\%$	$\ell_c/r = 40\%$
5716 Elements	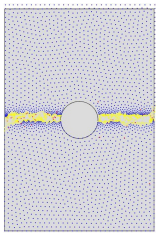	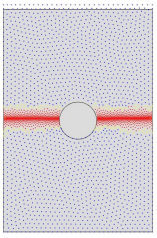	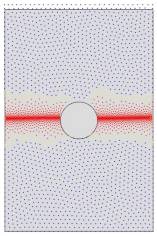	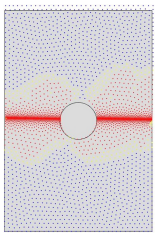	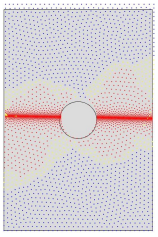
6409 Elements	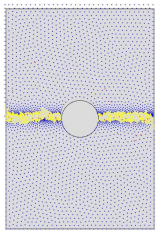	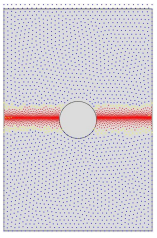	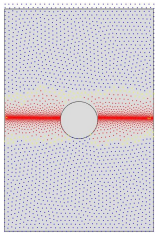	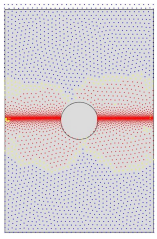	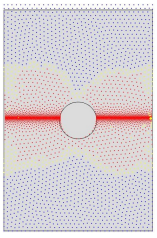
7654 Elements	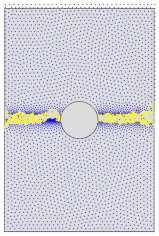	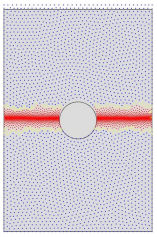	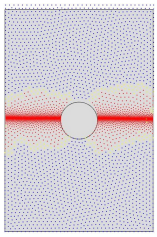	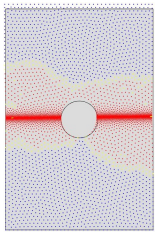	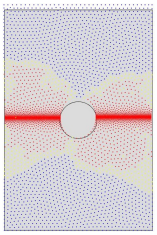

3.4.2.2 Hierarchical mesh

A hierarchical mesh procedure is adopted to study the variation in the results with the changes in the mesh. In each round of mesh refinement each triangular element is divided into four trian-

gular elements by passing lines through the mid-nodes of each two edges of the elements parallel to the third edge. This approach gives four elements which are identical to the original element. Therefore, if the original mesh is a mesh of good quality (avoiding narrow geometries causing singularity), the refined mesh will also preserve the same level of quality. In a hierarchical mesh the refined mesh includes the coarser mesh as a subset. Every round of hierarchical mesh refinement results in an increase in the number of edges, number of nodes, and number of elements (refer to Figure 3.5 and Table 3.3).

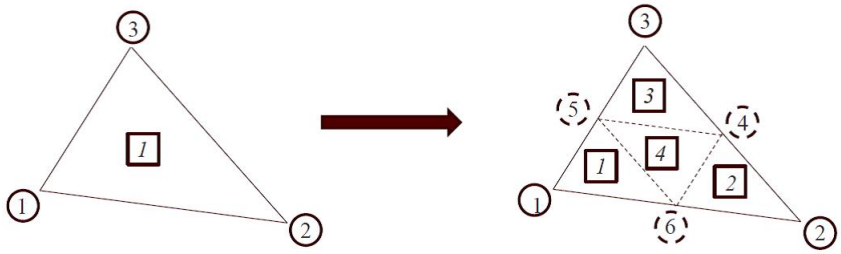

Figure 3.5: Hierarchical mesh refinement on a typical element.

Table 3.3: Increase in the number of edges, nodes, and elements due to one round of hierarchical mesh refinement.

Number of new nodes	Number of edges in the original mesh
Number of new elements	3 $\times$ Number of elements in the original mesh
Number of new edges	Number of edges in the original mesh + 3 $\times$ number of elements in the original mesh

Figure 3.6 shows an example of a hierarchical mesh refinement for a nonuniform mesh. The original mesh goes through two rounds of hierarchical refinements. From the highlighted red element it is apparent that the original mesh is a subset of both the meshes resulting from round one and round two of mesh refinement. The highlighted purple element also shows that the resulting

mesh from the first round of refinement is a subset of the mesh from the second round of refinement.

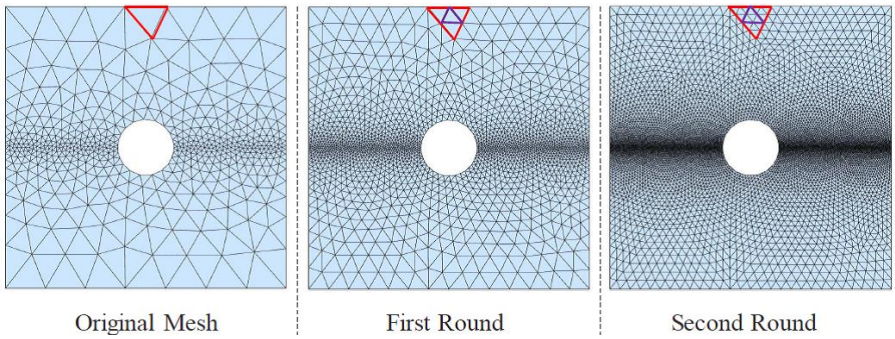

Figure 3.6: The figure shows an example of applying two rounds of hierarchical mesh refinement on a given mesh. The red triangular element in the original mesh is preserved in the first round and second round, and the purple triangular element highlighted in the resulting mesh from the first round is preserved in the second round.

An example of mesh sensitivity studies utilizing a hierarchical mesh refinement is provided next to assess whether the results of GraFEA are dependent on the fineness of the underlying mesh. A square plate ($W = L = 2$) with a circular hole ($r = 0.25$) is chosen (Figure 3.7). The plate is made of steel with $E = 29 \times 10^6$ and $\nu = 0.3$ in plane stress condition. A local fracture criterion is used first, and then a length scale parameter is introduced to investigate the effect of nonlocality. Similar to the previous examples the top boundary is subjected to tensile displacement boundary conditions, and the bottom boundary is constrained in the vertical direction. The central node at the bottom boundary is constrained in the horizontal direction to restrict rigid body translation. Three rounds of mesh refinement are performed. The number of nodes and elements in the original mesh and the subsequent meshes are tabulated in Table 3.4.

The results are provided for two values of the length scale parameter, to be specific $\ell_c/r = 0\%$ and 10%. The force-displacement diagram for all four cases (including the original mesh) is provided in Figure 3.8. Figure 3.9 provides the fracture pattern for each case by utilizing the color-code of Figure 3.3. According to Figure 3.8, using the local fracture criterion the force displace-

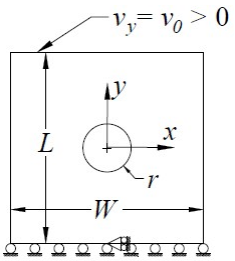

Figure 3.7: Square plate with a circular hole.

Table 3.4: Mesh information for the original mesh, and the resulting meshes after one, two, and three rounds of hierarchical mesh refinement.

	Original Mesh	First Round	Second Round	Third Round
Number of nodes	415	1580	6160	24320
Number of elements	750	3000	12000	48000
Number of edges	1165	4580	18160	72320

ment diagrams for the meshes resulting from the first and second rounds of mesh refinement are within very good agreement. However, the force corresponding to the peak value of the third round (using a local fracture criterion) is slightly smaller than that of round one and round two. This can be attributed to the mesh dependency of the results of GraFEA with a local fracture criterion. One can also notice from Figure 3.9 that there is a good compatibility between the fracture pattern of the round one and round two mesh refinements, however, the crack pattern is different for round three of mesh refinement. It is also apparent that the maximum force and the corresponding displacement for the original mesh are larger compared to the other meshes. This is partly due to the mesh dependency of the results and partly due to the coarseness of the original mesh. The force-displacement results for a nonlocal fracture criterion (Figure 3.9) show perfect compatibility for all of the meshes (except for the post-fracture-initiation deviation noticed for the original mesh which is due to the coarseness of the original mesh). It is obvious that the introduction of the integral-type nonlocal fracture criterion will help eliminate the observed mesh dependency for the

original GraFEA formulation [15].

The deformed configurations for the original mesh and the three rounds of mesh refinement are provided in Figure 3.9 for the two values of the length scale parameter. The deviation of the crack path for round three mesh refinement of a local fracture criterion from those of round one and round two is noticeable from the figures. The introduction of the nonlocality in the fracture criterion results in an obvious diffuse damage. However, according to Figure 3.8 this variation in the diffuse damage pattern does not cause changes in the global force-displacement response, and the global mesh independency is preserved through the introduction of a nonlocal fracture criterion.

A few remarks must be made at this point on the integration of a nonlocal fracture criterion in GraFEA:

- According to Jirásek [64], the nonlocal approach is only successful (in resolving the mesh dependency induced by strain localization) when it is applied to a proper variable. The results obtained in this study demonstrate that applying the nonlocality to the edge-based damage variable enables GraFEA of producing mesh independent results.

- Peerlings et al. [60] suggested that in the strong nonlocal theories the integral averaging at each point should only take place over the portion of the characteristic zone which has not yet failed. Otherwise, the large strains that are formed in the broken edges will cause a faster growth of the crack and an increase in the width of the diffuse damage part. The effect of updating the characteristic zone with the progression of crack needs to be further studied.

- One of the issues with integral-type nonlocal damage theories is the question that whether or not the points located on the two sides of a crack (yet still in each other's characteristic zone) will interact. This issue has also been expressed in the study by Peerlings et al. [60], however, its effect is yet to be studied.

3.5 Chapter Summary and Conclusions

This chapter is an extension of the recent paper on GraFEA [15] for the study of fracture in solids. The goals of this chapter are two-folded: the influence of the nonlocality of the fracture criterion used in GraFEA is studied on the results, and the mesh-sensitivity of GraFEA is examined for both local and nonlocal fracture criteria. The numerical results illustrate that GraFEA is mesh dependent in its original form (local fracture criterion), and the introduction of the nonlocality in the fracture pattern will help eliminate the mesh dependency caused by fracture localization. The second major finding of this study is that by increasing the level of nonlocality (the length scale parameter), the problem shifts from an acute fracture problem to a fracture problem with a diffuse damage pattern.

These findings enhance our understanding of GraFEA, however, more research is required to investigate the mesh dependency of the results in a more systematic way. The existing studies in the literature have only dealt with mesh sensitivity in a general sense by qualitatively comparing the crack patterns, or comparing the global behavior of the model (global force-displacement relationship, wave propagation properties, changes in the dissipated energy with mesh refinement). Although these studies are informative, they do not provide us with a quantitative measure for studying mesh dependency.

Further studies need to be carried out to determine the compatibility of the results from GraFEA with experimental results. This study was a parametric study on the effect of including an intrinsic length scale on the numerical results. It is hoped that this study will provide an impetus for experimentation to determine what this length scale corresponds to. By observing Figure 3.3 and Figure 3.9, one might speculate that the length scale might probably be related to the width of the band of the diffuse damage. According to a study by Bažant and Jirásek [35]:

> "In relation to nonlinear fracture mechanics, the characteristic length in quasibrittle materials with distributed cracking may be physically interpreted as (or related to) the effective size of the fracture process zone at the tip of a macroscopic crack."

However, more research and experiments are needed to determine the physics behind the length scale parameter, and how it can be determined for particular material.

It would also be of interest to incorporate GraFEA into probabilistic methods to provide a contour of damage probability as opposed to deterministic approaches with a definite crack path. Due to the level of uncertainty involved (geometry, material properties, manufacturing flaws, etc.), a probabilistic approach would provide us with more reliable results in the study of damage and fracture. As Bažant and Jirásek [35] put it in words:

> "... the real crack path is tortuous and, in one single experiment, may deviate from the ideal trajectory. However, the computational simulations is supposed to reproduce the mean trajectory, averaged over a large number of experiments."

It is already known that if the same experiment is run for different samples of the same material (with similar geometry, and loading conditions), the fracture pattern will differ in the samples. Thus, the main goal of the computational methods should not be to determine the exact crack path of an experiment, but to determine a zone in which damage is most probable.

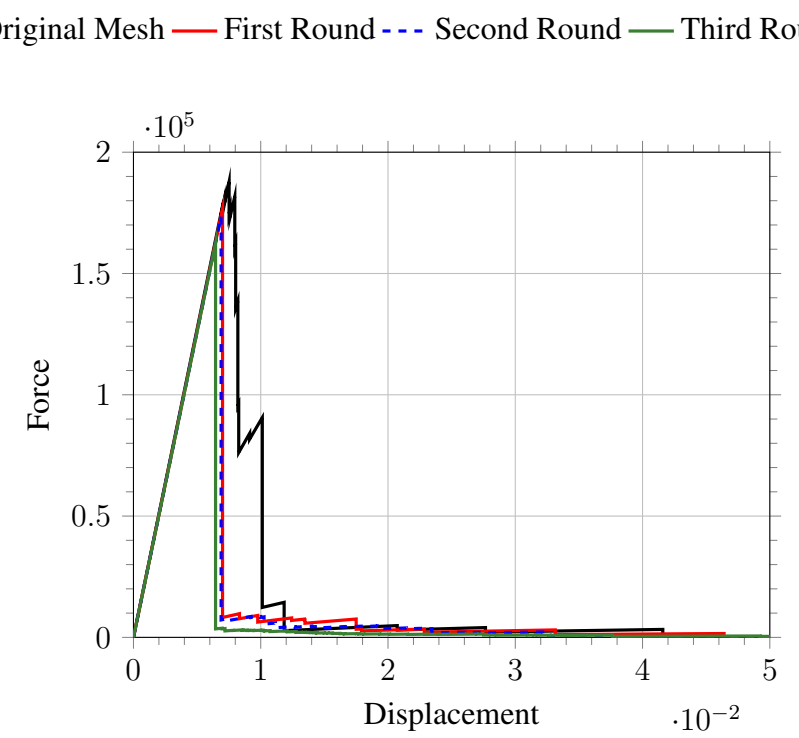

(a) Local Fracture Criterion, $\ell_c/r = 0\%$

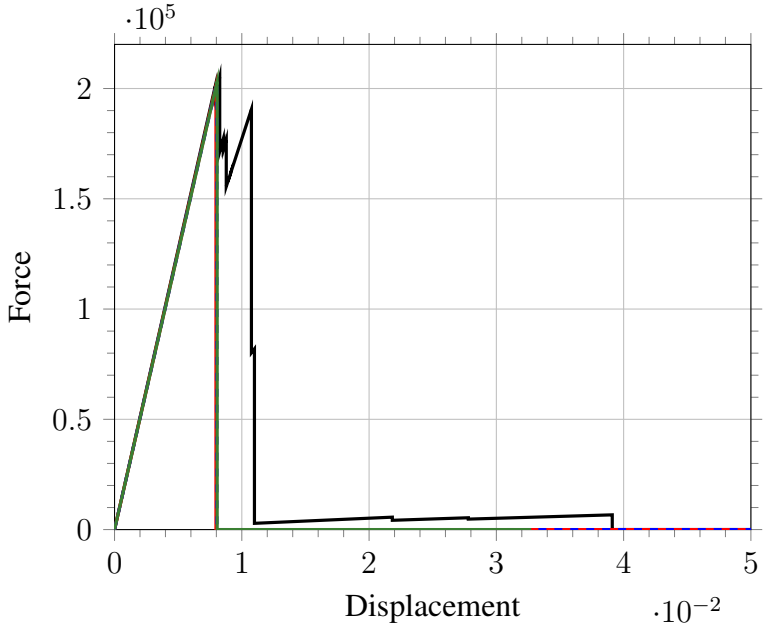

(b) Nonlocal Fracture Criterion, $\ell_c/r = 10\%$

Figure 3.8: Force-displacement results for a square plate with a circular hole subjected to a tensile displacement boundary condition. The results are provided for a given mesh and three rounds of hierarchical mesh refinement using a local fracture criterion $(\ell_c/r = 0\%)$ and a nonlocal fracture criterion $(\ell_c/r = 10\%)$.

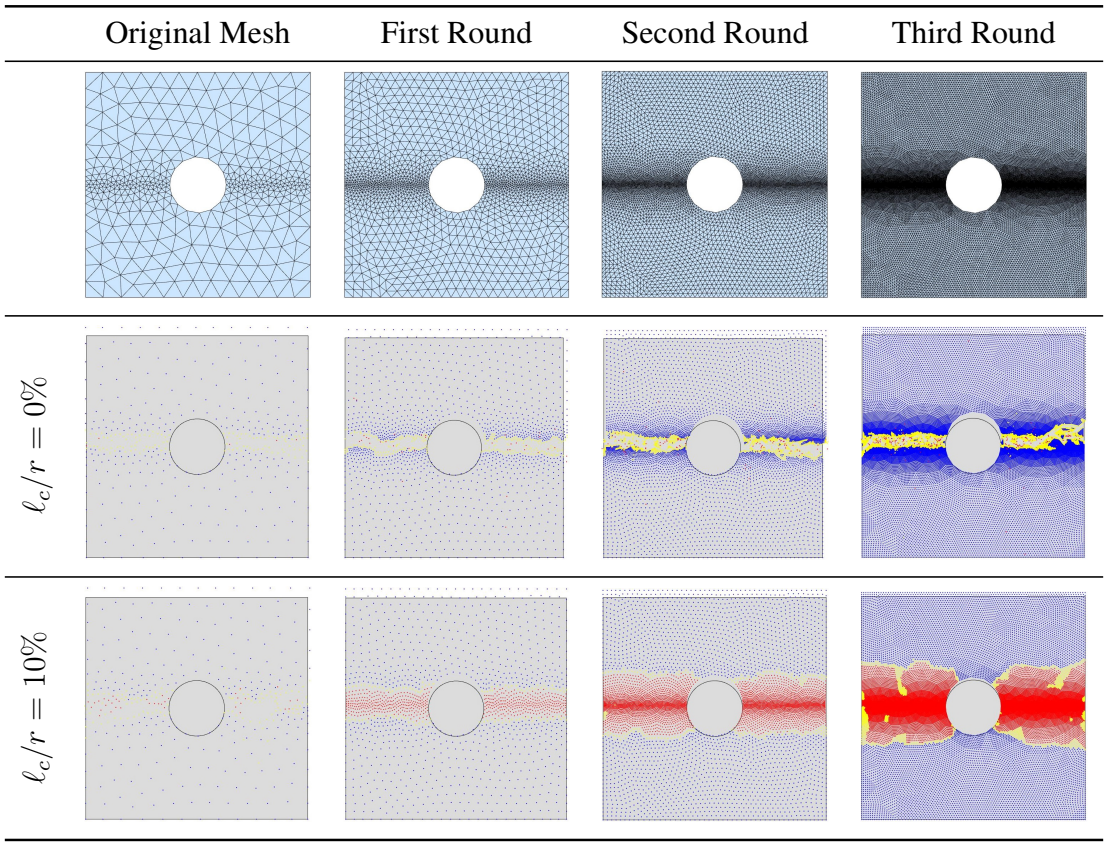

Figure 3.9: The figure contains the original mesh and the results of the three subsequent rounds of mesh refinement, as well as the deformed configurations for a local fracture criterion ($\ell_c/r = 0\%$) and a nonlocal fracture criterion ($\ell_c/r = 10\%$). The second row displays the FE mesh in the reference configuration, while the third and fourth rows contain the nodes of the FE mesh in current configuration with the color-code described in Figure 3.3.

4. A UNIFIED INTEGRO–DIFFERENTIAL NONLOCAL MODEL*

4.1 Introduction

For hyperelastic materials (i.e., Green elastic materials) there exists a potential function whose derivative with respect to the strain at a point gives the corresponding stress at that point [84]. This forms the basis for a local (conventional) constitutive model where the stress and strain at each point are related. Local theory of continuum mechanics is inherently scale free, i.e. forces are only transferred through contact and no long–range forces between points located further apart are considered. However, there exists certain phenomena (e.g., dispersion of elastic waves, crack propagation in fracture mechanics, dislocations, and so on) that cannot be explained using local theory of elasticity. In addition, as a consequence of recent developments in the field of material science there is a need to model the structural response of a variety of new materials that require the consideration of nonlocal aspects of the material (e.g. size effect in nanomaterials). In nonlocal theories, stress at each point is influenced by the strain at all points in the domain. This influence decreases as the distance between the points increases. The concept of nonlocal theory of linear elasticity was initially introduced in papers by Kröner [85], Krumhansl [86], and Kunin [87]. Later, the idea of long–range interactions was further developed in the works of Eringen [88–91] and Eringen and Edelen [92]. Eringen [90] introduced an integro–differential nonlocal model which has widely been used in the literature. Later, Eringen proposed a two–phase nonlocal model [22] which was a combination of local and integro–differential nonlocal constitutive theories. One of the advantages of an integral nonlocal theory over the local elasticity theory is that the former gives non–singular results for geometric singularities (i.e. cracks) due to the averaging effect inherent in the integral form of the constitutive relation.

The nonlocal integral constitutive equation makes use of a positive distance–decaying kernel function which specifies the dependence of stress at each point on the strain at other points in

*Reprinted with permission from "A unified integro–differential nonlocal model" by P. Khodabakhshi, and J. N. Reddy, 2015. *International Journal of Engineering Science*, 95, 60–75, Copyright 2015 by Elsevier Ltd.

the domain. Eringen [90] showed that for a specific class of kernel functions the Eringen nonlocal integral constitutive equation can be transformed into a differential form with the exact same properties. Due to the difficulties in using integral constitutive equations, the nonlocal differential model proposed by Eringen [90] is the one most widely used in the literature to account for nonlocal effects. Several studies have been reported on the basis of nonlocal theories. Peddieson, Buchanan,and McNitt [93] used the Eringen nonlocal differential model to derive the equations of equilibrium for a nonlocal Euler–Bernoulli beam. This study [93] was pioneering in the sense that Eringen nonlocal differential model was used to incorporate nonlocal effects into the analysis of structural elements. One of the main issues that was discussed in the work of Peddieson, Buchanan,and McNitt [93] was the fact that in nonlocal cantilever beams (enhanced with Eringen's differential model) nonlocal effects were not triggered for point loads applied at the free end. This is not a desirable outcome, because recently cantilever beams of micro–and nano–sizes have found several applications as actuators and sensors in the fields of chemical and biological sciences [94–97]. If a nonlocal model is not capable of capturing the size effect in these nano–and macro–cantilever beams, then the data obtained by these devices may not be interpreted correctly.

Other examples of nonlocal Euler–Bernoulli beam studies were presented in [65, 98–100]. Challamel and Wang [65] also pointed to the deficiency mentioned in [93] and suggested the integration of gradient elasticity model with Eringen nonlocal model to eliminate it. Shakouri, Lin, and Ng [100] gave a discrete formulation for a nonlocal Euler–Bernoulli beam representation of the double–walled carbon nanotubes using the Galerkin method. Wang, et al. [101], Wang et al. [102], Wang, and Wang [103], and Wang, and Liew [104] integrated Timoshenko beam theory with Eringen nonlocal model. The main problem with these works [101–104] is that nonlocal effects are only limited to normal stresses and not transverse shear stresses. Reddy [105] used Eringen nonlocal model to give the variational statements for several beam theories, namely the Euler–Bernoulli, Timoshenko, Reddy and Levinson beam theories. In this comprehensive study [105] the limitation on considering the nonlocal effects on the shearing stresses [101–104] is removed and nonlocal effects are included in both normal and transverse shear stresses. Analytical solutions of static bend-

ing, vibration, and buckling of the beams are also provided in this study [105]. Later, Reddy [106] formulated the governing equations for the bending of Eringen nonlocal beams (Euler–Bernoulli and Timoshenko beam theories) and plates (Classical and first order shear deformation plate theories) which also took in account von Kármán nonlinearity. Reddy [106] stated that no quadratic functional can be derived for the differential form of Eringen nonlocal beam theory from which the governing equations can be derived. Thai [107], and Thai, and Vo [108] recently provided a higher order nonlocal beam theory slightly different from Reddy beam theory which also accounted for variation of shear stress along the height of the beam. Reddy and El–Borgi [109] provided the governing equations for bending of nonlocal Euler–Bernoulli and Timoshenko beam theories accounting for moderate rotations through modified von Kármán nonlinearity. Several studies have also applied Eringen nonlocal model to the study of functionally graded beams [110–112]. Studies on nonlocal beam theories based on the differential model are far more exhaustive to be reported here. Interested readers may consult [109] and [110] for further information.

In all of the above–mentioned references, the differential form of the Eringen model had been used. Polizzotto [113] applied the integral form of Eringen model and derived the variational principles governing the integral form from which the nonlocal finite element formulation is obtained. The kernel function in the integral constitutive equation brings in a concept of a length scale. Pisano and Fuschi [114] used the approach proposed by Polizzotto [113] to derive a closed–form solution for a bar in tension with Eringen nonlocal model as the constitutive equation. Later, Pisano, Sofi, and Fuschi [115] used this integro–differential nonlocal model to give a finite element formulation for 2D problems of two–phase elastic materials [22]. DiPaola et al. [116] came up with a new method to introduce long–range forces into the equations of motion. General 3D variational statements were constructed and they were further simplified for the Timoshenko beam theory. The formulation proposed by DiPaola et al. [116] is conceptually similar to the formulation of peridynamic theory proposed by Silling [13].

It is found by several researchers that Eringen's differential model yields inconsistent results for a cantilever when compared to other boundary conditions [65, 93, 102, 104, 117]. For all bound-

ary conditions except the cantilever, the model predicts softening effect (i.e., larger defections and lower fundamental frequencies) as the nonlocal parameter is increased. Several ad hoc approaches or explanations have been proposed to alleviate the baffling case of the cantilever beam. In the present study, classical theory of elasticity is augmented with Eringen's nonlocal model in integral form to present a unified integro–differential model for nonlocal elasticity and a general finite element formulation for the integral form of Eringen nonlocal model. Note that by using the two–phase Eringen model [22], two control parameters will exist, namely the length scale parameter and phase parameter. The general 3D equations are further simplified to the one–dimensional case of the Euler–Bernoulli beam theory. Several examples are provided to show how Eringen nonlocal model affects the transverse displacement of the beams. In this study, the kernel function used in the integral constitutive equation is different from that of which yields into Eringen's differential equation [90]. It is shown that the proposed nonlocal model yields consistent results for most boundary conditions (including the paradoxical case of a cantilever beam), however, the results are slightly different for the case of a simply supported beam. Among the provided examples, other than the simply supported beam which shows a slight stiffening effect, the rest of the boundary conditions show a softening effect as expected. This result is promising, in the sense that it can be used for the study of nonlocal effects in micro–and nano–cantilevers used as actuators/sensors in biological and chemical sciences. The softening effect increases with the increase in the length scale parameter and the decrease in the phase parameter. A brief discussion on the applicability of the integral formulation to general problems is brought in the end. Also the transition from stiffened nonlocal simply supported beam to softened nonlocal clamped beam is studied further.

4.2 Eringen–type Nonlocal Formulation

4.2.1 Unified Nonlocal Constitutive Model

The Eringen nonlocal model [88, 89] is based on the assumption that the stress at each point depends on the strain at all points of the domain. According to this model, stress at point $\mathbf{x}$ can be

determined according to the following equation:

$$\boldsymbol{\sigma}(\mathbf{x}) = \int_{V'} \alpha(\mathbf{x}, \mathbf{x}', l_c)\, \mathbf{C} : \boldsymbol{\varepsilon}(\mathbf{x}')\, dV' \tag{4.1}$$

where $\boldsymbol{\varepsilon}(\mathbf{x}')$ is the local strain at point $\mathbf{x}'$ which is assumed to be the linearized version of the Green–Lagrange strain tensor [84]:

$$\boldsymbol{\varepsilon}(\mathbf{x}) = \frac{1}{2}\left[\nabla \mathbf{u} + (\nabla \mathbf{u})^T\right] \tag{4.2}$$

In Eq. (4.1), $\alpha(\mathbf{x}, \mathbf{x}', l_c)$ is a kernel function which determines the measure by which stress at point $\mathbf{x}$ is affected by the strain at point $\mathbf{x}'$; $\alpha(\mathbf{x}, \mathbf{x}', l_c)$ has the following properties [90]:

1. It should be a positive distance decaying function with its maximum value taking place at $\mathbf{x} = \mathbf{x}'$.

2. In the limit of $l_c \to 0$ (where l_c is a length scale parameter), the kernel function should revert to the Dirac–delta function and the nonlocal formulation should simplify to the familiar local formulation.

3. In the limit of $l_c \to \infty$, the Eringen model should approximate lattice theory.

4. The integral of this function over the whole domain should be unity (assuming that point $\mathbf{x}$ is embedded in an infinite domain):

$$\int_{V'} \alpha(\mathbf{x}, \mathbf{x}', l_c)\, dV' = 1 \tag{4.3}$$

Selection of the kernel function is based on satisfying the above–mentioned physical and mathematical requirements. Note that the kernel function introduces a concept of material length scale into the problem. The distance of each point within the domain from a specific point $\mathbf{x}$ becomes meaningful only when it is compared to a length scale. A kernel function is often chosen to be symmetric and one of the most commonly used forms is the exponential function of the following

form:

$$\alpha\left(\frac{|\mathbf{x}-\mathbf{x}'|}{l_c}\right)=\alpha_0 e^{-\frac{|\mathbf{x}-\mathbf{x}'|}{l_c}} \tag{4.4}$$

where α_0 is determined by satisfying the constraint in Eq. (4.3) while assuming that the point is embedded in an infinite domain.

Equation (4.1) can be modified such that it takes the form of a two–phase constitutive model with both local and nonlocal phases [22]:

$$\boldsymbol{\sigma}(\mathbf{x})=\xi_1\mathbf{C}:\boldsymbol{\varepsilon}(\mathbf{x})+\int_{V'}\xi_2\alpha(\mathbf{x},\mathbf{x}',l_c)\,\mathbf{C}:\boldsymbol{\varepsilon}(\mathbf{x}')\,dV' \tag{4.5}$$

where ξ_1 and ξ_2 satisfy the following relation:

$$\xi_1+\xi_2=1 \tag{4.6}$$

Here ξ_1 and ξ_2 represent measures of local and nonlocal properties of the model; $\xi_1=1$ and $\xi_2=0$ corresponds to the purely local constitutive equation and $\xi_1=0$ and $\xi_2=1$ corresponds to the original Eringen nonlocal constitutive equation. ξ_1 is called phase parameter in the following sections.

It is worth mentioning that nonlocal theories in general will introduce at least one length scale parameter into the constitutive equation (i.e. l_c in Eq. (4.1)) regardless of the choice of differential or integral form. The two–phase constitutive equation used in this study (Eq. (4.5)) accounts for an additional independent variable, i.e. the phase parameter, compared to the differential form of Eringen nonlocal model. The phase parameter, ξ_1, adds to the generality of the formulation used herein. By setting $\xi_1=0$ the original Eringen formulation is attained.

In order for the nonlocal continuum theory to be applicable to the study of problems with prominent nonlocal effects, the length scale parameter, l_c, should be determined to be representative of the problem at hand. Notice that in the original formulation of Eringen [90] and the papers using the differential form of Eringen model, the kernel function is defined to be $\alpha=\alpha(|\mathbf{x}-\mathbf{x}'|,\tau)$, where $\tau=e_0a/l$. In this formulation a and l are internal and external

characteristic lengths, respectively, and e_0 is a constant which is material dependent. The corresponding counterpart in the formulation used herein is $\tau l = e_0 a = l_c$. To this date, no consensus has been reached on how to experimentally determine the material–dependent length scale parameter. Eringen [90] proposed that the length scale parameter be determined such that the dispersion curve of the nonlocal theory agreed with that of the atomistic approaches. Wang and Wang [103] suggested a conservative range for the length scale parameter of the single–walled CNTs to be $l_c < 2.0$ nm. According to Arash and Wang [118], the length scale parameter of CNTs depends on several parameters, i.e. boundary conditions, chirality, number of walls, and so on. Further studies are required to determine the length scale parameter corresponding to a specific problem.

4.2.2 General Finite Element Formulation

The equations of equilibrium and the boundary conditions will remain the same as in local analysis, where $\boldsymbol{\sigma}$ is replaced by the definition in Eq. (4.5):

$$\nabla.\boldsymbol{\sigma} + \mathbf{b} = \mathbf{0} \quad \text{in } V, \quad \mathbf{u} = \bar{\mathbf{u}} \quad \text{on } \Gamma_u, \quad \mathbf{t} = \bar{\mathbf{t}} \quad \text{on } \Gamma_t \tag{4.7}$$

where V is the interior domain of the body, Γ_u is the part of the boundary where displacements are specified, and Γ_t is the part of the boundary where traction is specified; Γ_u and Γ_t are disjoint parts with the property $\Gamma_u \cup \Gamma_t = \Gamma$, with Γ being the entire boundary of the domain.

The total potential energy of the system can be written as [119]:

$$\begin{aligned}
\Pi(\mathbf{u}) = U + V^E &= \int_V \left(\frac{1}{2}\boldsymbol{\sigma} : \boldsymbol{\varepsilon} - \mathbf{b}.\mathbf{u} \right) dV - \oint_\Gamma \mathbf{t}.\mathbf{u}\, dS \\
&= \int_V \left(\frac{1}{2}\xi_1 \boldsymbol{\varepsilon}(\mathbf{x}) : \mathbf{C} : \boldsymbol{\varepsilon}(\mathbf{x}) - \mathbf{b}.\mathbf{u} \right) dV \\
&\quad + \frac{1}{2}\int_V \left(\int_{V'} \xi_2 \alpha(\mathbf{x}, \mathbf{x}', l_c)\, \boldsymbol{\varepsilon}(\mathbf{x}) : \mathbf{C} : \boldsymbol{\varepsilon}(\mathbf{x}')\, dV' \right) dV - \oint_\Gamma \mathbf{t}.\mathbf{u}\, dS
\end{aligned} \tag{4.8}$$

The finite element model is derived using the procedure discussed in [51]. The weak form associated with Eq. (4.8) is

$$0 = \int_{V_e} \left\{ -\left(\nabla \mathbf{w}\right)^T : \left[\xi_1 \mathbf{C} : \boldsymbol{\varepsilon}_e\left(\mathbf{x}\right) + \sum_{e'=1}^{N_{el}} \int_{V_{e'}} \xi_2 \alpha\left(\mathbf{x}, \mathbf{x}', l_c\right) \mathbf{C} : \boldsymbol{\varepsilon}_{e'}\left(\mathbf{x}'\right) dV' \right] \right\} dV \tag{4.9}$$
$$+ \int_{V_e} \mathbf{w}^T . \mathbf{b}_e dV + \oint_{\Gamma_e} \mathbf{w}^T . \mathbf{t}_e \, dS$$

where N_{el} is the number of elements in the domain and $\mathbf{t}_e$ is the traction vector along the boundaries of element e. The nonlocal terms correspond to element e' interacting nonlocally with element e.

Next, the displacement field $\mathbf{u}\left(\mathbf{x}\right)$ is replaced with a finite element approximation and the strains are computed using Eq. (4.2):

$$\mathbf{u}\left(\mathbf{x}\right) = \boldsymbol{\Psi}_e \boldsymbol{\Delta}_e \quad \mathbf{x} \in V_e, \; e = 1, ..., N_{el} \tag{4.10}$$

$$\boldsymbol{\varepsilon}\left(\mathbf{x}\right) = \left\langle \varepsilon_{xx} \quad \varepsilon_{yy} \quad \varepsilon_{zz} \quad \gamma_{yz} \quad \gamma_{xz} \quad \gamma_{xy} \right\rangle^T = \mathbf{D}\mathbf{u}\left(\mathbf{x}\right) = \mathbf{B}_e \boldsymbol{\Delta}_e \tag{4.11}$$

In Eqs. (4.10) and (4.11), $\boldsymbol{\Delta}_e$ is the vector of nodal displacements of element e, and $\boldsymbol{\Psi}_e$ is the matrix of shape functions relating the displacement field of the element to its nodal displacements $\boldsymbol{\Delta}_e$. For a general three–dimensional problem $\boldsymbol{\Delta}_e$, and $\boldsymbol{\Psi}_e$ are defined according to Eqs. (4.12) and (4.13) with n being the number of nodes in the element.

$$\boldsymbol{\Delta}_e = \left\langle u_x^1 \quad u_y^1 \quad u_z^1 \quad ... \quad u_x^n \quad u_y^n \quad u_z^n \right\rangle^T_{3n \times 1} \tag{4.12}$$

$$\boldsymbol{\Psi}_e = \begin{bmatrix} \psi_1 & 0 & 0 & ... & \psi_n & 0 & 0 \\ 0 & \psi_1 & 0 & ... & 0 & \psi_n & 0 \\ 0 & 0 & \psi_1 & ... & 0 & 0 & \psi_n \end{bmatrix}_{3 \times 3n} \tag{4.13}$$

In Eq. (4.11), $\mathbf{B}_e$ is defined as

$$\mathbf{B}_e = \mathbf{D}\boldsymbol{\Psi}_e \tag{4.14}$$

and $\mathbf{D}$ is a differential matrix operator:

$$\mathbf{D} = \begin{bmatrix} \frac{\partial}{\partial x} & 0 & 0 \\ 0 & \frac{\partial}{\partial y} & 0 \\ 0 & 0 & \frac{\partial}{\partial z} \\ 0 & \frac{\partial}{\partial z} & \frac{\partial}{\partial y} \\ \frac{\partial}{\partial z} & 0 & \frac{\partial}{\partial x} \\ \frac{\partial}{\partial y} & \frac{\partial}{\partial x} & 0 \end{bmatrix} \tag{4.15}$$

The weight function $\mathbf{w}$ is replaced with the shape functions $\mathbf{\Psi}_e$. Therefore, we have

$$\nabla \mathbf{w} = \mathbf{B}_e = \mathbf{D}\mathbf{\Psi}_e \tag{4.16}$$

Finally, $\mathbf{u}$ and $\mathbf{w}$ are substituted into Eq. (4.9) to obtain the final finite element model over an element e

$$\begin{aligned} 0 = \int_{V_e} \left\{ -\mathbf{B}_e^T : \left[\xi_1 \mathbf{C} : \mathbf{B}_e \mathbf{\Delta}_e + \sum_{e'=1}^{N_{el}} \int_{V_{e'}} \xi_2 \alpha \left(\mathbf{x}, \mathbf{x}', l_c \right) \mathbf{C} : \mathbf{B}_{e'} \mathbf{\Delta}_{e'} dV' \right] + \mathbf{\Psi}_e^T \mathbf{b}_e \right\} dV \\ + \oint_{\Gamma_e} \mathbf{\Psi}_e^T \mathbf{t}_e \, dS \end{aligned} \tag{4.17}$$

or

$$\xi_1 \mathbf{k}_e^l \mathbf{\Delta}_e + \xi_2 \sum_{e'=1}^{N_{el}} \mathbf{k}_{ee'}^{nl} \mathbf{\Delta}_{e'} = \mathbf{F}_e \tag{4.18}$$

where

$$\mathbf{k}_e^l = \int_{V_e} \mathbf{B}_e^T : \mathbf{C} : \mathbf{B}_e \, dV \qquad \mathbf{x} \in V_e \tag{4.19}$$

$$\mathbf{k}_{ee'}^{nl} = \int_{V_e} \int_{V_{e'}} \alpha \left(\mathbf{x}, \mathbf{x}', l_c \right) \mathbf{B}_e^T : \mathbf{C} : \mathbf{B}_{e'} dV' \, dV \qquad \mathbf{x} \in V_e, \, \mathbf{x}' \in V_e' \tag{4.20}$$

$$\mathbf{F}_e = \int_{V_e} \mathbf{\Psi}_e^T \mathbf{b}^e \, dV + \oint_{\Gamma_e} \mathbf{\Psi}_e^T \mathbf{t}^e \, dS \tag{4.21}$$

where $\mathbf{k}_e^l$ and $\mathbf{k}_{ee'}^{nl}$ are the local and nonlocal parts of the stiffness matrix, respectively; $\mathbf{F}_e$ is the element force vector. Note that $\mathbf{k}_{ee'}^{nl}$ has double integration over the domain of elements e and e'. By

setting $\xi_1 = 1$ in Eq. (4.18), we obtain the familiar finite element model for the local theory. Also it is worth mentioning that according to Eq. (4.21) the natural boundary conditions for nonlocal formulation remain the same as those of local formulation. Equation (4.18) is assembled for all elements in the domain and the specified boundary conditions are imposed before solving for the unknown nodal values of the displacements.

4.2.3 Kernel Function for One–dimensional Analysis

This study is dedicated to the beams with nonlocal constitutive equations. Therefore, one needs to determine the one dimensional kernel function used in Eringen nonlocal model. It is assumed that nonlocal effects are only present along the length of the beam and no effect is considered in the other two dimensions. For 1D problems Eq. (4.4) simplifies to an exponential equation of the following form:

$$\alpha\left(\frac{|x-x'|}{l_c}\right) = \alpha_0 e^{-\frac{|x-x'|}{l_c}} \tag{4.22}$$

The constraint in Eq. (4.3) is used to determine the constant α_0 in Eq. (4.22). For simplicity of integration, it is assumed that the cross section of the beam is constant and doesn't change across the length of the beam, therefore, $A' = A$:

$$\int_{-\infty}^{+\infty}\int_{A}\alpha\left(\frac{|x-x'|}{l_c}\right)dAdx' = 2\alpha_0 A l_c = 1 \rightarrow \alpha_0 = \frac{1}{2Al_c} \tag{4.23}$$

Hence the kernel function becomes

$$\alpha\left(\frac{|x-x'|}{l_c}\right) = \frac{1}{2Al_c}e^{-\frac{|x-x'|}{l_c}} \tag{4.24}$$

However, note that the nonlocal part of the stiffness matrix (Eq. (4.20)) has a volume integral over the domain of element e'. Knowing that no nonlocal effect is considered along the height and width of the beam, A can be factored out of the integration. Finally, one can assume the kernel function to be:

$$\alpha\left(\frac{|x-x'|}{l_c}\right) = \frac{1}{2l_c}e^{-\frac{|x-x'|}{l_c}} \tag{4.25}$$

where the volume integration over element e' is transformed to an integration over the length of this element only.

In the original formulation, each point is assumed to interact nonlocally with all other points in the domain. Since the kernel function, α, decays rapidly with distance, it acquires a very small value beyond some point. One can make use of this property to limit the domain of nonlocal interactions which is named to be the influence zone. An influence zone of the radius $l_i = 6l_c$ is a reasonable choice which is used in this study. Using this value the exponential term of the kernel function reduces to $e^{-l_i/l_c} \approx 0.0025$ which is practically a very small value.

4.2.4 Finite Element Model of the Nonlocal Euler–Bernoulli Beam Theory

The ideas presented in the previous sections are applied to the bending of beams. We consider the Euler–Bernoulli beam theory to illustrate the application of the integro–differential model proposed herein. We also show that the cantilever beam paradox can be successfully resolved.

Consider a straight, homogeneous, isotropic beam of length L, constant rectangular cross section $b \times h$ (b being the width and h being the height). The x–axis is taken along the geometric centroid of the beam cross section and the z–coordinate is taken positive upward. The only nonzero strain in the Euler–Bernoulli beam theory [51] is

$$\varepsilon(x) = \frac{du}{dx} - z\frac{d^2w}{dx^2} \tag{4.26}$$

The nonlocal stress is determined using Eq. (4.5):

$$\sigma(x) = \xi_1 E\left(\frac{du}{dx} - z\frac{d^2w}{dx^2}\right) + \int_0^L \int_{A'} \xi_2 \alpha(x, x', l_c)\, E\left(\frac{du}{dx} - z\frac{d^2w}{dx^2}\right) dA'dx' \tag{4.27}$$

Applying the general calculations of Subsection 4.2.2 to the present case, one can derive the one–dimensional finite element formulation for an element of a beam under the action of distributed horizontal and transverse loads, $f(x)$ and $q(x)$, respectively. Note that, since the governing equation for the Euler–Bernoulli beam is a fourth order equation, integration by parts is

applied twice for the term containing w. This makes the calculations slightly different from those of Subsection 4.2.2. The finite element formulation takes the form of Eq. (4.18):

$$\xi_1 \begin{bmatrix} \left(\mathbf{k}_e^l\right)^{11} & \mathbf{0} \\ \mathbf{0} & \left(\mathbf{k}_e^l\right)^{22} \end{bmatrix} \begin{Bmatrix} \mathbf{\Delta}_e^1 \\ \mathbf{\Delta}_e^2 \end{Bmatrix} + \xi_2 \sum_{e'=1}^{N_{el}} \begin{bmatrix} \left(\mathbf{k}_{ee'}^{nl}\right)^{11} & \mathbf{0} \\ \mathbf{0} & \left(\mathbf{k}_{ee'}^{nl}\right)^{22} \end{bmatrix} \begin{Bmatrix} \mathbf{\Delta}_{e'}^1 \\ \mathbf{\Delta}_{e'}^2 \end{Bmatrix} = \begin{Bmatrix} \mathbf{F}_e^1 \\ \mathbf{F}_e^2 \end{Bmatrix} \tag{4.28}$$

where

$$\left(\mathbf{k}_e^l\right)_{ij}^{11} = \int_{x_1^e}^{x_2^e} EA^e \frac{d\psi_i^e}{dx} \frac{d\psi_j^e}{dx} dx, \quad i,j = 1..2 \tag{4.29}$$

$$\left(\mathbf{k}_e^l\right)_{ij}^{22} = \int_{x_1^e}^{x_2^e} EI^e \frac{d^2\phi_i^e}{dx^2} \frac{d^2\phi_j^e}{dx^2} dx, \quad i,j = 1..4 \tag{4.30}$$

$$\left(\mathbf{k}_{ee'}^{nl}\right)_{ij}^{11} = \int_{x_1^e}^{x_2^e} \int_{x_1^{e'}}^{x_2^{e'}} \alpha\left(x, x', l_c\right) EA^e A^{e'} \frac{d\psi_i^e}{dx} \frac{d\psi_j^{e'}}{dx} dx' dx, \quad i,j = 1..2 \tag{4.31}$$

$$\left(\mathbf{k}_{ee'}^{nl}\right)_{ij}^{22} = \int_{x_1^e}^{x_2^e} \int_{x_1^{e'}}^{x_2^{e'}} \alpha\left(x, x', l_c\right) EI^e A^{e'} \frac{d^2\phi_i^e}{dx^2} \frac{d^2\phi_j^{e'}}{dx^2} dx' dx, \quad i,j = 1..4 \tag{4.32}$$

$$\left(\mathbf{\Delta}^e\right)^1 = \left\langle u_1^e \quad u_2^e \right\rangle^T, \quad \left(\mathbf{\Delta}^e\right)^2 = \left\langle w_1^e \quad \theta_1^e \quad w_2^e \quad \theta_2^e \right\rangle^T \quad \left(\theta_i^e = -\left.\frac{dw}{dx}\right|_{x=x_i^e}\right) \tag{4.33}$$

$$\left(\mathbf{F}_e\right)_i^1 = \int_{x_1^e}^{x_2^e} f\left(x\right) \psi_i^e dx + \sum_{j=1}^{2} P_j \psi_j^e\left(x_i^e\right), \quad i,j = 1..2 \tag{4.34}$$

$$\left(\mathbf{F}_e\right)_i^2 = \int_{x_1^e}^{x_2^e} q\left(x\right) \phi_i^e dx + \sum_{j=1}^{4} Q_j \phi_j^e\left(x_i^e\right), \quad i,j = 1..4 \tag{4.35}$$

and ψ_i^e and ϕ_i^e are the linear Lagrange and Hermite cubic interpolations functions, respectively. Since the cross section of the beam is assumed to be constant, the subscripts e and e' over A and I in Eqs. (4.29) to (4.32) can be eliminated. Also in the above equations $x_1^e\left(x_1^{e'}\right)$, and $x_2^e\left(x_2^{e'}\right)$ are the x–coordinate of the first and last nodes of element $e\left(e'\right)$, respectively. Substituting for $\alpha\left(x, x', l_c\right)$ from Eq. (4.24) one can rewrite $\mathbf{k}_{ee'}^{nl}$ as

$$\left(\mathbf{k}_{ee'}^{nl}\right)_{ij}^{11} = \int_{x_1^e}^{x_2^e} \int_{x_1^{e'}}^{x_2^{e'}} \frac{1}{2l_c} e^{-\frac{|x-x'|}{l_c}} EA^e \frac{d\psi_i^e}{dx} \frac{d\psi_j^{e'}}{dx} dx' dx, \quad i,j = 1..2 \tag{4.36}$$

$$\left(\mathbf{k}_{ee'}^{nl}\right)_{ij}^{22} = \int_{x_1^e}^{x_2^e} \int_{x_1^{e'}}^{x_2^{e'}} \frac{1}{2l_c} e^{-\frac{|x-x'|}{l_c}} EI^e \frac{d^2\phi_i^e}{dx^2} \frac{d^2\phi_j^{e'}}{dx^2} dx' dx, \quad i,j = 1..4$$

The final assembled form of the equations is

$$\left(\xi_1 \mathbf{K}^l + \xi_2 \mathbf{K}^{nl}\right) \mathbf{U} = \mathbf{F} \tag{4.37}$$

where $\mathbf{U}$ and $\mathbf{F}$ are the global vectors of nodal displacements and nodal forces, respectively, and $\mathbf{K}^l$ and $\mathbf{K}^{nl}$ are the assembled local and nonlocal global stiffness matrices, respectively.

4.3 Numerical Results

4.3.1 General Comments

In this section, numerical results are presented for the Euler–Bernoulli beam theory with nonlocal constitutive relation of the form of Eq. (4.27). Four different types of boundary conditions and load conditions are considered here (Figure 4.1):

(a) Clamped beam with uniformly distributed load.

(b) Simply supported beam with uniformly distributed load.

(c) Cantilever beam with a concentrated load applied to the free end.

(d) Cantilever beam with non–uniform triangular distributed load.

In all cases, a uniform rectangular cross section with width b and height h is considered. The problems are solved for three different values of length scale parameter, l_c, and five different values of phase parameter, ξ_1. The value of the length scale parameter is chosen to be much smaller than the length of the beam. The nonlocal interactions are considered to exist only within the influence zone. If the mesh is such that only part of an element falls into this zone, the nonlocal interaction between that element and the element of interest is neglected. This causes the discretized integral form of Eq. (4.18) to be mesh–dependent to some degree for coarse meshes which will be discussed later. The integral equations are solved numerically using Gauss–Legendre quadrature rule.

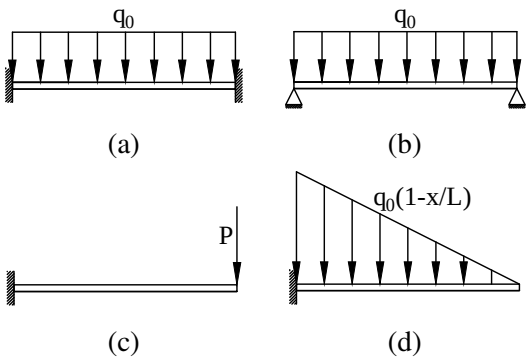

Figure 4.1: Analysis cases with different load conditions and boundary conditions.

In all of the examples presented here the length to height ratio of the beam is chosen to be 40. Therefore, assumption of a thin beam theory is appropriate and the fact that Euler–Bernoulli beam theory neglects shear deformation does not introduce a significant error into the solution.

4.3.2 Clamped Beam with Uniform Distributed Load

The first example deals with a clamped beam of length L, constant bending stiffness EI, and uniformly distributed load of intensity q_0. The maximum deflection according to the local beam model is $w(L/2) = q_0 l^4/384EI$. For a beam with constant EI, the conventional FEM gives the exact deflection. The nonlocal deflections are normalized with respect to the maximum deflection of the conventional local beam. The deflections of the beam for the purely nonlocal case $(\xi_1 = 0)$ and 3 different values of l_c, namely $l_c = 0.01L,\ 0.015L$, and $0.02L$, are shown in Figure 4.2. It is clear that for the purely nonlocal case an increase in length scale parameter, l_c, makes the beam more flexible and consequently increases the deflection of the beam. This is consistent with most of the reported results in the literature concerning Eringen nonlocal model (for instance [93, 102, 104, 105]), whereas DiPaola et al. [116] reported an opposite trend for constant ξ_1 and varying l_c. According to Figure 4.2 the transverse deflection of the beam can increase up to about 15% for $l_c = 0.02L$.

The results for the maximum normalized deflection for three different values of l_c and varying phase parameter are shown in Figure 4.3, where $\xi_1 = 0$ and $\xi_1 = 1$ correspond to purely nonlocal

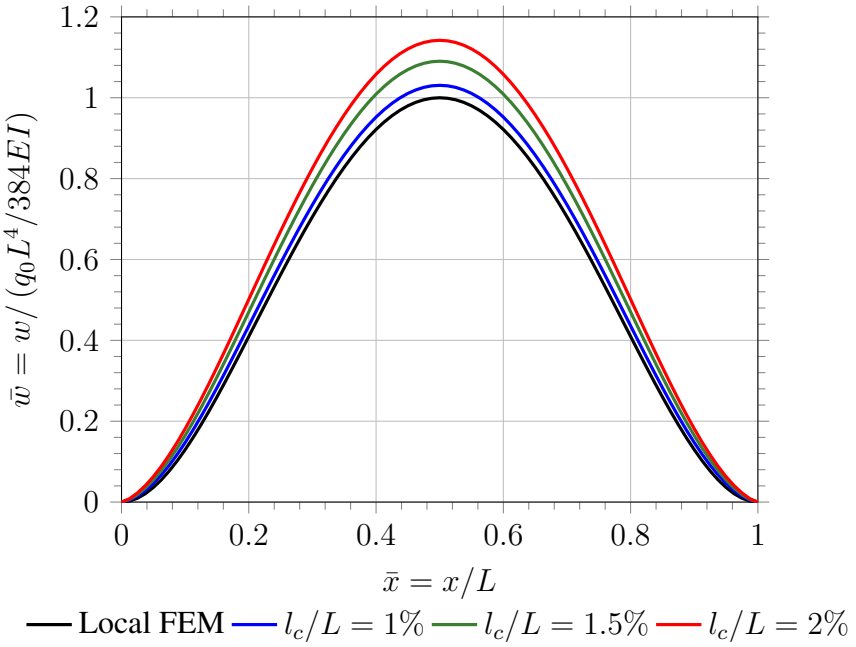

Figure 4.2: Normalized deflection of a clamped beam with uniformly distributed load and $\xi_1 = 0$.

and purely local constitutive models, respectively. It is clear that the normalized maximum deflection increases with a decrease in the phase parameter, that is, an increase in the nonlocal part of Eq. (4.27). One can conclude that for a clamped beam an increase in l_c and decrease in ξ_1 results in a more flexible beam. It is worth mentioning that higher l_c and lower ξ_1 both denote higher nonlocal effects in the system.

In the local approach, the case of a homogeneous beam with constant cross section having symmetric boundary conditions and loading conditions can be further simplified with the use of the inherent symmetry of the model. Using the symmetry, one can model only half of the beam $[0, L/2]$, and the displacement of the second half is the mirror image of the displacement of the first half. Due to the decrease in thesize of the domain to be modeled, the accuracy can be increased, i.e. the same number of elements in a smaller domain gives higher accuracy. Symmetry is present for a clamped beam with uniform distributed load. Use of symmetry in the nonlocal model of a clamped beam is examined next. The results for the case with symmetry are shown in Figure 4.4. Compared to the results shown in Figure 4.2, use of symmetry causes the beam to become more

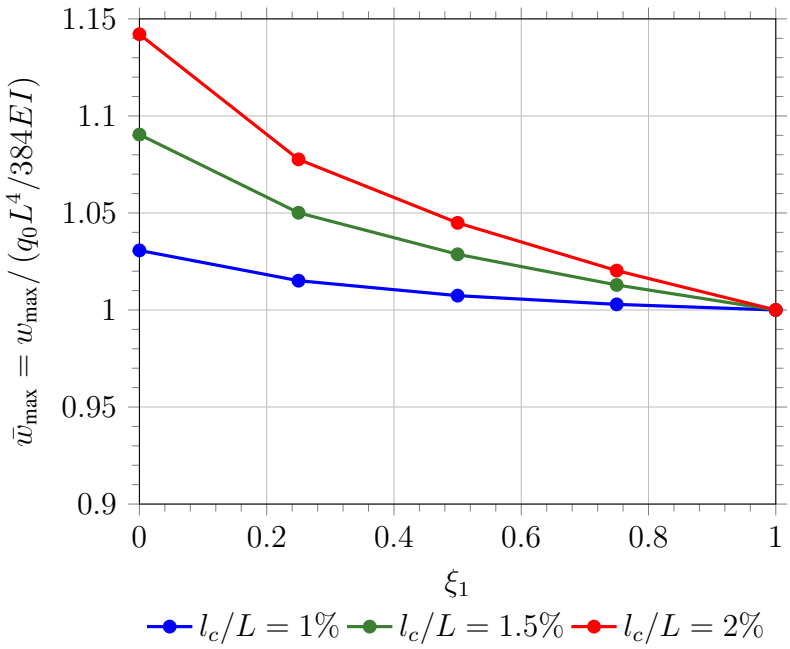

Figure 4.3: Normalized maximum deflections of a clamped beam with uniformly distributed load for different values of the length scale and phase parameters.

flexible. As stated by Pisano, Sofi, and Fuschi [115], the discretized Eringen nonlocal formulation will introduce some error near the boundaries of the model. This error is present in a zone with a dimension equal to the influence zone (which is the distance beyond which nonlocal effects are neglected). This error is due to the fact that in the integral of Eq. (4.3) it is assumed that point $\mathbf{x}$ is embedded in an infinite medium. The effect of the points located further than the influence zone from the point of interest becomes less significant on satisfying the assumption of Eq. (4.3). However, this assumption is violated at the boundaries of the medium and the integral will not result in unity. As a result of the end conditions, the stiffness terms in this zone are approximated lower than the true value. This causes the noticeable difference between the deflections of the case with symmetry and without symmetry. It can be seen that the difference is more for higher values of l_c. This shows that reduction of the domain by use of symmetry is not allowable in nonlocal analysis, unless some conditions are enforced at the end conditions to modify the resulting error in the stiffness of these areas.

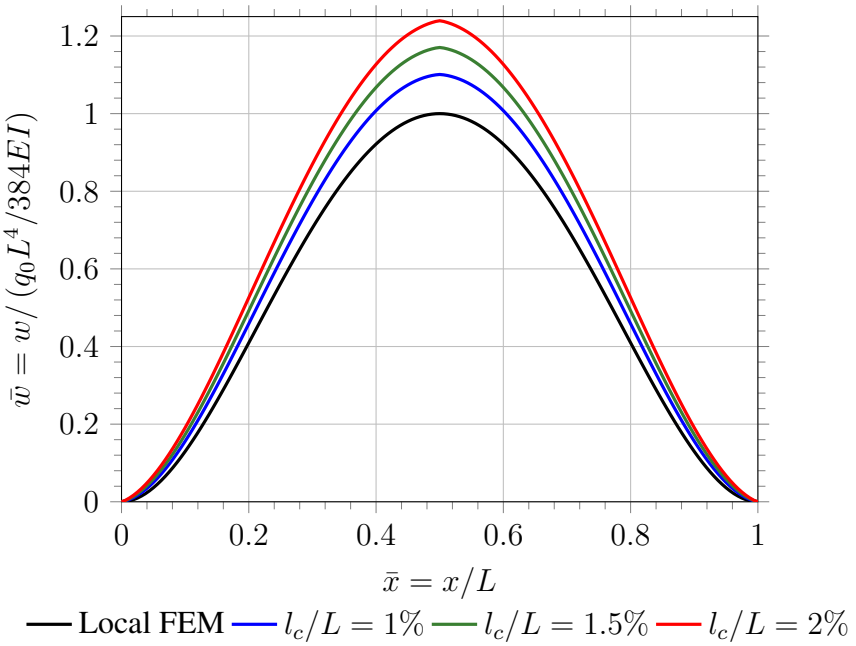

Figure 4.4: Normalized deflection of a clamped beam with uniformly distributed load and $\xi_1 = 0$ (symmetry is used in modeling only half of the beam).

Note that the error caused by end conditions is present even in the case where the full beam is analyzed. However, since in the case of a full beam the boundary conditions at the ends of the beam involve a constraint on the transverse deflection, the reduction in stiffness will not affect the deflection to the extent of the case of a half beam. In the case of a half beam, the introduced boundary condition in the middle of the beam has a constraint on the slope of the beam and not the transverse deflection. As a result, the influence of the end conditions on the deflection will become more prominent with the use of symmetry.

4.3.3 Simply Supported Beam with Uniformly Distributed Load

Next the problem of a simply supported beam under uniformly distributed transverse load of intensity q_0 is studied. The maximum local deflection of this beam is $5q_0l^4/384EI$. The normalized deflections of the beam for $\xi_1 = 0$ and 3 different values of l_c are shown in Figure 4.5. The results shown in Figure 4.5 for a simply supported beam show a different trend as compared with those shown in Figure 4.2 for a clamped beam. The deflection of the simply supported beam increases

with the increase in the length scale parameter l_c. However, the increase is not very significant. Also note that the deflections derived from the nonlocal theory are slightly smaller than their local counterpart which is not in agreement with the softening effect reported in the literature.

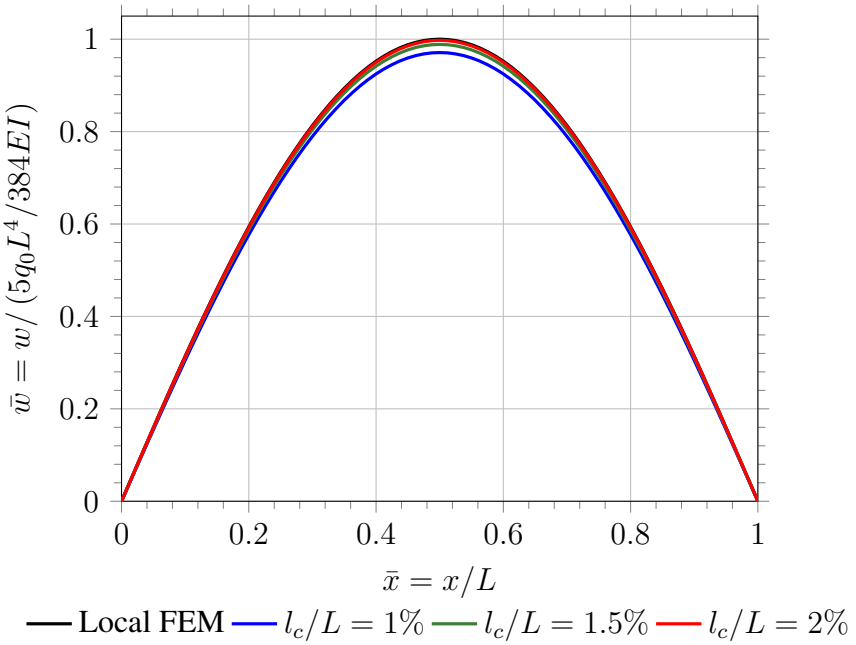

Figure 4.5: Normalized deflection of a simply supported beam with uniformly distributed load and $\xi_1 = 0$.

Same as what was done for the clamped beam, the maximum normalized deflection for three different values of l_c and varying phase parameter is shown in Figure 4.6. It is obvious that lowering the phase parameter makes the system more stiff; therefore, the tip deflection increases with increasing ξ_1. This is in contradiction with the results of the clamped beam (Figure 4.3). In general, for the simply supported beam a decrease in ξ_1 decreases the deflection as opposed to other boundary conditions and the reported results in the literature. One should note that the kernel function used in this study is different from the one which gives rise to Eringen's differential nonlocal model. The differential model comes from a kernel function with a Gaussian distribution; therefore, differences are to be expected. As will be shown next, the kernel function used here

(Eq. (4.4)) eliminates the paradox concerning the cantilever beam, however, it introduces another paradox for the simply supported beam.

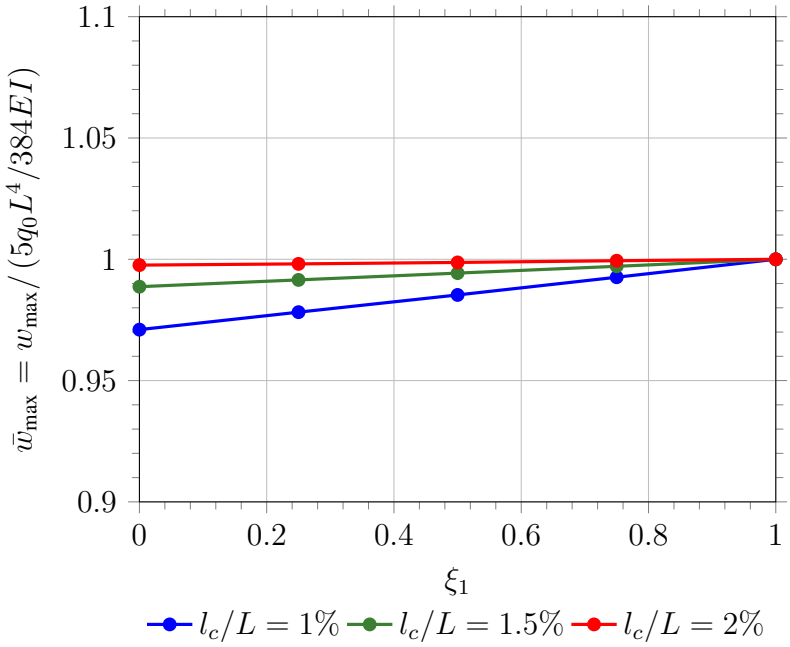

Figure 4.6: Normalized maximum deflections of a simply supported beam with uniformly distributed load for different values of the length scale and phase parameters.

Although for the case of a simply supported beam the nonlocal transverse deflections are smaller than the local deflections, by increasing the number of elements in the beam the results of the local and nonlocal analysis converge and the difference between the results will decrease. This is shown in Figure 4.7 for $l_c = 0.01L$ (for which according to Figure 4.5 the difference between local and nonlocal deflections was larger among the different values considered for l_c) and increasing number of elements.

Similar to the clamped beam, the analysis of the half beam with the use of inherent symmetry of the simply supported beam was performed. It was once again concluded that huge errors will be introduced into the problem, if the stiffness of the end zone near the half beam is not modified.

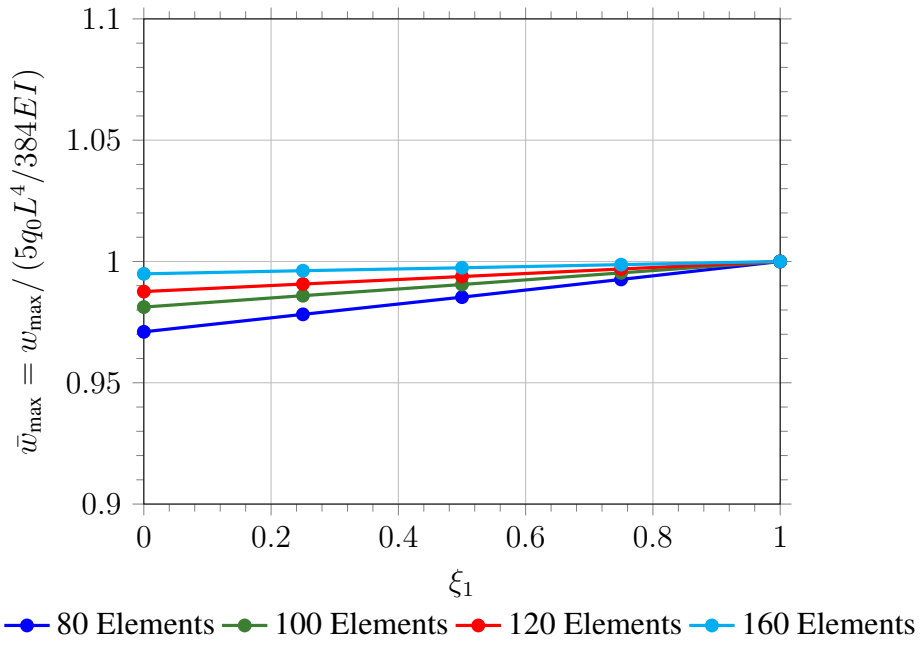

Figure 4.7: Normalized maximum deflections of a simply supported beam with uniform distributed load for different number of elements and $l_c/L = 1\%$.

4.3.4 Cantilever Beam with Concentrated Load

The third example deals with a cantilever beam with a point load at the free end. The normalized deflections are shown in Figure 4.8. The conventional (local) FEM result for the maximum deflection of a cantilever beam of length L with constant EI subjected to a concentrated load P at the free end is $PL^3/3EI$. The deflections are normalized by this value to remove the effect of other parameters. The results shown in Figure 4.8 correspond to the value of $\xi_1 = 0$ which gives the original one–phase Eringen nonlocal formulation of Eq. (4.1). The results show that as expected the increase in the length scale parameter l_c makes the system more flexible and the deflections are increased which is in agreement with the trend of the clamped beam and the results stated in the literature [93, 102, 104, 105]. Although an increase in the deflection is noticed, this increase is not very significant. The maximum increase in the deflection of the tip of the beam is about 5% for $l_c = 0.02L$. The results for $l_c = 0.01L$ is almost the same as those of the conventional local FEM.

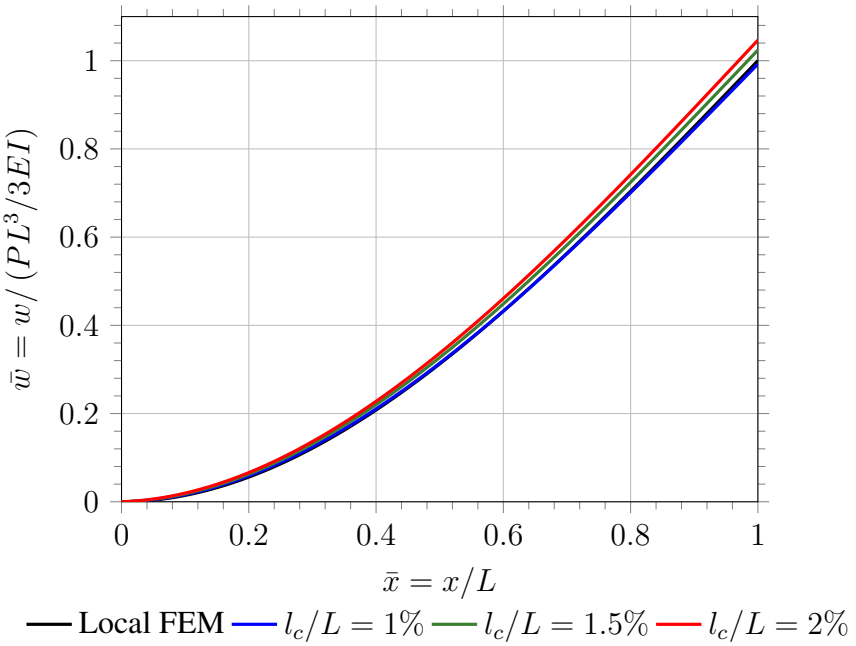

Figure 4.8: Results for a cantilever beam with point load at the free end and $\xi_1 = 0$, normalized by the local maximum deflection.

The normalized deflection of the tip of the beam for varying phase parameter ξ_1 is shown in Figure 4.9. The results are provided for three different values of l_c and five values of ξ_1. Similar to the clamped beam, the results show that the deflections increase with the decrease in the phase parameter.

Overall, the normalized tip deflection is generally greater than unity for varying l_c and ξ_1. In Figure 4.9 the values of the normalized tip deflection for $l_c = 0.01L$ and ξ_1 other than unity are slightly smaller than unity, the reason for which is discussed later. As opposed to the results reported in several studies [65, 93, 102, 104, 117] for the paradoxical case of a cantilever beam, it can be seen that the integral form of Eringen nonlocal model (with the present choice of kernel function) results in deflections which are different from its local counterpart.

4.3.5 Cantilever Beam with Non–uniform Distributed Load

Finally, the case of a cantilever beam with triangular distributed load (Figure 4.1d) is studied here. The maximum deflection for the conventional case is $q_0 L^4/30EI$. Normalized displacements

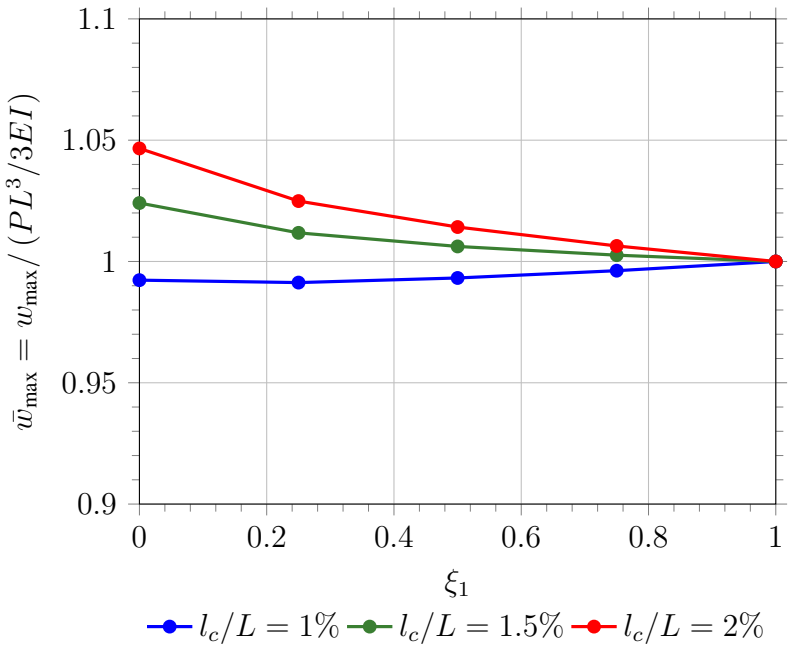

Figure 4.9: Normalized deflections of the tip of a cantilever beam with a point load at the tip for different values of length scale parameter and phase parameter.

for varying l_c and $\xi_1 = 0$ are shown in Figure 4.10, and normalized deflections of the tip of the beam for different values of l_c and ξ_1 are shown in Figure 4.11. The trend is the same as in the previous cases of a clamped beam and a cantilever beam with a point load. By comparing the plots of Figure 4.11 with those in Figure 4.9 one can realize that the increase in deflection due to nonlocal effects is more significant for the cantilever beam with the triangular distributed load compared to the one with a point load at the tip. Although the results for a cantilever beam with uniformly distributed load are not brought here, the deflections of the case of the triangular distributed load even exceed those of the uniformly distributed load. This can be attributed to the derivations by Reddy [105] which shows that the derivative of $q(x)$ (transverse distributed force) come into the picture in the differential form of the nonlocal Eringen model.

4.4 Assessment of the Discrete Eringen Nonlocal Formulation

As discussed in the introduction, most of the studies in the literature used the differential form of the Eringen nonlocal model. Now the discrete integral model is evaluated to determine its

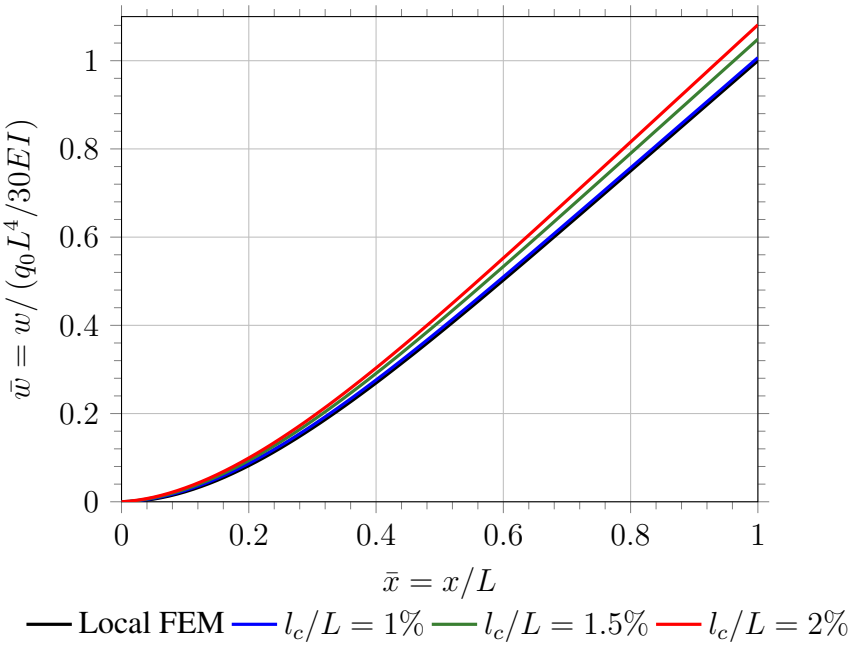

Figure 4.10: Normalized deflection of a cantilever beam with triangular distributed load and $\xi_1 = 0$.

applicability to the problems.

After finite element discretization of the domain and development of element–wise equations, the elements are assembled using the connectivity matrix. The connectivity matrix is a rectangular array whose i^{th} row gives the element numbers which are located in the influence zone of element i. A schematic view of the determination of the element numbers in the i^{th} row of the connectivity matrix is shown in Figure 4.12. As shown in the figure, first the exponential term of Eq. (4.25) is constructed at the end nodes of the i^{th} element (shown as a blue line). Next, the horizontal line corresponding to the criterion e^{-l_i/l_c} is constructed (shown as a red line). The distance between the intersection of the red line and the blue line (from constructing the exponential term at end nodes of element i) is equal to $2l_i + h_i$, where l_i is the influence zone and h_i is the length of element i, and it is named as the nonlocal zone of element i (as shown in Figure 4.12). In the final step, the elements remaining in the nonlocal zone of element i are determined. These elements form the i^{th} row of the connectivity matrix. This can be repeated for the rest of the elements to construct the

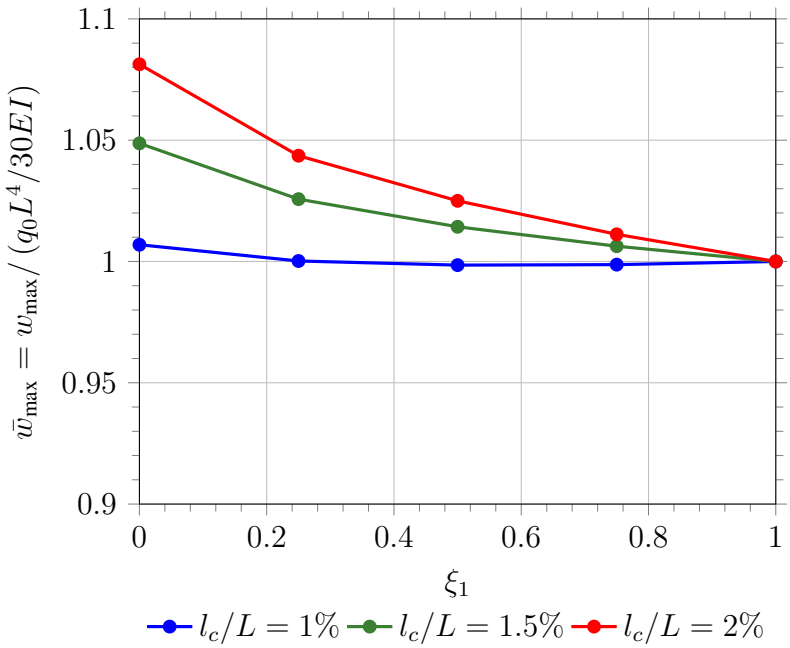

Figure 4.11: Normalized tip deflections of a cantilever beam with a triangular distributed load for different values of length scale and phase parameters.

connectivity matrix (Figure 4.13).

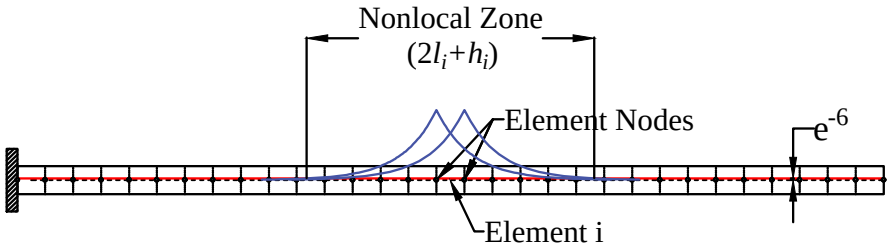

Figure 4.12: Determination of the elements falling in the influence zone of element i.

By examining Figure 4.13 one can see that for the elements located in a distance equal to the influence zone from the boundaries of the beam the integral equation of Eq. (4.3) is not satisfied. This causes the results to have some undesirable changes in these areas. On the other hand, as it is obvious from the figure, the nonlocal stiffness $\mathbf{k}_{ee'}^{nl}$ depends highly on the mesh distribution

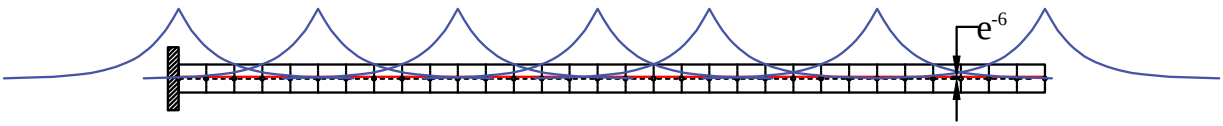

Figure 4.13: Constructing the connectivity matrix.

(l_c is chosen to be much smaller than the length of the beam). The accuracy of the results in the integral form depends on the relative value of l_c and the mesh size. If the mesh is very coarse, the finite element solution will not converge to the true solution. Therefore, to obtain accurate results the mesh size needs to be determined according to the length scale parameter, l_c. To illustrate this, the final results for the normalized maximum transverse deflection of a clamped beam with uniformly distributed load are shown in Table 4.1 for different values of length scale parameter, phase parameter, and number of elements. Note that the length of the beam is taken to be constant, therefore, by increasing the number of elements the mesh size is decreased. As can be seen, by increasing the number of elements the results start converging. For fewer number of elements, the maximum nonlocal deflection becomes less than the corresponding local response. However, the difference between the solutions obtained with meshes of 80, 90, and 100 elements becomes negligible (the figures provided in the previous sections all correspond to a mesh of 80 elements). This shows that if the integral form of the Eringen model is to be used, a sensitivity analysis should be conducted on the mesh size before final analysis. Note that according to the results presented in Table 4.1, the sensitivity of the solution to the number of elements decreases by increasing the value of the length scale parameter, l_c. This is due to the fact that an increase in l_c will result in the increase in the influence zone which will naturally increase the number of elements falling into the influence zone.

4.5 Clamped vs. Simply Supported Beam

Except for the simply supported beam, all of the numerical examples presented in Section 4.3 show the following trends with the change in the nonlocal parameters, l_c and ξ_1:

1. The deflection increases with the increase in the length scale parameter, l_c.

Table 4.1: Normalized maximum deflections for a clamped beam with uniformly distributed load for different numbers of elements, phase parameter, and length–scale parameter.

	Number of elements	Normalized nonlocal deflection $\xi_1 = 0.00$	$\xi_1 = 0.25$	$\xi_1 = 0.50$	$\xi_1 = 0.75$	$\xi_1 = 1.00$
$l_c/L = 0.010$	20	0.6891	0.7469	0.8154	0.8982	1.0000
	40	0.9252	0.9402	0.9579	0.9779	1.0000
	80	1.0307	1.0151	1.0074	1.0029	1.0000
	90	1.0387	1.0200	1.0106	1.0044	1.0000
	100	1.0451	1.0239	1.0131	1.0056	1.0000
$l_c/L = 0.015$	20	0.8638	0.8925	0.9246	0.9602	1.0000
	40	1.0274	1.0124	1.0051	1.0014	1.0000
	80	1.0904	1.0501	1.0287	1.0129	1.0000
	90	1.0960	1.0529	1.0304	1.0137	1.0000
	100	1.1003	1.0549	1.0317	1.0143	1.0000
$l_c/L = 0.020$	20	0.9689	0.9717	0.9784	0.9880	1.0000
	40	1.0951	1.0546	1.0310	1.0137	1.0000
	80	1.1421	1.0776	1.0449	1.0203	1.0000
	90	1.1466	1.0794	1.0460	1.0208	1.0000
	100	1.1495	1.0802	1.0464	1.0211	1.0000

2. The deflection increases with the decrease in the phase parameter, ξ_1.

3. The nonlocal deflection ($\xi_1 \neq 1$) is generally larger than the local deflection.

For the simply supported beam the same trend with respect to variations of l_c is noticed. However, the last two trends are not observed. The normalized deflection (nonlocal deflection divided by the maximum local deflection) is always less than or equal to unity (equality to 1 corresponds to the case of $\xi_1 = 1$); also, the normalized deflection decreases with decreasing ξ_1. To study this further, a simply supported beam with rotational springs at both ends with equal spring constants of μ, Figure 4.14, is considered. The case of $\mu = 0$ corresponds to a simply supported beam, while $\mu \to \infty$ corresponds to a clamped beam. It is understood that one cannot reach infinity numerically, however, for a value of μ large enough the deflections of the clamped beam are attained.

To observe how the transition from the simply supported beam to the clamped beam occurs, maximum nonlocal deflection for different values of μ, l_c, and ξ_1 is obtained. Once again the

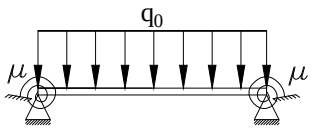

Figure 4.14: Simply supported beam with rotational springs with constant μ at both ends.

results are normalized with respect to the maximum local deflection. The results are tabulated in Table 4.2 for different values of the normalized rotational stiffness, $\mu L/EI$, normalized length scale parameter, l_c/L, and phase parameter ξ_1. The values of normalized deflection that are larger or equal to unity are highlighted in the table. For $\mu L/EI = e^0 = 1$, the results are almost the same as the simply supported beam (note that in this case, μ acquires a small value, $\mu = EI/L \neq 0$). The nonlocal simply supported beam behaves slightly stiffer compared to its local counterpart. Also note that the normalized deflection for $\mu L/EI = e^{10}$ and $\mu L/EI = e^{12}$ are the same and convergence to the clamped beam has been made. One can see that the nonlocal clamped beam is more flexible than the local clamped beam. As expected, the normalized deflection for $\xi_1 = 1$, purely local constitutive equation, will be exactly equal to 1 for all values of l_c/L and $\mu L/EI$. For other values of ξ_1, with an increase in l_c the change from a stiffer nonlocal system to a softer nonlocal system takes place with a lower value of the rotational stiffness spring μ.

Finally, the normalized maximum transverse deflections for a wider range of values of ξ_1 and $\mu L/EI$ and a constant value of $l_c/L = 0.02$ are shown in Figure 4.15. Since μ changes from very small values to very large values, the $\mu L/EI$ is presented in the logarithmic form. The figure shows that for $l_c/L = 0.02$, only a very small range of $\mu L/EI$ gives normalized values of less than unity. With the increase of μ the normalized deflection increases to about 1.14. Due to the difference in the kernel function used in this study as compared to the underlying kernel function for the differential Eringen nonlocal model, one should expect some differences to arise. The advantage of the integro–differential model with the exponential kernel function of Eq. (4.4) is that it solves the afore–mentioned controversy for cantilever beams which has many applications in science [94–97].

Table 4.2: Normalized maximum deflections of a simply supported beam with rotational springs at both ends for different values of $\mu L/EI$, l_c/L, ξ_1.

	$\mu L/EI$	Max. Local Deflection	Normalized Maximum Nonlocal Deflection				
			$\xi_1 = 0.00$	$\xi_1 = 0.25$	$\xi_1 = 0.50$	$\xi_1 = 0.75$	$\xi_1 = 1.00$
$l_c/L = 0.010$	10^0	1.3333	0.9710	0.9782	0.9853	0.9926	1.0000
	10^2	1.3325	0.9710	0.9781	0.9853	0.9926	1.0000
	10^4	1.2543	0.9728	0.9795	0.9862	0.9931	1.0000
	2×10^4	1.1862	0.9745	0.9807	0.9870	0.9934	1.0000
	5×10^4	1.0286	0.9785	0.9836	0.9889	0.9944	1.0000
	10^5	0.8593	0.9837	0.9872	0.9913	0.9955	1.0000
	2×10^5	0.6769	0.9910	0.9919	0.9942	0.9970	1.0000
	5×10^5	0.4800	1.0028	0.9992	0.9985	0.9989	1.0000
	10^6	0.3852	1.0118	1.0044	1.0015	1.0003	1.0000
	10^8	0.2680	1.0304	1.0149	1.0074	1.0028	1.0000
	10^{10}	0.2667	1.0307	1.0150	1.0074	1.0028	1.0000
	10^{12}	0.2667	1.0307	1.0150	1.0074	1.0028	1.0000
$l_c/L = 0.015$	10^0	1.3333	0.9887	0.9915	0.9943	0.9971	1.0000
	10^2	1.3325	0.9887	0.9915	0.9943	0.9971	1.0000
	10^4	1.2543	0.9897	0.9922	0.9947	0.9974	1.0000
	2×10^4	1.1862	0.9907	0.9928	0.9952	0.9976	1.0000
	5×10^4	1.0286	0.9939	0.9948	0.9964	0.9982	1.0000
	10^5	0.8593	0.9994	0.9983	0.9985	0.9991	1.0000
	2×10^5	0.6769	1.0093	1.0041	1.0020	1.0007	1.0000
	5×10^5	0.4800	1.0301	1.0160	1.0089	1.0039	1.0000
	10^6	0.3852	1.0483	1.0264	1.0150	1.0066	1.0000
	10^8	0.2680	1.0897	1.0497	1.0285	1.0128	1.0000
	10^{10}	0.2667	1.0904	1.0501	1.0287	1.0129	1.0000
	10^{12}	0.2667	1.0904	1.0501	1.0287	1.0129	1.0000
$l_c/L = 0.020$	10^0	1.3333	0.9976	0.9981	0.9987	0.9994	1.0000
	10^2	1.3325	0.9975	0.9981	0.9987	0.9993	1.0000
	10^4	1.2543	0.9982	0.9986	0.9990	0.9995	1.0000
	2×10^4	1.1862	0.9992	0.9990	0.9992	0.9996	1.0000
	5×10^4	1.0286	1.0024	1.0009	1.0004	1.0001	1.0000
	10^5	0.8593	1.0092	1.0046	1.0026	1.0011	1.0000
	2×10^5	0.6769	1.0225	1.0120	1.0068	1.0031	1.0000
	5×10^5	0.4800	1.0523	1.0283	1.0163	1.0074	1.0000
	10^6	0.3852	1.0792	1.0431	1.0249	1.0112	1.0000
	10^8	0.2680	1.1410	1.0771	1.0446	1.0201	1.0000
	10^{10}	0.2667	1.1420	1.0776	1.0449	1.0203	1.0000
	10^{12}	0.2667	1.1420	1.0776	1.0449	1.0203	1.0000

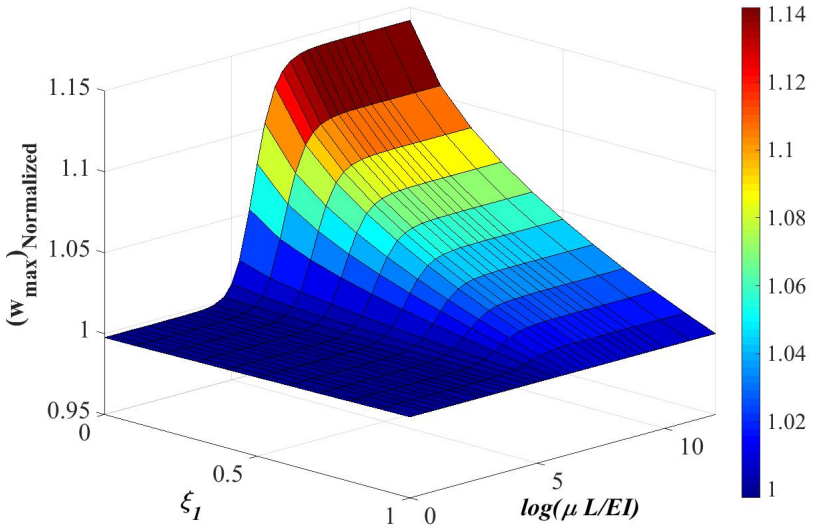

Figure 4.15: Normalized maximum deflections of a simply supported beam with rotational springs at both ends, $l_c/L = 0.02$, varying value of ξ_1 and $\mu L/EI$.

According to most of the studies in the literature Eringen nonlocal model has a softening effect (e.g. [93, 101, 102, 104]), i.e. the displacements of the Eringen nonlocal model are typically higher than their local counterpart, while the frequencies are generally lower. However, the studies by Reddy and El–Borgi [109] and Li et al. [120] showed that the behavior of the Eringen nonlocal model depends upon the type of loading and boundary conditions compared to their corresponding local counterpart. Although the stiffness may increase in some cases, there exists some cases where it has a softening effect [109, 120]. This further supports the results obtained in the present study.

4.6 Chapter Summary and Conclusions

A unified nonlocal integro–differential model is proposed as a generalization of Eringen's nonlocal model. In the present study the constitutive equation is written as a linear combination of local and nonlocal constitutive theories. The present model gives rise to two key parameters, namely the length scale parameter, l_c, and the phase parameter, ξ_1. General three–dimensional finite element formulation for the integro–differential model is presented. Then the results are specialized to the case of the Euler–Bernoulli beam theory. It is shown through numerical examples that the nonlocal beam is more flexible than its local counterpart for most boundary conditions (other than the

case of a simply supported beam). The paradox surrounding the cantilever beam disappears with the integro–differential model proposed herein, which is very beneficial in the study of micro–and nano–cantilevers. This can also be attributed to the different choice of kernel function as compared to the underlying kernel function for the differential form of Eringen's nonlocal model.

As shown in this study, as with other numerical frameworks the accuracy of the discrete form of the integral model depends on the mesh size, and it converges to the true solution by increasing the number of elements. However, note that due to the existence of the nonlocal stiffness matrix, $\mathbf{k}_{nl}^{ee'}$, increasing the number of nonlocal interactions will result in a global stiffness matrix with more nonzero terms (i.e., larger bandwidth) and consequently higher memory demand. The determination of the elements which are within the influence zone of a specific element becomes more challenging for two–dimensional and three–dimensional problems, which is a topic of future study. These are most likely the reasons why most of the previous studies made use of the differential form of the Eringen model. However, the integral form can be used to handle the problematic case of cantilever beams.

Application of the integro–differential model to other beam theories (e.g., the Timoshenko and Reddy third–order beam theories) is straightforward. However, extension and application of the ideas presented herein to plates and shells is more challenging and requires attention. It is also interesting to see how the integro–differential model predicts the vibration response in fundamental and higher modes of vibration. It is hoped that with the publication of the present study, a number of other studies will ensue.

5. A UNIFIED BEAM THEORY WITH STRAIN GRADIENT EFFECT AND THE VON KÁRMÁN NONLINEARITY*

5.1 Introduction

5.1.1 Nonlocal Theories

Classical continuum mechanics has proven to be very useful in the study of a variety of problems of engineering and applied sciences. However, recent developments in the field of materials science and emergence of new materials necessitate the need for new theories that account for certain material length scales. Conventional continuum mechanics is inherently scale–free; therefore, the stress at each point depends only on the strain at that point. However, there exist examples where continuum mechanics does not suffice. Nonlocality by itself does not have a single specific definition, and "it can arise from the way we choose to model physical phenomena" (see [121]). In nonlocal theories, as opposed to local theories, it is assumed that particles further apart will also influence each other. Several nonlocal theories exist which consider the long–range interactions between materials particles. These theories can be broadly divided into two major groups:

1. Weakly nonlocal theories (such as strain gradient theories [122–124] and modified couple stress theories [125–130]) where stress at each point depends not only on the strain but also on the derivatives of the strain. These are non–classical mechanics theories in the sense that they account for couple stress effect and the material length scale comes in through a constitutive equation relating the couple stress tensor and curvature tensor.

2. Strongly nonlocal theories (such as Eringen integral theory[2] [88–90, 105, 106, 131], and peridynamic theory [13, 69]), where stress at each point depends on the strain at all points within

*Reprinted with permission from "A unified beam theory with strain gradient effect and the von Kármán Nonlinearity" by P. Khodabakhshi, and J. N. Reddy, 2017. *ZAMM –Journal of Applied Mathematics and Mechanics / Zeitschrift für Angewandte Mathematik und Mechanik*, 97(1), 70–91, Copyright 2016 by John Wiley and Sons.

[2]Eringen's model is originally in integral form. However, for a special class of kernel functions the original formulation is transformed into a differential model which can be considered as an example of stress gradient theories. However, both integral form and differential form of Eringen nonlocal model are considered to be strongly nonlocal theories.

a domain through an integral.

Several papers have been published in the last ten years in these two areas, and many of them deal with beams, plates, and shells. A good list of references on these two classes of models can be found in [131] and [130]. What all nonlocal theories have in common is the introduction of material length scales which represent certain microstructural features (e.g., lattice structure). Most nonlocal theories, with the exception of the Eringen nonlocal model, exhibit a stiffening effect. This effect is more significant when a certain dimension of a structure (e.g., thickness in the case of beams, plates, and shells) becomes comparable to the length scale parameter. This is consistent with the results obtained from experiments on micro–and nano–sized structures where the size effect gives rise to enhanced stiffness. Since the focus of this study is on the strain gradient theory, the rest of the discussion is devoted to discussions on this theory.

5.1.2 Background on Strain Gradient Theories

Mindlin [122] was the first to formulate a general strain gradient theory where first–and second–order strain gradients (as well as the strain itself) were included in the strain energy. The theory resulted in 18 independent material constants (two of which are the Lamé constants) for an isotropic homogeneous elastic material. The extra material constants were material length scales corresponding to the additional strain gradients. Later, several attempts were made to reduce the number of material length scales [132–134]. Altan and Aifantis [123] simplified the strain gradient theory presented by Mindlin and Eshel [132][3] to a theory with only one material length scale in addition to the Lamé constants. This theory [123] is the simplest strain gradient theory available in the literature. Lam et al. [134] proposed a modified strain gradient theory with three material length scales accounting for dilatation gradient, and deviatoric stretch gradient, as well as the rotation gradient present in modified couple stress theory.

Gao and Park [135] used the strain gradient theory proposed by Altan and Aifantis [123] to construct a variational formulation for a three–dimensional elasticity problem and determine the corresponding equilibrium equations and consistent boundary conditions. Several studies have

[3] With five material length scales.

been reported on the study of strain gradient homogeneous beams [136–139], functionally–graded beams with strain gradient theory [140, 141], and beams accounting for nonlinearity [142]. Couple stress theory can be assumed as a form of strain gradient theory where only rotation gradients (the antisymmetric part of the second order deformation gradients) are considered and the symmetric part is neglected [134, 143]. Lim, Zhang, and Reddy [143] proposed a higher–order nonlocal theory where both strain gradients and stress gradients are present. The theory can be considered as a combination of Eringen nonlocal model (differential form) and classical strain gradient theory. The findings of the study demonstrate a good match with results from lattice dynamics, which couldn't be satisfied with each of the theories (Eringen nonlocal model and classical strain gradient theory) individually. Yaghoubi, Mousavi, and Paavlova [144] and Mousavi, Paavlova, and Reddy [145] integrated velocity gradients with the strain gradient theory of Altan and Aifantis [123] to study the effect of material length scales in dynamic problems of beams and plates. Static and kinetic length scales are chosen to be different. Microstructure–dependent beams have significant applications in the study of nano–or micro–sized beam–like components. Nano–sensors and nano–actuators are used frequently in biological, chemical, and engineering sciences [94, 95, 146].

5.1.3 Present Study

Several papers have appeared on the study of strain gradient beams; however, most of the studies are devoted to one beam theory or another, and most of them do not account for the von Kármán nonlinearity. In this study attempt is made to unify the familiar beam kinematics of the Euler–Bernoulli, Timoshenko, and Reddy third–order beam theories into a single unified beam theory while considering for both the strain gradient effect and the von Kármán nonlinearity. Nonlinear finite element formulation of the unified beam theory with strain gradient and the von Kármán nonlinear effects is developed. Individual effect of the kinematics as well as combined effect of boundary conditions, material length scale, and nonlinearity on the bending response are studied. Formulations for each beam theory can be derived by assigning appropriate values to a set of parameters introduced in the unified beam theory. The unified beam theory can be used to develop a finite element code that can model strain gradient beams with any of the three beam kinematics.

Section 5.2 includes a summary on the form of the strain energy density function of strain gradient theories. Section 5.3 covers the definition of the von Kármán nonlinearity, displacement fields of various beam theories, and the definitions and formulations of the unified beam theory. Section 5.4 provides the theoretical formulation to derive the governing equations and the associated boundary conditions for the proposed beam theory using the principle of virtual displacements. In Section 5.5 nonlinear finite element formulation and the corresponding tangent matrix for strain gradient unified beam are developed. Several numerical examples are provided in Section 5.6 to study the individual influence of shear deformation (different beam theories), strain gradient, and the von Kármán nonlinearity on transverse deflection. Finally, an example including all factors is presented. Concluding remarks are provided in Section 5.7.

5.2 Strain Gradient Theory

Strain energy density function is different for strain gradient theory as compared to conventional theory in that it includes additional terms due to the couple stress. The strain energy potential in classical theories only depends on the strains, whereas in the strain gradient theory it depends not only on the strain but also on the gradients of the strain. This brings a material length scale (a size–dependent property) into the formulation.

The strain energy potential for a linearized strain gradient theory is a function of the strains and their gradients:

$$U_0 = U_0\left(\varepsilon_{ij}, \varepsilon_{ij,k}\right) \tag{5.1}$$

Throughout the text "$()_{,k}$" is the notation used for differentiation with respect to x_k. Therefore, $\varepsilon_{ij,k} = \frac{\partial \varepsilon_{ij}}{\partial x_k}$. The components of the Cauchy stress tensor, σ_{ij} and the higher order stress tensor τ_{ijk} in linear elastic solids are determined from the strain energy potential as

$$\sigma_{ij} = \frac{\partial U_0}{\partial \varepsilon_{ij}}, \qquad \tau_{ijk} = \frac{\partial U_0}{\partial \varepsilon_{ij,k}} \tag{5.2}$$

Note that τ_{ijk} is the work conjugate of $\varepsilon_{ij,k}$ in the same manner that σ_{ij} is the work conjugate of ε_{ij} (Recall that no distinction between reference and current coordinates is made here.).

The strain energy potential is assumed to be a quadratic function of strains and gradients of strains [123, 135]. Therefore, we can write

$$U_0 = \tfrac{1}{2} C_{ijkl}\, \varepsilon_{ij}\, \varepsilon_{kl} + \tfrac{1}{2} \ell_s^2\, C_{ijkl}\, \varepsilon_{ij,m}\, \varepsilon_{kl,m} \tag{5.3}$$

where ℓ_s is the material length scale parameter. Using Eqs. (5.2) and (5.3), σ_{ij} and τ_{ijm} can be expressed in terms of the strains and strain gradients as

$$\sigma_{ij} = C_{ijkl}\, \varepsilon_{kl}, \qquad \tau_{ijm} = \ell_s^2\, C_{ijkl}\, \varepsilon_{kl,m} = \ell_s^2\, \sigma_{ij,m} \tag{5.4}$$

Finally, Eq. (5.3) can be rewritten as

$$U_0 = \tfrac{1}{2} \varepsilon_{ij}\, \sigma_{ij} + \tfrac{1}{2} \varepsilon_{ij,m}\, \tau_{ijm} \tag{5.5}$$

The total strain energy stored in the elastic body is obtained by integrating the strain energy potential over the whole domain:

$$U = \int_V U_0\, dV \tag{5.6}$$

The virtual strain energy is simply equal to (see Reddy [119])

$$\delta U = \int_V \delta U_0\, dV = \int_V \left(\delta\varepsilon_{ij}\, \sigma_{ij} + \delta\varepsilon_{ij,m}\, \tau_{ijm} \right) dV \tag{5.7}$$

5.3 One–dimensional Beam Theories

The goal of this section is to present a unified beam theory to investigate the combined effect of the strain gradient formulation and the von Kármán nonlinearity on the bending response of straight beams. Towards this objective, three distinct beam theories, namely, the Euler–Bernoulli, the Timoshenko, and the Reddy third–order beam theories [51, 119, 147] are considered. A brief description of each of the beam theories with the von Kármán nonlinearity are provided next.

5.3.1 The von Kármán Nonlinearity

The Green–Lagrange strain tensor in Cartesian coordinates can be expressed as

$$E_{ij} = \frac{1}{2}\left(\frac{\partial u_i}{\partial X_j} + \frac{\partial u_j}{\partial X_i} + \frac{\partial u_m}{\partial X_i}\frac{\partial u_m}{\partial X_j}\right) \tag{5.8}$$

where (X_1, X_2, X_3) denotes the reference coordinate system. In Eq. (5.8) summation on repeated indices is assumed.

In the case of infinitesimal strains, we assume that $\frac{\partial u_i}{\partial X_j}$ are small so that the nonlinear terms can be omitted and no distinction between the reference coordinates (X_1, X_2, X_3) and current coordinates (x_1, x_2, x_3) is made. Then Eq. (5.8) simplifies to

$$E_{ij} \approx \varepsilon_{ij} = \frac{1}{2}\left(\frac{\partial u_i}{\partial X_j} + \frac{\partial u_j}{\partial X_i}\right) = \frac{1}{2}\left(\frac{\partial u_i}{\partial x_j} + \frac{\partial u_j}{\partial x_i}\right) \tag{5.9}$$

For a one–dimensional beam, x_1 is the axis passing through the centroid of the beam and x_3 is the axis perpendicular to it. The only nonzero strains in a straight beam with inextensible normals are

$$\varepsilon_{xx} = \frac{\partial u_1}{\partial x_1}, \quad \varepsilon_{xz} = \frac{1}{2}\left(\frac{\partial u_1}{\partial x_3} + \frac{\partial u_3}{\partial x_1}\right) \tag{5.10}$$

In the case of moderate rotations yet small strains the Green–Lagrange strain tensor can be simplified to account for the von Kármán nonlinearity, where it is assumed that the nonlinear term corresponding to $\frac{\partial u_1}{\partial x_1}$ is small enough to be neglected but the nonlinear term corresponding to $\frac{\partial u_3}{\partial x_1}$ (which is a measure of rotation) is kept. Thus, we have

$$E_{xx} \approx \varepsilon_{xx} = \frac{\partial u_1}{\partial x_1} + \frac{1}{2}\left(\frac{\partial u_3}{\partial x_1}\right)^2, \quad E_{xz} \approx \varepsilon_{xz} = \frac{1}{2}\left(\frac{\partial u_1}{\partial x_3} + \frac{\partial u_3}{\partial x_1}\right) \tag{5.11}$$

The extra term in Eq. (5.11) is the source of coupling between extensional and bending responses of straight beams with moderately large rotations and small strains. Note that the bending–extensional coupling is present in curved beams even when the nonlinear terms are neglected.

5.3.2 Euler–Bernoulli Beam Theory

The Euler–Bernoulli beam theory (EBT), also known as the classical beam theory, is built upon three hypotheses: (1) inextensibility, (2) straightness, and (3) normality of the material lines transverse to the beam axis. In other words, planes normal to the axis of the beam before deformation remain rigid, plane, and normal to the axis of the beam after deformation. Consequently, the Euler–Bernoulli beam theory is not capable of accounting for the transverse shear strain ε_{xz} and Poisson's effect.

The displacement field of the EBT is given by

$$\mathbf{u} = u_1\hat{\mathbf{e}}_x + u_2\hat{\mathbf{e}}_y + u_3\hat{\mathbf{e}}_z, \quad u_1 = u\left(x\right) - zw_{,x}\left(x\right), \quad u_2 = 0, \quad u_3 = w\left(x\right) \tag{5.12}$$

where $x_1 = x$ and $x_3 = z$ are the axes along the length and height of the beam, respectively; the y–axis is taken into the plane of the beam; (u_1, u_2, u_3) are the total displacements of a point located at the point (x, y, z); and u and w are the longitudinal and transverse deflections of a point on the x–axis, which passes through the centroid of the beam.

The only nonzero von Kármán strain component for the Euler–Bernoulli beam theory is

$$\varepsilon_{xx} = \varepsilon_{xx}^{(0)} + z\varepsilon_{xx}^{(1)} \tag{5.13}$$

where

$$\varepsilon_{xx}^{(0)} = u_{,x} + \tfrac{1}{2}w_{,x}^2, \quad \varepsilon_{xx}^{(1)} = -w_{,xx} \tag{5.14}$$

5.3.3 Timoshenko Beam Theory

The Timoshenko beam theory (TBT) relaxes the normality restriction of the Euler–Benroulli beam theory by allowing for the independent rotation of a transverse normal. Thus, the planes normal to the axis of the beam before deformation will not necessarily be perpendicular to the axis of the beam after deformation. Consequently, Timoshenko beam theory can account for the

transverse shear strain. The displacement components for the TBT are

$$\mathbf{u} = u_1\hat{\mathbf{e}}_x + u_2\hat{\mathbf{e}}_y + u_3\hat{\mathbf{e}}_z, \quad u_1 = u(x) + z\phi(x), \quad u_2 = 0, \quad u_3 = w(x) \tag{5.15}$$

Similar to the EBT, the nonzero components of the simplified Green–Lagrange strain tensor are

$$\varepsilon_{xx} = \varepsilon_{xx}^{(0)} + z\varepsilon_{xx}^{(1)}, \quad \gamma_{xz} = \gamma_{xz}^{(0)} \tag{5.16}$$

where

$$\varepsilon_{xx}^{(0)} = u_{,x} + \tfrac{1}{2}w_{,x}^2, \quad \varepsilon_{xx}^{(1)} = \phi_{,x}, \quad \gamma_{xz}^{(0)} = \phi + w_{,x} \tag{5.17}$$

The assumed displacement field in Eq. (5.15) results in constant transverse shear strain (and consequently constant shear stress) across the height of the beam. This is in contradiction with the fact that top and bottom surfaces of the beam are stress free (unless a distributed shear force is applied to these surfaces). As a result, Timoshenko beam requires a shear correction factor to account for the difference between the transverse shear energy calculated from equilibrium stresses and that predicted by the Timoshenko beam theory [51, 119]. For a homogeneous beam with rectangular cross section, the shear correction factor is equal to $K_s = 5/6$.

5.3.4 Third–Order Reddy Beam Theory

The Reddy beam theory (RBT) further relaxes the restrictions of the EBT and the Timoshenko beam theory by removing the straightness condition. Therefore, it is capable of capturing the quadratic variation of the transverse shear stress across the height of the beam and avoiding the need for shear correction factor K_s. The displacement components of the RBT are

$$\mathbf{u} = u_1\hat{\mathbf{e}}_x + u_2\hat{\mathbf{e}}_y + u_3\hat{\mathbf{e}}_z, \quad u_1 = u(x) + z\phi(x) - c_1 z^3(\phi + w_{,x}), \quad u_2 = 0, \quad u_3 = w(x) \tag{5.18}$$

where $c_1 = \frac{4}{3h^2}$. The nonzero strain components are

$$\varepsilon_{xx} = \varepsilon_{xx}^{(0)} + z\varepsilon_{xx}^{(1)} + z^3\varepsilon_{xx}^{(3)}, \quad \gamma_{xz} = \gamma_{xz}^{(0)} + z^2\gamma_{xz}^{(2)} \tag{5.19}$$

where

$$\varepsilon_{xx}^{(0)} = u_{,x} + \tfrac{1}{2}w_{,x}^2, \quad \varepsilon_{xx}^{(1)} = \phi_{,x}, \quad \varepsilon_{xx}^{(3)} = -c_1\left(\phi_{,x} + w_{,xx}\right) \tag{5.20}$$

$$\gamma_{xz}^{(0)} = \phi + w_{,x}, \quad \gamma_{xz}^{(2)} = -3c_1\left(\phi + w_{,x}\right) \tag{5.21}$$

5.3.5 Unified Beam Theory

The displacement components of the three beam theories outlined in the previous sections can be cast into a unified set with the help of tracers (α_i) whose specific values will yield the three displacement fields. Let

$$u_1 = u\left(x\right) + z\left(\alpha_1\phi + \alpha_2 w_{,x}\right) + \alpha_3 z^3\left(\phi + w_{,x}\right), \quad u_2 = 0, \quad u_3 = w\left(x\right) \tag{5.22}$$

where the value of the constants $\alpha_i \ \ (i = 1, 2, 3)$ is listed in Table 5.1. Table 5.1 also includes the values of the shear correction factor, K_s. Although K_s does not show up in the displacement field, it will appear in the strain energy expression.

Table 5.1: Values of the constants of the unified equation for different beam theories.

	EBT	TBT	RBT
α_1	0	1	1
α_2	-1	0	0
α_3	0	0	-c_1
K_s	1	$5/6$	1

The nonzero strain components for the unified beam theory take the following form:

$$\varepsilon_{xx} = \varepsilon_{xx}^{(0)} + z\varepsilon_{xx}^{(1))} + z^3\varepsilon_{xx}^{(3)}, \quad \gamma_{xz} = \gamma_{xz}^{(0)} + z^2\gamma_{xz}^{(2)} \tag{5.23}$$

where

$$\varepsilon_{xx}^{(0)} = u_{,x} + \tfrac{1}{2}w_{,x}^2, \quad \varepsilon_{xx}^{(1)} = \alpha_1\phi_{,x} + \alpha_2 w_{,xx}, \quad \varepsilon_{xx}^{(3)} = \alpha_3\left(\phi_{,x} + w_{,xx}\right) \tag{5.24}$$

$$\gamma_{xz}^{(0)} = \alpha_1\phi + \left(\alpha_2 + 1\right)w_{,x}, \quad \gamma_{xz}^{(2)} = 3\alpha_3\left(\phi + w_{,x}\right) \tag{5.25}$$

This unified form [Eq. (5.22)] can be used to write a general finite element code that can be used to obtain results for any of the three beam theories by setting appropriate values of constants α_i $(i = 1, 2, 3)$ and K_s.

The unified beam theory presented in this study differs from the general third–order beam theory proposed by Arbind, Reddy, and Srinivasa [148] in several aspects.

1. The micro–structure dependent properties in the paper by Arbind, Reddy, and Srinivasa [148] are provided through modified couple stress theory, whereas, in this paper strain gradient theory is employed. In modified couple stress theory the nonlocal terms present in the strain energy depend on the product of the deviatoric part of the symmetric couple stress tensor and the components of the symmetric curvature tensor. Modified couple stress theory can be considered as a special case of the strain gradient theory [143, 149].

2. The generalized third–order beam theory presented by Arbind, Reddy, and Srinivasa [148] assumes a displacement field with 7 primary variables with C^0 continuity for all variables in the case where the beam is studied with no nonlocal features. When modified couple stress theory is considered, some of the primary variables will require C^1 continuity. In the unified beam theory presented in this paper, only 3 primary variables are present. However, the degree of continuity will depend on the type of the beam and it can vary for each variable between C^0, C^1, and C^2 continuity. More information is provided later in Table 5.3.

5.4 Theoretical Formulation

The principle of virtual displacements can be used to derive the governing equations and associated boundary conditions for a beam enhanced with strain gradient theory. The primary purpose of

this section is to derive the governing differential equations and boundary conditions of the unified strain gradient beam theory. The boundary conditions always appear in pairs, where one element of the pair is known as a *primary variable* (i.e., the generalized displacement) and the second element of the pair is termed a *secondary variable* (i.e., the generalized force); see Reddy [119] for details. For a non–conventional theory of the type considered herein, the nature of the primary and secondary variables is an important outcome of the principle of virtual displacements. The starting point of this development is the computation of the total virtual work done, which is the sum of the virtual strain energy stored in the body (δU) and the virtual work done by external forces (δV_E).

The mathematical expression of the principle of virtual displacements is [119]:

$$\delta W \equiv \delta U + \delta V_E = 0 \tag{5.26}$$

where δW is the total virtual work done, δU is the virtual strain energy stored in the body, and δV_E is the virtual work done by external forces, which are yet to be identified. For a one–dimensional beam element, δV_E is given by

$$\delta V_E = -\left[\int_0^L (f\delta u + q\delta w)\, dx + \sum_{i=1}^{n(\alpha_1,\alpha_2,\alpha_3)} Q_i\, \delta\Delta_i\right] \tag{5.27}$$

where the negative sign indicates that the work is expended on the structure, f and q are the distributed forces in the longitudinal and transverse directions, respectively, and (Q_i, Δ_i) are the generalized forces and displacements whose form will be identified for different beam theories (parameters α_i are used to identify various theories; see Eq. (5.22)) in the sequel; n denotes the number of primary variables. Using the definitions of Eqs. (5.7) and (5.27), one obtains

$$\begin{aligned} 0 =& \delta U + \delta V_E \\ =& \int_0^L \int_A [\sigma_{ij}\delta\varepsilon_{ij} + \tau_{ijm}\delta\varepsilon_{ij,m}]\, dA dx - \left[\int_0^L (f\delta u + q\delta w)\, dx + \sum_{i=1}^{n(\alpha_1,\alpha_2,\alpha_3)} Q_i\, \delta\Delta_i\right] \end{aligned} \tag{5.28}$$

In the following, δU is expressed in terms of the stress resultants using the displacement field of Eq. (5.22) of a unified beam:

$$\begin{aligned}
\delta U = \int_0^L \int_A \Big\{ & \sigma_{xx}\delta\varepsilon_{xx} + \sigma_{xz}\delta\gamma_{xz} \\
& + \ell_s^2 \Big\langle \sigma_{xx,x}\delta\varepsilon_{xx,x} + \sigma_{xz,x}\delta\gamma_{xz,x} + \sigma_{xx,z}\delta\varepsilon_{xx,z} + \sigma_{xz,z}\delta\gamma_{xz,z} \Big\rangle \Big\} dA dx \\
= \int_0^L \Big\{ & N_{xx}\left(\delta u_{,x} + w_{,x}\delta w_{,x}\right) + M_{xx}\left(\alpha_1\delta\phi_{,x} + \alpha_2\delta w_{,xx}\right) + \alpha_3 P_{xx}\left(\delta\phi_{,x} + \delta w_{,xx}\right) \\
& + Q_x\left(\alpha_1\delta\phi + (\alpha_2+1)\,\delta w_{,x}\right) + 3\alpha_3 R_x\left(\delta\phi + \delta w_{,x}\right) \\
& + \ell_s^2 \Big\langle N_{xx,x}\left(\delta u_{,xx} + w_{,xx}\delta w_{,x} + w_{,x}\delta w_{,xx}\right) + M_{xx,x}\left(\alpha_1\delta\phi_{,xx} + \alpha_2\delta w_{,xxx}\right) \\
& + \alpha_3 P_{xx,x}\left(\delta\phi_{,xx} + \delta w_{,xxx}\right) + Q_{x,x}\left(\alpha_1\delta\phi_{,x} + (\alpha_2+1)\,\delta w_{,xx}\right) \\
& + 3\alpha_3 R_{x,x}\left(\delta\phi_{,x} + \delta w_{,xx}\right) + \bar{N}_{xx}\left(\alpha_1\delta\phi_{,x} + \alpha_2\delta w_{,xx}\right) + 3\alpha_3\bar{S}_{xx}\left(\delta\phi_{,x} + \delta w_{,xx}\right) \\
& + 6\alpha_3\bar{T}_x\left(\delta\phi + \delta w_{,x}\right) \Big\rangle \Big\} dx
\end{aligned} \tag{5.29}$$

where the following notation have been used for the stress resultants:

$$\begin{aligned}
\langle N_{xx}, M_{xx}, P_{xx}\rangle &= \int_A \left\langle 1, z, z^3 \right\rangle \sigma_{xx}\, dA \\
\left\langle \bar{N}_{xx}, \bar{S}_{xx} \right\rangle &= \int_A \left\langle 1, z^2 \right\rangle \sigma_{xx,z}\, dA \\
\langle Q_x, R_x\rangle &= \int_A \left\langle 1, z^2 \right\rangle \sigma_{xz}\, dA \\
\bar{T}_x &= \int_A z\sigma_{xz,z}\, dA
\end{aligned} \tag{5.30}$$

By relieving δu, δw and $\delta\phi$ of differentiation, δU can be expressed as

$$\begin{aligned}
\delta U = \int_0^L \Big\{ & \Big[-N_{xx,x} + \ell_s^2 N_{xx,xxx} \Big]\delta u + \Big[-\Big(N_{xx}w_{,x}\Big)_{,x} - \bar{Q}_{x,x} + \bar{M}_{xx,xx} \\
& + \ell_s^2 \Big\langle \underline{\Big(N_{xx,x}w_{,x}\Big)_{,xx} - \Big(N_{xx,x}w_{,xx}\Big)_{,x}} + \bar{Q}_{x,xxx} + \tilde{N}_{xx,xx} - 6\alpha_3\bar{T}_{x,x} - \bar{M}_{xx,xxxx} \Big\rangle \Big]\delta w \\
& + \Big[\hat{Q}_x - \hat{M}_{xx,x} + \ell_s^2 \Big\langle 6\alpha_3\bar{T}_x - \hat{Q}_{x,xx} - \hat{N}_{xx,x} + \hat{M}_{xx,xxx} \Big\rangle \Big]\delta\phi \Big\} dx
\end{aligned}$$

$$
\begin{aligned}
&+\Big\{\Big[N_{xx}-\ell_s^2 N_{xx,xx}\Big]\delta u+\ell_s^2 N_{xx,x}\delta u_{,x}\\
&\quad+\Big[N_{xx}w_{,x}+\bar{Q}_x-\bar{M}_{xx,x}+\ell_s^2\Big\langle\underline{N_{xx,x}w_{,xx}-\Big(N_{xx,x}w_{,x}\Big)_{,x}}+6\alpha_3\bar{T}_x-\bar{Q}_{x,xx}\\
&\qquad-\tilde{N}_{xx,x}+\bar{M}_{xx,xxx}\Big\rangle\Big]\delta w\\
&\quad+\Big[\bar{M}_{xx}+\ell_s^2\Big\langle N_{xx,x}w_{,x}+\bar{Q}_{x,x}+\tilde{N}_{xx}-\bar{M}_{xx,xx}\Big\rangle\Big]\delta w_{,x}+\ell_s^2\bar{M}_{xx,x}\delta w_{,xx}\\
&\quad+\Big[\hat{M}_{xx}+\ell_s^2\Big\langle\hat{Q}_{x,x}+\hat{N}_{xx}-\hat{M}_{xx,xx}\Big\rangle\Big]\delta\phi+\ell_s^2\hat{M}_{xx,x}\delta\phi_{,x}\Big\}\Big|_0^L
\end{aligned}
\tag{5.31}
$$

where for the sake of brevity the following notation is introduced:

$$
\begin{aligned}
&\bar{M}_{xx}=\alpha_2 M_{xx}+\alpha_3 P_{xx} && \hat{M}_{xx}=\alpha_1 M_{xx}+\alpha_3 P_{xx}\\
&\bar{Q}_x=(\alpha_2+1)\,Q_x+3\alpha_3 R_x && \hat{Q}_x=\alpha_1 Q_x+3\alpha_3 R_x\\
&\tilde{N}_{xx}=\alpha_2\bar{N}_{xx}+3\alpha_3\bar{S}_{xx} && \hat{N}_{xx}=\alpha_1\bar{N}_{xx}+3\alpha_3\bar{S}_{xx}
\end{aligned}
\tag{5.32}
$$

Using the identities $\Big(N_{xx,x}w_{,x}\Big)_{,xx}-\Big(N_{xx,x}w_{,xx}\Big)_{,x}=\Big(N_{xx,xx}w_{,x}\Big)_{,x}$ and $N_{xx,x}w_{,xx}-\Big(N_{xx,x}w_{,x}\Big)_{,x}$ $=-N_{xx,xx}w_{,x}$, the underlined parts in Eq. (5.31) can further be simplified as

$$
\begin{aligned}
\delta U=\int_0^L&\Big\{\Big[-N_{xx,x}+\ell_s^2 N_{xx,xxx}\Big]\delta u\\
&\quad+\Big[-\Big(N_{xx}w_{,x}\Big)_{,x}-\bar{Q}_{x,x}+\bar{M}_{xx,xx}+\ell_s^2\Big\langle\underline{\Big(N_{xx,xx}w_{,x}\Big)_{,x}}+\bar{Q}_{x,xxx}+\tilde{N}_{xx,xx}\\
&\qquad-6\alpha_3\bar{T}_{x,x}-\bar{M}_{xx,xxxx}\Big\rangle\Big]\delta w\\
&\quad+\Big[\hat{Q}_x-\hat{M}_{xx,x}+\ell_s^2\Big\langle 6\alpha_3\bar{T}_x-\hat{Q}_{x,xx}-\hat{N}_{xx,x}+\hat{M}_{xx,xxx}\Big\rangle\Big]\delta\phi\Big\}dx\\
&+\Big\{\Big[N_{xx}-\ell_s^2 N_{xx,xx}\Big]\delta u+\ell_s^2 N_{xx,x}\delta u_{,x}\\
&\quad+\Big[N_{xx}w_{,x}+\bar{Q}_x-\bar{M}_{xx,x}+\ell_s^2\Big\langle\underline{-N_{xx,xx}w_{,x}}+6\alpha_3\bar{T}_x-\bar{Q}_{x,xx}-\tilde{N}_{xx,x}+\bar{M}_{xx,xxx}\Big\rangle\Big]\delta w\\
&\quad+\Big[\bar{M}_{xx}+\ell_s^2\Big\langle N_{xx,x}w_{,x}+\bar{Q}_{x,x}+\tilde{N}_{xx}-\bar{M}_{xx,xx}\Big\rangle\Big]\delta w_{,x}+\ell_s^2\bar{M}_{xx,x}\delta w_{,xx}\\
&\quad+\Big[\hat{M}_{xx}+\ell_s^2\Big\langle\hat{Q}_{x,x}+\hat{N}_{xx}-\hat{M}_{xx,xx}\Big\rangle\Big]\delta\phi+\ell_s^2\hat{M}_{xx,x}\delta\phi_{,x}\Big\}\Big|_0^L
\end{aligned}
\tag{5.33}
$$

By substituting Eqs. (5.27) and (5.33) into the statement of the principle of virtual displacements in Eq. (5.26), one obtains

$$
\begin{aligned}
0 = \int_0^L \Bigg\{ & \Big[- N_{xx,x} + \ell_s^2 N_{xx,xxx} - f \Big] \delta u \\
& + \Big[- \Big(N_{xx} w_{,x} \Big)_{,x} - \bar{Q}_{x,x} + \bar{M}_{xx,xx} + \ell_s^2 \Big\langle \Big(N_{xx,xx} w_{,x} \Big)_{,x} + \bar{Q}_{x,xxx} + \tilde{N}_{xx,xx} \\
& \quad - 6\alpha_3 \bar{T}_{x,x} - \bar{M}_{xx,xxxx} \Big\rangle - q \Big] \delta w \\
& + \Big[\hat{Q}_x - \hat{M}_{xx,x} + \ell_s^2 \Big\langle 6\alpha_3 \bar{T}_x - \hat{Q}_{x,xx} - \hat{N}_{xx,x} + \hat{M}_{xx,xxx} \Big\rangle \Big] \delta\phi \Bigg\} dx \\
& + \Bigg\{ \Big[N_{xx} - \ell_s^2 N_{xx,xx} \Big] \delta u + \ell_s^2 N_{xx,x} \delta u_{,x} \\
& \quad + \Big[N_{xx} w_{,x} + \bar{Q}_x - \bar{M}_{xx,x} + \ell_s^2 \Big\langle - N_{xx,xx} w_{,x} + 6\alpha_3 \bar{T}_x - \bar{Q}_{x,xx} - \tilde{N}_{xx,x} + \bar{M}_{xx,xxx} \Big\rangle \Big] \delta w \\
& \quad + \Big[\bar{M}_{xx} + \ell_s^2 \Big\langle N_{xx,x} w_{,x} + \bar{Q}_{x,x} + \tilde{N}_{xx} - \bar{M}_{xx,xx} \Big\rangle \Big] \delta w_{,x} + \ell_s^2 \bar{M}_{xx,x} \delta w_{,xx} \\
& \quad + \Big[\hat{M}_{xx} + \ell_s^2 \Big\langle \hat{Q}_{x,x} + \hat{N}_{xx} - \hat{M}_{xx,xx} \Big\rangle \Big] \delta\phi + \ell_s^2 \hat{M}_{xx,x} \delta\phi_{,x} \Bigg\} \Bigg|_0^L \\
& - \sum_{i=1}^{n(\alpha_1,\alpha_2,\alpha_3)} Q_i \, \delta\Delta_i
\end{aligned}
\tag{5.34}
$$

By setting the coefficients of δu, δw and $\delta\phi$ to zero separately, the equilibrium equations are derived. Also, the boundary terms resulting from differentiation by parts give the corresponding boundary conditions. The governing equations for a unified beam theory are:

$$
\begin{aligned}
\delta u: \quad & - N_{xx,x} + \ell_s^2 N_{xx,xxx} - f = 0 \\
\delta w: \quad & - \left(N_{xx} w_{,x} \right)_{,x} - \bar{Q}_{x,x} + \bar{M}_{xx,xx} + \ell_s^2 \Big\langle \left(N_{xx,xx} w_{,x} \right)_{,x} + \bar{Q}_{x,xxx} + \tilde{N}_{xx,xx} - 6\alpha_3 \bar{T}_{x,x} \\
& \qquad - \bar{M}_{xx,xxxx} \Big\rangle - q = 0 \\
\delta\phi: \quad & \hat{Q}_x - \hat{M}_{xx,x} + \ell_s^2 \Big\langle 6\alpha_3 \bar{T}_x - \hat{Q}_{x,xx} - \hat{N}_{xx,x} + \hat{M}_{xx,xxx} \Big\rangle = 0
\end{aligned}
\tag{5.35}
$$

The primary and secondary variables as well as the generalized force boundary conditions are identified in Table 5.2 using the boundary terms in Eq. (5.34). It is important to note that only one element of each pair can be specified at a boundary point. Thus, when a primary variable is known,

its corresponding secondary variable is unknown and can be determined in the post–computation of the finite element analysis. On the other hand, if a primary variable is not specified, the corresponding secondary variable must be known/specified.

The stress resultants of Eq. (5.30) can be expressed in terms of the generalized displacements using a constitutive equation. For an isotropic elastic homogeneous beam, the stress–displacement relations are given by (using uniaxial stress–strain relations)

$$\sigma_{xx} = E\left[u_{,x} + \frac{1}{2}w_{,x}^2 + z\left(\alpha_1\phi_{,x} + \alpha_2 w_{,xx}\right) + \alpha_3 z^3\left(\phi_{,x} + w_{,xx}\right)\right] \tag{5.36}$$

$$\sigma_{xz} = G\left[\alpha_1\phi + \left(\alpha_2 + 1\right)w_{,x} + 3\alpha_3 z^2\left(\phi + w_{,x}\right)\right] \tag{5.37}$$

Then, the resultants of Eq. (5.30) can be expressed in terms of the generalized displacements as follows:

$$\begin{aligned}
N_{xx} &= A_{xx}\left(u_{,x} + \frac{1}{2}w_{,x}^2\right)\\
M_{xx} &= D_{xx}\left(\alpha_1\phi_{,x} + \alpha_2 w_{,xx}\right) + \alpha_3 F_{xx}\left(\phi_{,x} + w_{,xx}\right)\\
P_{xx} &= F_{xx}\left(\alpha_1\phi_{,x} + \alpha_2 w_{,xx}\right) + \alpha_3 H_{xx}\left(\phi_{,x} + w_{,xx}\right)\\
\bar{N}_{xx} &= A_{xx}\left(\alpha_1\phi_{,x} + \alpha_2 w_{,xx}\right) + 3\alpha_3 D_{xx}\left(\phi_{,x} + w_{,xx}\right)\\
\bar{S}_{xx} &= D_{xx}\left(\alpha_1\phi_{,x} + \alpha_2 w_{,xx}\right) + 3\alpha_3 F_{xx}\left(\phi_{,x} + w_{,xx}\right)\\
Q_x &= K_s\left[A_{xz}\left(\alpha_1\phi + \left(\alpha_2 + 1\right)w_{,x}\right) + 3\alpha_3 D_{xz}\left(\phi + w_{,x}\right)\right]\\
R_x &= K_s\left[D_{xz}\left(\alpha_1\phi + \left(\alpha_2 + 1\right)w_{,x}\right) + 3\alpha_3 F_{xz}\left(\phi + w_{,x}\right)\right]\\
\bar{T}_x &= 6K_s\alpha_3 D_{xz}\left(\phi + w_{,x}\right)
\end{aligned} \tag{5.38}$$

where the beam elastic stiffness coefficients ($A_{xx}, D_{xx}, F_{xx}, H_{xx}, A_{xz}, D_{xz}, F_{xz}$) are defined by

$$\left\langle A_{xx}, D_{xx}, F_{xx}, H_{xx}\right\rangle = \int_A E\left\langle 1, z^2, z^4, z^6\right\rangle dA \tag{5.39}$$

$$\left\langle A_{xz}, D_{xz}, F_{xz}\right\rangle = \int_A G\left\langle 1, z^2, z^4\right\rangle dA \tag{5.40}$$

Since the beam is assumed to be homogeneous, the terms with odd powers of z do not contribute

to the stress resultants.

5.5 Finite Element Formulation

5.5.1 Weak Form

The finite element model of the beam over a typical finite element, $\Omega^e = (x_a, x_b)$, can be developed directly from the principle of virtual displacements, $\delta W = 0$, applied to a typical beam finite element (see Reddy [51, 119, 150]):

$$\begin{aligned}
0 = \int_{x_a}^{x_b} \Big\{ & N_{xx}\left(\delta u_{,x} + w_{,x}\delta w_{,x}\right) + M_{xx}\left(\alpha_1 \delta\phi_{,x} + \alpha_2 \delta w_{,xx}\right) + \alpha_3 P_{xx}\left(\delta\phi_{,x} + \delta w_{,xx}\right) \\
& + Q_x\left(\alpha_1\delta\phi + (\alpha_2+1)\,\delta w_{,x}\right) + 3\alpha_3 R_x\left(\delta\phi + \delta w_{,x}\right) + \ell_s^2 \Big\langle N_{xx,x}\left(\delta u_{,xx} + w_{,xx}\delta w_{,x}\right. \\
& \left. + w_{,x}\delta w_{,xx}\right) + M_{xx,x}\left(\alpha_1\delta\phi_{,xx} + \alpha_2\delta w_{,xxx}\right) + \alpha_3 P_{xx,x}\left(\delta\phi_{,xx} + \delta w_{,xxx}\right) + Q_{x,x}\left(\alpha_1\delta\phi_{,x}\right. \\
& \left. + (\alpha_2+1)\,\delta w_{,xx}\right) + 3\alpha_3 R_{x,x}\left(\delta\phi_{,x} + \delta w_{,xx}\right) + \bar{N}_{xx}\left(\alpha_1\delta\phi_{,x} + \alpha_2\delta w_{,xx}\right) \\
& + 3\alpha_3\bar{S}_{xx}\left(\delta\phi_{,x} + \delta w_{,xx}\right) + 6\alpha_3\bar{T}_x\left(\delta\phi + \delta w_{,x}\right) \Big\rangle - f\delta u - q\delta w \Big\} dx \\
& - \sum_{i=1}^{n(\alpha_1,\alpha_2,\alpha_3)} Q_i\,\delta\Delta_i
\end{aligned} \tag{5.41}$$

where all of the stress resultants are defined in terms of the generalized displacements in Eq. (5.38).

5.5.2 Finite Element Model

The finite element model is developed by using the following approximation functions for u, w, and ϕ. In the derivation of the finite element formulation, δu, δw, and $\delta\phi$ are replaced by ψ_i^e, θ_i^e, and φ_i^e, respectively, to obtain the ith equation of each set. Let

$$\begin{aligned}
u(x) \approx u_h^e &= \sum_{i=1}^{n_1(\alpha_1,\alpha_2,\alpha_3)} \left(\Delta_i^1\right)^e \psi_i^e(x) \\
w(x) \approx w_h^e &= \sum_{i=1}^{n_2(\alpha_1,\alpha_2,\alpha_3)} \left(\Delta_i^2\right)^e \theta_i^e(x) \\
\phi(x) \approx \phi_h^e &= \sum_{i=1}^{n_3(\alpha_1,\alpha_2,\alpha_3)} \left(\Delta_i^3\right)^e \varphi_i^e(x)
\end{aligned} \tag{5.42}$$

Table 5.2: Primary and Secondary Variables for element e with left end at $x = x_a$ and right end at $x = x_b$.

No.	Primary Variables	Secondary Variables
1	$u\|_{x=x_a} = \Delta_1^e$	$-\left[N_{xx} - \ell_s^2 N_{xx,xx}\right]_{x=x_a} = Q_1^e$
2	$u_{,x}\|_{x=x_a} = \Delta_2^e$	$-\left[\ell_s^2 N_{xx,x}\right]_{x=x_a} = Q_2^e$
3	$w\|_{x=x_a} = \Delta_3^e$	$-\left[N_{xx}w_{,x} + \bar{Q}_x - \bar{M}_{xx,x} + \ell_s^2\left\langle -N_{xx,xx}w_{,x} + 6\alpha_3\bar{T}_x - \bar{Q}_{x,xx} - \tilde{N}_{xx,x} + \bar{M}_{xx,xxx}\right\rangle\right]_{x=x_a} = Q_3^e$
4	$w_{,x}\|_{x=x_a} = \Delta_4^e$	$-\left[\bar{M}_{xx} + \ell_s^2\left\langle N_{xx,x}w_{,x} + \bar{Q}_{x,x} + \tilde{N}_{xx} - \bar{M}_{xx,xx}\right\rangle\right]_{x=x_a} = Q_4^e$
5	$w_{,xx}\|_{x=x_a} = \Delta_5^e$	$-\left[\ell_s^2\bar{M}_{xx,x}\right]_{x=x_a} = Q_5^e$
6	$\phi\|_{x=x_a} = \Delta_6^e$	$-\left[\hat{M}_{xx} + \ell_s^2\left\langle \hat{Q}_{x,x} + \hat{N}_{xx} - \hat{M}_{xx,xx}\right\rangle\right]_{x=x_a} = Q_6^e$
7	$\phi_{,x}\|_{x=x_a} = \Delta_7^e$	$-\left[\ell_s^2\hat{M}_{xx,x}\right]_{x=x_a} = Q_7^e$
8	$u\|_{x=x_b} = \Delta_8^e$	$\left[N_{xx} - \ell_s^2 N_{xx,xx}\right]_{x=x_b} = Q_8^e$
9	$u_{,x}\|_{x=x_b} = \Delta_9^e$	$\left[\ell_s^2 N_{xx,x}\right]_{x=x_b} = Q_9^e$
10	$w\|_{x=x_b} = \Delta_{10}^e$	$\left[N_{xx}w_{,x} + \bar{Q}_x - \bar{M}_{xx,x} + \ell_s^2\left\langle -N_{xx,xx}w_{,x} + 6\alpha_3\bar{T}_x - \bar{Q}_{x,xx} - \tilde{N}_{xx,x} + \bar{M}_{xx,xxx}\right\rangle\right]_{x=x_b} = Q_{10}^e$
11	$w_{,x}\|_{x=x_b} = \Delta_{11}^e$	$\left[\bar{M}_{xx} + \ell_s^2\left\langle N_{xx,x}w_{,x} + \bar{Q}_{x,x} + \tilde{N}_{xx} - \bar{M}_{xx,xx}\right\rangle\right]_{x=x_b} = Q_{11}^e$
12	$w_{,xx}\|_{x=x_b} = \Delta_{12}^e$	$\left[\ell_s^2\bar{M}_{xx,x}\right]_{x=x_b} = Q_{12}^e$
13	$\phi\|_{x=x_b} = \Delta_{13}^e$	$\left[\hat{M}_{xx} + \ell_s^2\left\langle \hat{Q}_{x,x} + \hat{N}_{xx} - \hat{M}_{xx,xx}\right\rangle\right]_{x=x_b} = Q_{13}^e$
14	$\phi_{,x}\|_{x=x_b} = \Delta_{14}^e$	$\left[\ell_s^2\hat{M}_{xx,x}\right]_{x=x_b} = Q_{14}^e$

where $\boldsymbol{\Delta}^i$ $(i = 1, 2, 3)$ are the column vectors of the nodal degrees of freedom of the generalized displacements u, w, and ϕ, respectively. The polynomial degree of the interpolation functions in Eq. (5.42), $n_i\left(\alpha_1, \alpha_2, \alpha_3\right)$, is dictated by the degree of maximum differentiation on each of the variables in the weak form of Eq. (5.41). This depends on the type of beam theory used. For example, for the Reddy beam theory with the strain gradient effect $n_1\left(\alpha_1, \alpha_2, \alpha_3\right) = 4,\ n_2\left(\alpha_1, \alpha_2, \alpha_3\right) = 6,\ n_3\left(\alpha_1, \alpha_2, \alpha_3\right) = 4$:

$$\left(\boldsymbol{\Delta}^1\right)^e = \begin{Bmatrix} u\left(x_a\right) \\ \left(\frac{\partial u}{\partial x}\right)\Big|_{x=x_a} \\ u\left(x_b\right) \\ \left(\frac{\partial u}{\partial x}\right)\Big|_{x=x_b} \end{Bmatrix}, \quad \left(\boldsymbol{\Delta}^2\right)^e = \begin{Bmatrix} w\left(x_a\right) \\ \left(\frac{\partial w}{\partial x}\right)\Big|_{x=x_a} \\ \left(\frac{\partial^2 w}{\partial x^2}\right)\Big|_{x=x_a} \\ w\left(x_b\right) \\ \left(\frac{\partial w}{\partial x}\right)\Big|_{x=x_b} \\ \left(\frac{\partial^2 w}{\partial x^2}\right)\Big|_{x=x_b} \end{Bmatrix}, \quad \left(\boldsymbol{\Delta}^3\right)^e = \begin{Bmatrix} \phi\left(x_a\right) \\ \left(\frac{\partial \phi}{\partial x}\right)\Big|_{x=x_a} \\ \phi\left(x_b\right) \\ \left(\frac{\partial \phi}{\partial x}\right)\Big|_{x=x_b} \end{Bmatrix} \tag{5.43}$$

The strain gradient theory increases the degree of differentiation on each of the displacements u, w, and ϕ as compared to conventional beam theories. Thus, for the Reddy beam theory with strain gradient effect, u and ϕ should be approximated with the Hermite cubic interpolation functions and w is approximated with Hermite quintic interpolation functions; whereas, in the conventional Reddy beam theory, u and ϕ are approximated with linear Lagrange interpolation functions and w is approximated with the Hermite cubic interpolation functions. Table 5.3 includes the degree of interpolation functions for each of the beam theories for both cases: when strain gradient effect is included and excluded. Degrees of interpolation equal to 1, 3, and 5 in Table 5.3 suggest C^0, C^1, and C^2 continuity, respectively. Note that for the Euler–Bernoulli beam theory, "N/A" suggests that the matrices $\mathbf{K}^{i3}$ and $\mathbf{K}^{3i}$, the force vector $\mathbf{f}^3$, and the displacement vector $\boldsymbol{\Delta}^3$ are not present.

Substitution of the interpolation functions from Eq. (5.42) into the weak form in Eq. (5.41) results in the following finite element model:

$$\mathbf{K}^e\boldsymbol{\Delta}^e = \mathbf{F}^e \tag{5.44}$$

Table 5.3: Required degree of interpolation functions.

Without Strain Gradient			*With Strain Gradient*		
EBT	TBT	RBT	EBT	TBT	RBT
1	1	1	3	3	3
3	1	3	5	3	5
N/A	1	1	N/A	3	3

with

$$\mathbf{K}^e = \begin{bmatrix} [\mathbf{K}^{11}]_{n_1\times n_1} & [\mathbf{K}^{12}]_{n_1\times n_2} & [\mathbf{0}]_{n_1\times n_3} \\ [\mathbf{K}^{21}]_{n_2\times n_1} & [\mathbf{K}^{22}]_{n_2\times n_2} & [\mathbf{K}^{23}]_{n_2\times n_3} \\ [\mathbf{0}]_{n_3\times n_1} & [\mathbf{K}^{32}]_{n_3\times n_2} & [\mathbf{K}^{33}]_{n_3\times n_3} \end{bmatrix}, \quad \mathbf{\Delta}^e = \begin{Bmatrix} [\mathbf{\Delta}^1]_{n_1\times 1} \\ [\mathbf{\Delta}^2]_{n_2\times 1} \\ [\mathbf{\Delta}^3]_{n_3\times 1} \end{Bmatrix},$$
$$\mathbf{F}^e = \begin{Bmatrix} [\mathbf{f}^1]_{n_1\times 1} \\ [\mathbf{f}^2]_{n_2\times 1} \\ [\mathbf{f}^3]_{n_3\times 1} \end{Bmatrix} + \mathbf{Q}^e_{(n_1+n_2+n_3)\times 1} \tag{5.45}$$

where for the sake of brevity, the superscript e (element label) has been omitted from the submatrices. The components of the stiffness matrices $K_{ij}^{\alpha\beta}$ and force vectors f_i^α for a unified beam theory with the von Kármán nonlinearity are defined as follows:

$$K_{ij}^{11} = \int_{x_a}^{x_b} \left\{ A_{xx} \left[\frac{d\psi_i^e}{dx}\frac{d\psi_j^e}{dx} + \ell_s^2 \frac{d^2\psi_i^e}{dx^2}\frac{d^2\psi_j^e}{dx^2} \right] \right\} dx$$

$$K_{ij}^{12} = \frac{1}{2}K_{ji}^{21} = \frac{1}{2}\int_{x_a}^{x_b} \left\{ A_{xx} \left[\frac{d\bar{w}}{dx}\left(\frac{d\psi_i^e}{dx}\frac{d\theta_j^e}{dx} + \ell_s^2 \frac{d^2\psi_i^e}{dx^2}\frac{d^2\theta_j^e}{dx^2} \right) + \ell_s^2 \frac{d^2\bar{w}}{dx^2}\frac{d^2\psi_i^e}{dx^2}\frac{d\theta_j^e}{dx} \right] \right\} dx$$

$$K_{ij}^{13} = K_{ji}^{31} = 0$$

$$K_{ij}^{22} = \int_{x_a}^{x_b} \left\{ \left(\frac{1}{2}A_{xx}\left(\frac{d\bar{w}}{dx}\right)^2 + K_s\left[(\alpha_2+1)^2 A_{xz} + 6\alpha_3(\alpha_2+1)D_{xz} + 9\alpha_3^2 F_{xz} \right] \right) \frac{d\theta_i^e}{dx}\frac{d\theta_j^e}{dx} \right.$$
$$+ \left(\alpha_2^2 D_{xx} + 2\alpha_2\alpha_3 F_{xx} + \alpha_3^2 H_{xx}\right)\frac{d^2\theta_i^e}{dx^2}\frac{d^2\theta_j^e}{dx^2} + \ell_s^2 \left\langle \left(A_{xx}\left(\frac{d^2\bar{w}}{dx^2}\right)^2 + 36\alpha_3^2 K_s D_{xz} \right) \right.$$
$$\times \frac{d\theta_i^e}{dx}\frac{d\theta_j^e}{dx} + \left(A_{xx}\left(\frac{d\bar{w}}{dx}\right)^2 + K_s\left[(\alpha_2+1)^2 A_{xz} + 6\alpha_3(\alpha_2+1)D_{xz} + 9\alpha_3^2 F_{xz} \right] \right.$$
$$\left. \left. + \alpha_2^2 A_{xx} + 6\alpha_2\alpha_3 D_{xx} + 9\alpha_3^2 F_{xx} \right) \frac{d^2\theta_i^e}{dx^2}\frac{d^2\theta_j^e}{dx^2} + \left(\alpha_2^2 D_{xx} + 2\alpha_2\alpha_3 F_{xx} + \alpha_3^2 H_{xx}\right) \right.$$

$$
\begin{aligned}
&\times \frac{d^3\theta_i^e}{dx^3}\frac{d^3\theta_j^e}{dx^3}\Big\rangle\Big\}\,dx \\
K_{ij}^{23} = K_{ji}^{32} = \int_{x_a}^{x_b} \Big\{ & K_s\left[\alpha_1\left(\alpha_2+1\right)A_{xz} + 3\left(\alpha_1+\alpha_2+1\right)\alpha_3 D_{xz} + 9\alpha_3^2 F_{xz}\right]\frac{d\theta_i^e}{dx}\varphi_j^e \\
&+ \left(\alpha_1\alpha_2 D_{xx} + \left(\alpha_1+\alpha_2\right)\alpha_3 F_{xx} + \alpha_3^2 H_{xx}\right)\frac{d^2\theta_i^e}{dx^2}\frac{d\varphi_j^e}{dx} + \ell_s^2\Big\langle 36\alpha_3^2 K_s D_{xz}\frac{d\theta_i^e}{dx}\varphi_j^e \\
&+ \left(K_s\left[\alpha_1\left(\alpha_2+1\right)A_{xz} + 3\left(\alpha_1+\alpha_2+1\right)\alpha_3 D_{xz} + 9\alpha_3^2 F_{xz}\right] + \alpha_1\alpha_2 A_{xx}\right. \\
&\left.+3\left(\alpha_1+\alpha_2\right)\alpha_3 D_{xx} + 9\alpha_3^2 F_{xx}\right)\frac{d^2\theta_i^e}{dx^2}\frac{d\varphi_j^e}{dx} + \left(\alpha_1\alpha_2 D_{xx} + \left(\alpha_1+\alpha_2\right)\alpha_3 F_{xx} + \alpha_3^2 H_{xx}\right) \\
&\times \frac{d^3\theta_i^e}{dx^3}\frac{d^2\varphi_j^e}{dx^2}\Big\rangle\Big\}\,dx \\
K_{ij}^{33} = \int_{x_a}^{x_b} \Big\{ & K_s\left[\alpha_1^2 K_s A_{xz} + 6\alpha_1\alpha_3 D_{xz} + 9\alpha_3^2 F_{xz}\right]\varphi_i^e\varphi_j^e + \left(\alpha_1^2 D_{xx} + 2\alpha_1\alpha_3 F_{xx} + \alpha_3^2 H_{xx}\right) \\
&\times \frac{d\varphi_i^e}{dx}\frac{d\varphi_j^e}{dx} + \ell_s^2\Big\langle 36\alpha_3^2 K_s D_{xz}\varphi_i^e\varphi_j^e + \left(K_s\left[\alpha_1^2 A_{xz} + 6\alpha_1\alpha_3 D_{xz} + 9\alpha_3^2 F_{xz}\right]\right. \\
&\left.+\alpha_1^2 A_{xx} + 6\alpha_1\alpha_3 D_{xx} + 9\alpha_3^2 F_{xx}\right)\frac{d\varphi_i^e}{dx}\frac{d\varphi_j^e}{dx} + \left(\alpha_1^2 D_{xx} + 2\alpha_1\alpha_3 F_{xx} + \alpha_3^2 H_{xx}\right) \\
&\times \frac{d^2\varphi_i^e}{dx^2}\frac{d^2\varphi_j^e}{dx^2}\Big\rangle\Big\}\,dx
\end{aligned}
\tag{5.46}
$$

$$
\begin{aligned}
f_i^1 &= \int_{x_a}^{x_b} \psi_i^e f\left(x\right)dx \\
f_i^2 &= \int_{x_a}^{x_b} \theta_i^e q\left(x\right)dx \\
f_i^3 &= 0
\end{aligned}
\tag{5.47}
$$

It is worth mentioning that the stiffness matrix for a unified beam with the von Kármán nonlinearity is not symmetric $\left(K_{ij}^{12} \neq K_{ji}^{21}\right)$. The boundary conditions, Q_i^e, are defined in Table 5.2. The nonlinearity of the problem dictates the use of an iterative method to solve for the nodal displacements. In this specific problem, the nonlinearity is only due to the transverse displacement, w. In Eq. (5.46) $\bar{w}(x)$ corresponds to the value for the transverse displacement obtained from the previous iterations.

5.5.3 Imposition of Boundary Conditions

In the previous section, the stiffness matrix and the source vector for a typical element were derived. It should be noted that if the total number of degrees of freedom in the finite element mesh

is equal to N, the number of unknowns (i.e., the number of equations) before assembly of elements will be equal to $2N$ (N primary plus N secondary degrees of freedom). The number of unknowns is decreased to N by assembly of the elements and imposition of the boundary conditions. The final assembled set of equations will be of the following form:

$$\mathbf{K}(\boldsymbol{\Delta})\,\boldsymbol{\Delta} = \mathbf{F} = \mathbf{Q} + \mathbf{f} \tag{5.48}$$

The number of boundary conditions for various beam theories, with and without the strain gradient effect, are tabulated in Table 5.4, which are determined by use of Table 5.2.

Table 5.4: Number of boundary conditions at each node for various beam theories.

	EBT	TBT	RBT
Without Strain Gradient	3	3	4
With Strain Gradient	5	6	7

Higher–order theories (such as the Reddy third–order beam theory) and the strain gradient theories introduce higher–order primary and secondary variables which do not have simple physical meanings as the ones in the EBT and TBT with no strain gradient effect. Since the physical meaning of higher order boundary terms is not known, in this study the corresponding natural boundary conditions (secondary variables) of higher order terms are set to zero at the boundaries. As mentioned earlier due to the duality between secondary and primary variables at each node, only one element of each pair can be specified. For example, in the case of a fixed support (clamped end) the primary variables $u,\ w$, and $\frac{dw}{dx}$ for the EBT (and $u,\ w$, and ϕ for the TBT and RBT) are set to zero, and in the remaining pairs (if any, depending on the beam theory and whether or not strain gradient effect is included) the secondary variables are set to zero or a specified value. For a pinned support u, and w are set to zero for all beam theories.

5.5.4 Newton's Iterative Scheme

An iterative scheme should be used to solve the set of nonlinear algebraic equations in Eq. (5.48). Newton's iterative scheme is chosen here (see Reddy [150]). Using this scheme incremental solution is derived at each iteration.

$$\delta\boldsymbol{\Delta}^{(r)} = -\left[\mathbf{T}^{e}\left(\boldsymbol{\Delta}^{(r-1)}\right)\right]^{-1}\mathbf{R}^{e}\left(\boldsymbol{\Delta}^{(r-1)}\right) \tag{5.49}$$

with the tangent matrix, $\mathbf{T}$ defined in the following:

$$\begin{aligned}
\mathbf{T}\left(\boldsymbol{\Delta}^{(r)}\right) &= \left[\frac{\partial \mathbf{R}^{(r)}}{\partial \boldsymbol{\Delta}^{(r)}}\right] \\
\mathbf{R}^{(r)} &= \mathbf{K}\left(\boldsymbol{\Delta}^{(r)}\right)\boldsymbol{\Delta}^{(r)} - \mathbf{F}^{(r)} \\
\mathbf{T}\left(\boldsymbol{\Delta}^{(r)}\right) &= \frac{\partial \mathbf{K}^{(r)}}{\partial \boldsymbol{\Delta}^{(r)}}\boldsymbol{\Delta}^{(r)} + \mathbf{K}^{(r)} - \frac{\partial \mathbf{F}^{(r)}}{\partial \boldsymbol{\Delta}^{(r)}}
\end{aligned} \tag{5.50}$$

where $\mathbf{K}^{(r)} = \mathbf{K}\left(\boldsymbol{\Delta}^{(r)}\right)$, r represents the results of the r^{th} iteration, and $\mathbf{R}$ is the global residual vector. The total solution at the end of each iteration is obtained from the following equation:

$$\boldsymbol{\Delta}^{(r)} = \boldsymbol{\Delta}^{(r-1)} + \delta\boldsymbol{\Delta}^{(r)} \tag{5.51}$$

At the end of each iteration the following convergence criterion is checked:

$$\sqrt{\frac{\delta\boldsymbol{\Delta}^{(r)} \cdot \delta\boldsymbol{\Delta}^{(r)}}{\boldsymbol{\Delta}^{(r)} \cdot \boldsymbol{\Delta}^{(r)}}} \leq \epsilon \tag{5.52}$$

where ϵ denotes a specified value of the error tolerance. The iteration process continues until convergence is achieved.

The tangent matrix of a strain gradient unified beam theory with the von Kármán nonlinearity is derived next. The submatrices of the tangent matrix $\mathbf{T}$ are determined individually using the following definitions:

$$
\begin{aligned}
R_i^\alpha =& \sum_{m=1}^{n_1(\alpha_1,\alpha_2,\alpha_3)} K_{im}^{\alpha 1}\Delta_m^1 + \sum_{n=1}^{n_2(\alpha_1,\alpha_2,\alpha_3)} K_{in}^{\alpha 2}\Delta_n^2 + \sum_{p=1}^{n_3(\alpha_1,\alpha_2,\alpha_3)} K_{ip}^{\alpha 3}\Delta_p^3 - F_i^\alpha \\
T_{ij}^{\alpha\beta} =& \frac{\partial R_i^\alpha}{\partial \Delta_j^\beta} = \sum_{m=1}^{n_1(\alpha_1,\alpha_2,\alpha_3)} \frac{\partial K_{im}^{\alpha 1}}{\partial \Delta_j^\beta}\Delta_m^1 + \sum_{n=1}^{n_2(\alpha_1,\alpha_2,\alpha_3)} \frac{\partial K_{in}^{\alpha 2}}{\partial \Delta_j^\beta}\Delta_n^2 + \sum_{p=1}^{n_3(\alpha_1,\alpha_2,\alpha_3)} \frac{\partial K_{ip}^{\alpha 3}}{\partial \Delta_j^\beta}\Delta_p^3 \\
& + K_{ij}^{\alpha\beta} - \frac{\partial F_i^\alpha}{\partial \Delta_j^\beta} \qquad\qquad \alpha,\beta = 1,2,3
\end{aligned} \tag{5.53}
$$

Note that α as the superscript is a variable different from the degree of interpolation functions $(\alpha_1, \alpha_2, \alpha_3)$. Since $\mathbf{F}$ does not depend on the primary variables, the last term $\left(\frac{\partial F_i^\alpha}{\partial \Delta_j^\beta}\right)$ vanishes. Since the nonlinearity of the equations is only due to the primary variable w, we have

$$
\frac{\partial K_{im}^{\alpha\gamma}}{\partial \Delta_j^1} = \frac{\partial K_{im}^{\alpha\gamma}}{\partial \Delta_j^3} = 0 \qquad\qquad \alpha,\gamma = 1,2,3 \tag{5.54}
$$

Consequently, we have

$$
T_{ij}^{\alpha 1} = K_{ij}^{\alpha 1}, \qquad T_{ij}^{\alpha 3} = K_{ij}^{\alpha 3} \tag{5.55}
$$

In addition, the following relations are useful in the determination of $T_{ij}^{\alpha 2}$:

$$
\frac{\partial K_{im}^{11}}{\partial \Delta_j^2} = \frac{\partial K_{im}^{31}}{\partial \Delta_j^2} = \frac{\partial K_{in}^{32}}{\partial \Delta_j^2} = \frac{\partial K_{ip}^{13}}{\partial \Delta_j^2} = \frac{\partial K_{ip}^{23}}{\partial \Delta_j^2} = \frac{\partial K_{ip}^{33}}{\partial \Delta_j^2} = 0 \tag{5.56}
$$

The $T_{ij}^{\alpha 2}$ are derived to be

$$
\begin{aligned}
T_{ij}^{12} =& 2K_{ij}^{12} = K_{ji}^{21} = T_{ji}^{21} \\
T_{ij}^{22} =& K_{ij}^{22} + \int_{x_a}^{x_b} \left\{ A_{xx} \left[\left(\frac{d\bar{u}}{dx} + \left(\frac{d\bar{w}}{dx}\right)^2 \right) \frac{d\theta_i^e}{dx}\frac{d\theta_j^e}{dx} \right.\right. \\
& \left.\left. + \ell_s^2 \left(\frac{d^2\bar{u}}{dx^2} + 2\frac{d\bar{w}}{dx}\frac{d^2\bar{w}}{dx^2} \right) \left(\frac{d^2\theta_i^e}{dx^2}\frac{d\theta_j^e}{dx} + \frac{d\theta_i^e}{dx}\frac{d^2\theta_j^e}{dx^2} \right) \right] \right\} dx \\
T_{ij}^{32} =& K_{ij}^{32}
\end{aligned} \tag{5.57}
$$

where barred displacement components ($\bar{u}$, $\bar{w}$) correspond to the functions interpolated using the nodal values from immediate previous iteration. Although the stiffness matrix was not symmetric, the resulting tangent matrix is symmetric for a strain gradient unified beam with the von Kármán nonlinearity.

5.5.5 Hermite Quintic Interpolation Functions

From the list of primary variables one can realize that for strain gradient beams, Hermite cubic polynomials should be used for u and ϕ (where applicable, e.g., TBT and RBT), whereas w is approximated by either the Hermite cubic polynomials (TBT) or higher order polynomials (EBT and RBT). The process of constructing the required higher–order polynomial is described in [119]. Since in the case of transverse displacement of strain gradient EBT and RBT elements there exists 6 parameters in each element (3 at each node), a polynomial of fifth degree (Hermite quintic) should be used.

$$w\left(x\right) \simeq w_h^e\left(\bar{x}\right) = c_1^e + c_2^e\bar{x} + c_3^e\bar{x}^2 + c_4^e\bar{x}^3 + c_5^e\bar{x}^4 + c_6^e\bar{x}^5 \tag{5.58}$$

where, $\bar{x}$ is the local coordinate ($\bar{x} = x - x_e$ with x_e being the coordinate of the first node of the element).

Coefficients c_i^e are determined in terms of the nodal values of the primary variables. Note that h_e is the length of the element e and the superscript 2 corresponds to the notation used in Eq. (5.45). We have

$$\begin{aligned}
\left(\Delta_1^2\right)^e &= w_h^e(0), \quad \left(\Delta_2^2\right)^e = \left.\frac{dw_h^e}{dx}\right|_{\bar{x}=0}, \quad \left(\Delta_3^2\right)^e = \left.\frac{d^2w_h^e}{dx^2}\right|_{\bar{x}=0} \\
\left(\Delta_4^2\right)^e &= w_h^e(h_e), \quad \left(\Delta_5^2\right)^e = \left.\frac{dw_h^e}{dx}\right|_{\bar{x}=h_e}, \quad \left(\Delta_6^2\right)^e = \left.\frac{d^2w_h^e}{dx^2}\right|_{\bar{x}=h_e}
\end{aligned} \tag{5.59}$$

The above equations can be written in matrix form as follows:

$$\begin{bmatrix} 1 & 0 & 0 & 0 & 0 & 0 \\ 0 & 1 & 0 & 0 & 0 & 0 \\ 0 & 0 & 2 & 0 & 0 & 0 \\ 1 & h_e & h_e^2 & h_e^3 & h_e^4 & h_e^5 \\ 0 & 1 & 2h_e & 3h_e^2 & 4h_e^3 & 5h_e^4 \\ 0 & 0 & 2 & 6h_e & 12h_e^2 & 20h_e^3 \end{bmatrix} \begin{Bmatrix} c_1^e \\ c_2^e \\ c_3^e \\ c_4^e \\ c_5^e \\ c_6^e \end{Bmatrix} = \begin{Bmatrix} \left(\Delta_1^2\right)^e \\ \left(\Delta_2^2\right)^e \\ \left(\Delta_3^2\right)^e \\ \left(\Delta_4^2\right)^e \\ \left(\Delta_5^2\right)^e \\ \left(\Delta_6^2\right)^e \end{Bmatrix} \tag{5.60}$$

By inverting Eq. (5.60) and substituting it into Eq. (5.58), one can rewrite Eq. (5.58) in terms of the interpolation functions θ_i^e and the primary variables:

$$w(x) \simeq w_h^e(\bar{x}) = \sum_{i=1}^{6} \theta_i^e(\bar{x}) \left(\Delta_i^2\right)^e \tag{5.61}$$

where,

$$\begin{aligned} \theta_1^e(\bar{x}) &= \left(1 - \frac{\bar{x}}{h_e}\right)^3 \left(1 + 3\frac{\bar{x}}{h_e} + 6\left(\frac{\bar{x}}{h_e}\right)^2\right) \\ \theta_2^e(\bar{x}) &= \bar{x}\left(1 - \frac{\bar{x}}{h_e}\right)^3 \left(1 + 3\frac{\bar{x}}{h_e}\right) \\ \theta_3^e(\bar{x}) &= \frac{1}{2}\bar{x}^2\left(1 - \frac{\bar{x}}{h_e}\right)^3 \\ \theta_4^e(\bar{x}) &= 1 - \left(1 - \frac{\bar{x}}{h_e}\right)^3 \left(1 + 3\frac{\bar{x}}{h_e} + 6\left(\frac{\bar{x}}{h_e}\right)^2\right) \\ \theta_5^e(\bar{x}) &= -\bar{x}\left(\frac{\bar{x}}{h_e}\right)^2 \left(4 - 7\frac{\bar{x}}{h_e} + 3\left(\frac{\bar{x}}{h_e}\right)^2\right) \\ \theta_6^e(\bar{x}) &= \frac{1}{2}\bar{x}^2\frac{\bar{x}}{h_e}\left(1 - \frac{\bar{x}}{h_e}\right)^2 \end{aligned} \tag{5.62}$$

The interpolations belong to the Hermite family because at each node w and two of its derivatives are defined ($\frac{dw}{dx}$ and $\frac{d^2w}{dx^2}$). Note that the interpolation functions satisfy the following conditions:

$$\theta_1^e(0) = 1, \qquad \theta_i^e(0) = 1 \qquad (i \neq 1)$$

$$
\begin{aligned}
&\theta_4^e\left(h_e\right)=1, && \theta_i^e\left(h_e\right)=1 && (i\neq 4)\\
&\left.\frac{d\theta_2^e}{dx}\right|_{\bar{x}=0}=1, && \left.\frac{d\theta_i^e}{dx}\right|_{\bar{x}=0}=0 && (i\neq 2)\\
&\left.\frac{d\theta_5^e}{dx}\right|_{\bar{x}=h_e}=1, && \left.\frac{d\theta_i^e}{dx}\right|_{\bar{x}=h_e}=0 && (i\neq 5)\\
&\left.\frac{d^2\theta_3^e}{dx^2}\right|_{\bar{x}=0}=1, && \left.\frac{d^2\theta_i^e}{dx^2}\right|_{\bar{x}=0}=0 && (i\neq 3)\\
&\left.\frac{d^2\theta_6^e}{dx^2}\right|_{\bar{x}=h_e}=1, && \left.\frac{d^2\theta_i^e}{dx^2}\right|_{\bar{x}=h_e}=0 && (i\neq 6)
\end{aligned}
\tag{5.63}
$$

Hermite quintic interpolation functions are plotted in Figure 5.1.

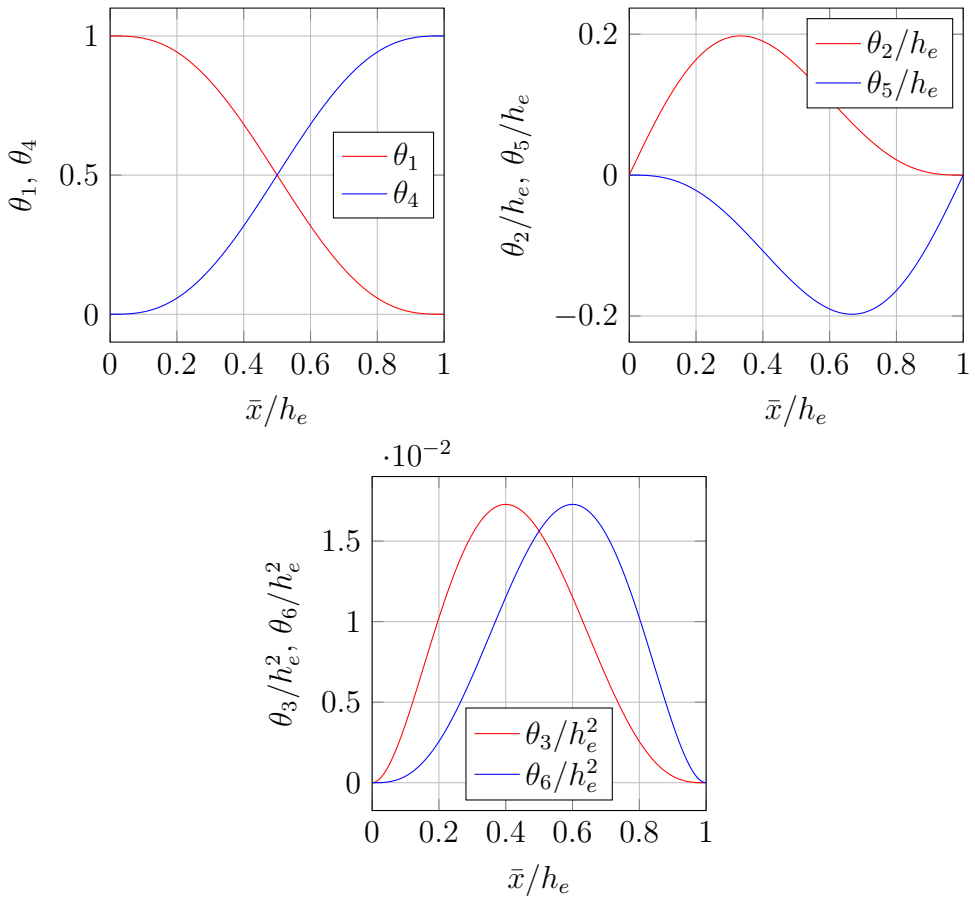

Figure 5.1: Hermite quintic interpolation functions.

The interpolation functions can also be written in terms of the local coordinate $\xi = \frac{2\bar{x}}{h_e} - 1$, which is more useful in code development:

$$\begin{aligned}
\theta_1^e(\xi) &= \frac{1}{16}(1-\xi)^3\left(8+9\xi+3\xi^2\right) \\
\theta_2^e(\xi) &= \frac{h_e}{32}(1-\xi)^3(1+\xi)(5+3\xi) \\
\theta_3^e(\xi) &= \frac{h_e^2}{64}(1-\xi)^3(1+\xi)^2 \\
\theta_4^e(\xi) &= \frac{1}{16}(1+\xi)^3\left(8-9\xi+3\xi^2\right) \\
\theta_5^e(\xi) &= -\frac{h_e}{32}(1+\xi)^3(1-\xi)(5-3\xi) \\
\theta_6^e(\xi) &= \frac{h_e^2}{64}(1+\xi)^3(1-\xi)^2
\end{aligned} \tag{5.64}$$

5.6 Numerical Results and Discussion

Numerical examples have been selected to demonstrate the individual influence of each of the factors on the response and compare with the combined effect of all factors. The transverse displacements are normalized to eliminate the effect of other parameters (such as length of the beam, elastic modulus, and so on) as follows:

$$\hat{w} = \frac{wEh^3}{L^4} \tag{5.65}$$

where w is the transverse deflection, E is the elastic modulus, h is the height of the beam, and L is the length of the beam.

The following results have been provided in the subsequent subsections:

- Linear transverse deflections for a clamped–clamped beam according to the Euler–Bernoulli and third–order Reddy beam theories with no strain gradient effect (to study the effect of shear deformation).

- Linear transverse deflections for a clamped–clamped beam using the Reddy third–order beam theory with strain gradient effect (to study the effect of strain gradient terms on the response).

- Nonlinear transverse deflections for a clamped–clamped beam using the Euler–Bernoulli and Timoshenko beam theories with no strain gradient effect (to study the effect of the von Kármán nonlinearity).

- Nonlinear transverse deflections for a clamped–clamped beam using the Reddy third–order beam theory with strain gradient terms (to study the combined effect of the von Kármán nonlinearity and strain gradient effect on shear deformable beams).

- Nonlinear transverse deflections for the Reddy third–order beam theory with the strain gradient effect for different boundary conditions (to study how the results vary for different boundary conditions).

The results correspond to a homogeneous beam with Poisson's ratio of $\nu = 0.3$ and subjected to a uniform transverse load of intensity q_0. The Timoshenko beam element with reduced integration has been implemented to avoid shear locking. Reduced integration Timoshenko beam element does not give exact results for nodal displacements even for linear problems, unless a sufficiently large number of elements are employed. Also, in the case of the von Kármán nonlinearity, nonlinear terms in the stiffness matrix are evaluated using reduced integration to avoid membrane locking. For additional discussion on these two types of locking, consult the book by Reddy [150].

5.6.1 Linear Response with No Strain Gradient Effect

Transverse deflections for a clamped–clamped beam with no strain gradient is studied using the Euler–Bernoulli beam theory (EBT) and the Reddy third–order beam theory (RBT). For the EBT, the dimensionless deflection is independent of the aspect ratio, L/h of the beam. For the RBT, 4 aspect ratios have been chosen to study the effect of thickness on the deflection of the beam. Dimensionless transverse deflections are shown in Figure 5.2. Accounting for the shear deformation makes the beam more flexible, increasing the transverse deflection (i.e., the dimensionless deflections predicted by the TBT and RBT are higher than that predicted by the EBT). This increase is significant for thick beams (smaller values of L/h, say 10) for which the effect of shear deformation is more significant. For larger values of L/h (thin beams) shear deformation

becomes negligible and the transverse deflections predicted by the TBT and RBT get close to those of the EBT.

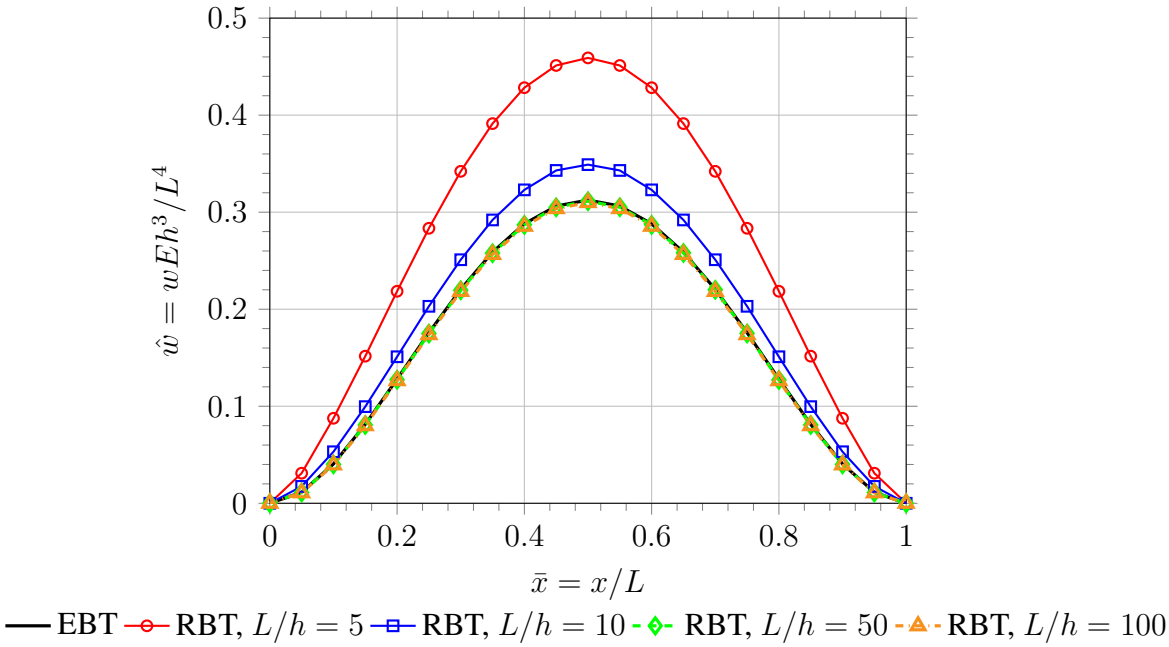

Figure 5.2: Normalized linear transverse displacements computed using the EBT and RBT for a clamped–clamped beam with different L/h ratios ($q_0 = 10$, $\nu = 0.3$).

5.6.2 Linear Response with Strain Gradient

Strain gradient theories are known to have stiffening effect on the structure. Therefore, accounting for strain gradients should result in a decrease in the displacements. Normalized linear transverse deflections for the Reddy third–order beam theory for clamped–clamped boundary conditions and for different values of the aspect ratio (L/h) and for two values of length scale parameter ($\ell_s/L = 0.1\%$ and 1.0%) are brought in Figure 5.3. The following observations can be made from the results presented in Figure 5.3:

- The transverse deflections predicted by the unified beam theory with the strain gradient effect are smaller than those of the unified beam theory without the strain gradient terms.

- Increasing the length scale parameter (ℓ_s) results in further reduction of the displacements (increased stiffening effect).

- The effect of strain gradient theory is more prominent for thin beams (higher L/h) than for thick beams (i.e., beams with smaller L/h).

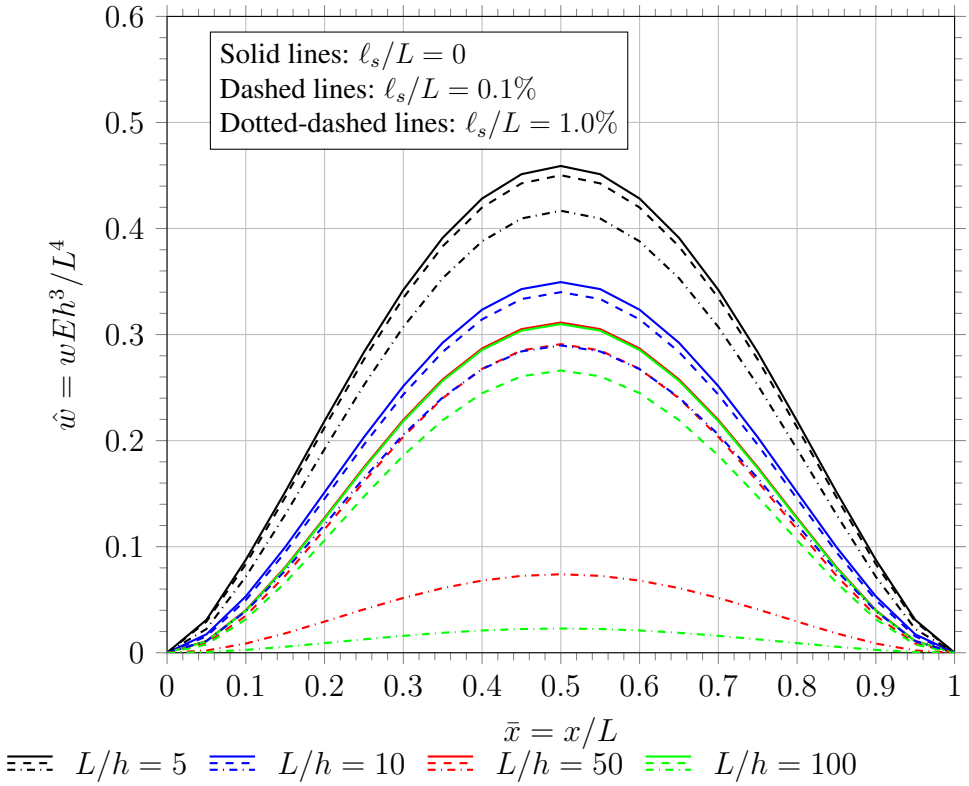

Figure 5.3: Normalized linear transverse displacements computed using the RBT for a clamped –clamped beam with different L/h ratios; without and with strain gradient effect ($q_0 = 10$, $\nu = 0.3$, $\ell_s/L = 0.0, 0.1\%$ and 1.0%).

The dimensionless transverse deflections predicted by the classical EBT are independent of the aspect ratio of the beam (L/h). However, this is not true for the EBT with the strain gradient effect, where thinner beams are influenced more (higher reduction in transverse displacement) as

compared to thick beams. This is due to the fact that for thinner beam the thickness becomes comparable to the length scale parameter.

5.6.3 Nonlinear Response with No Strain Gradient

The von Kármán nonlinearity (small strains and moderately large rotations) makes the systems stiffer compared to the corresponding linear system. Plots of dimensionless nonlinear maximum transverse deflections ($\hat{w}\left(L/2\right)$) predicted by the EBT and TBT versus the intensity of the distributed transverse load for clamped–clamped beams are shown in Figure 5.4. The results are presented for several values of the length–to–height ratio, L/h. The following observations can be made from Figure 5.4:

- Nonlinear transverse deflections are generally smaller than the linear transverse deflections.
- The effect of nonlinearity is more significant on thinner beams (larger L/h ratios). The reason is that thick beams have larger stiffness and consequently smaller deflections. Therefore, the effect of geometric nonlinearity on thick beams is less prominent. The trend is similar to the effect of strain gradient theory of beams with high or low L/h ratios.
- For very thick beams ($L/h < 20$ inFigure 5.4) the effect of nonlinearity is not significant; that is linear and nonlinear responses coincide to a good degree.
- Nonlinearity is dependent upon the intensity of the transverse distributed load, q_0. Increase in q_0 triggers higher axial force (N_{xx}) and higher nonlinear contribution to the stiffness, and thus more reduction in transverse deflections as compared to linear deflections.

5.6.4 Nonlinear Response with Strain Gradient Effect

The results for strain gradient beams with the von Kármán nonlinearity and clamped–clamped boundary conditions are studied next. The Reddy third–order beam theory is chosen with 4 different values of the length–to–height ratio, L/h. The results are graphically presented in figure 5.5. The figure includes linear and nonlinear results with no strain gradient ($\ell_s/L = 0$), and nonlinear strain gradient deflections with two distinct values of the material length scale. In figure 5.5, the

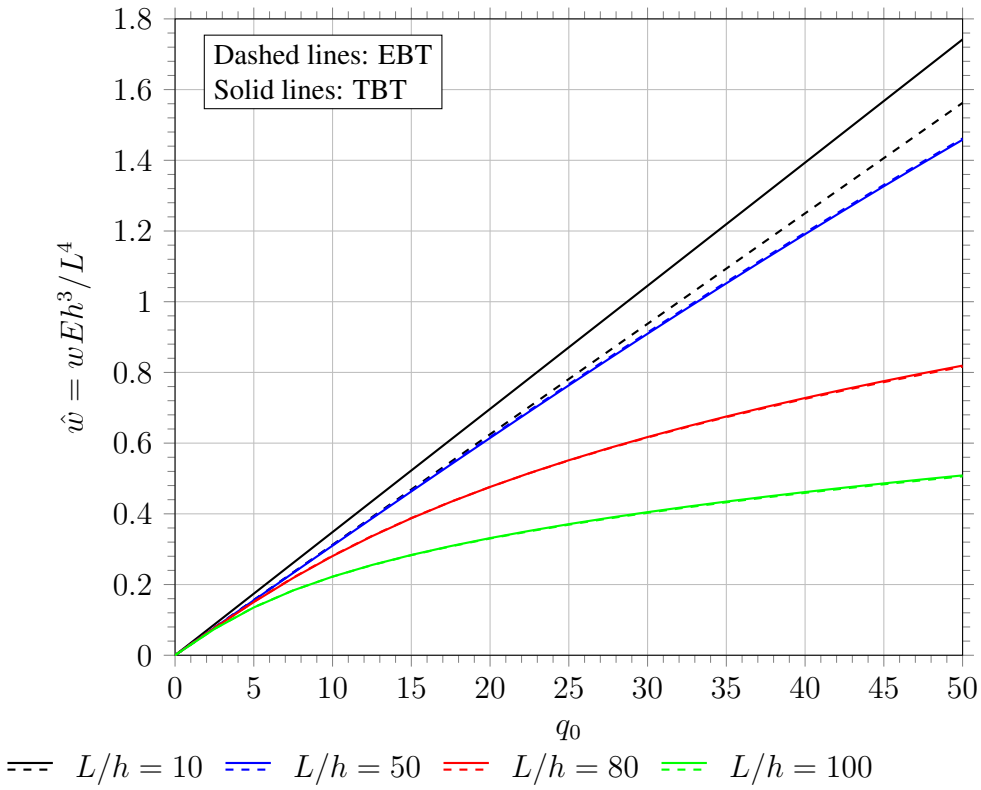

Figure 5.4: Dimensionless nonlinear maximum transverse displacement ($\bar{w}\,(L/2)$) predicted by the EBT and TBT for clamped–clamped beams for different L/h ratios and varying transverse distributed load ($\nu = 0.3$).

linear deflections for higher values of L/h (> 50 in figure 5.5) coincide. For small values of the length scale parameter ℓ_s, the effect of nonlinearity on reducing the transverse deflections is more prominent than the gradient elasticity theory. However, as ℓ_s increases, the reduction in transverse deflection due to the gradient elasticity effect becomes more apparent. For $\ell_s/L = 1.0\%$ one can see that the beam becomes extremely stiff and the effect of the von Kármán nonlinearity becomes insignificant (the relationship between the transverse deflection and the load is almost linear).

5.6.5 Different Boundary Conditions

Finally, the results for a strain gradient Reddy beam theory with von Kármán nonlinearity for two different boundary conditions (pinned–pinned beam and cantilever beam) are studied. The maximum transverse deflections for pinned–pinned beam and cantilever beam are brought

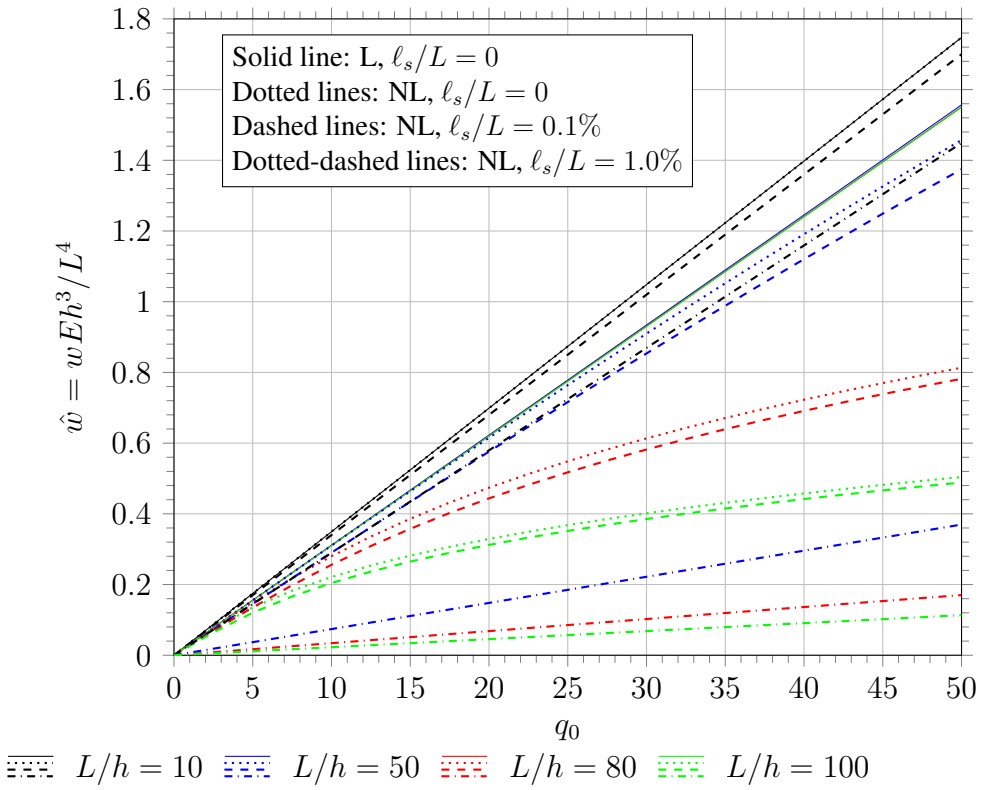

Figure 5.5: Dimensionless linear and nonlinear transverse displacements ($\hat{w}\,(L/2)$) for a clamped –clamped RBT for different L/h ratios, with and without strain gradient ($\ell_s/L = 0,\ 0.1\%$, and 1.0%), $\nu = 0.3$. L and NL correspond to linear and nonlinear results, respectively.

in figure 5.6 and figure 5.7, respectively. Comparison of figure 5.6 with figure 5.5 shows that the deflections of a pinned–pinned beam are larger compared to the clamped–clamped beam, and consequently the effect of strain gradient theory on the reduction of the transverse deflection is slightly higher. Other than this, the same trend exists for both boundary conditions. A cantilever beam (figure 5.7) experiences significantly higher transverse bending deflections. Therefore, the maximum value of the horizontal axis offigure 5.7 is different from the previous figures. One can see that for a cantilever beam the amount of bending deflection dominates the total transverse deflection, therefore, the linear displacements for all aspect ratios of the beam coincide to a good degree. Similar to the previous examples, the effect of nonlinearity is more apparent for beams with no strain gradient effect. As the length scale parameter increases, the beam becomes stiff to

the point that it almost acts linearly.

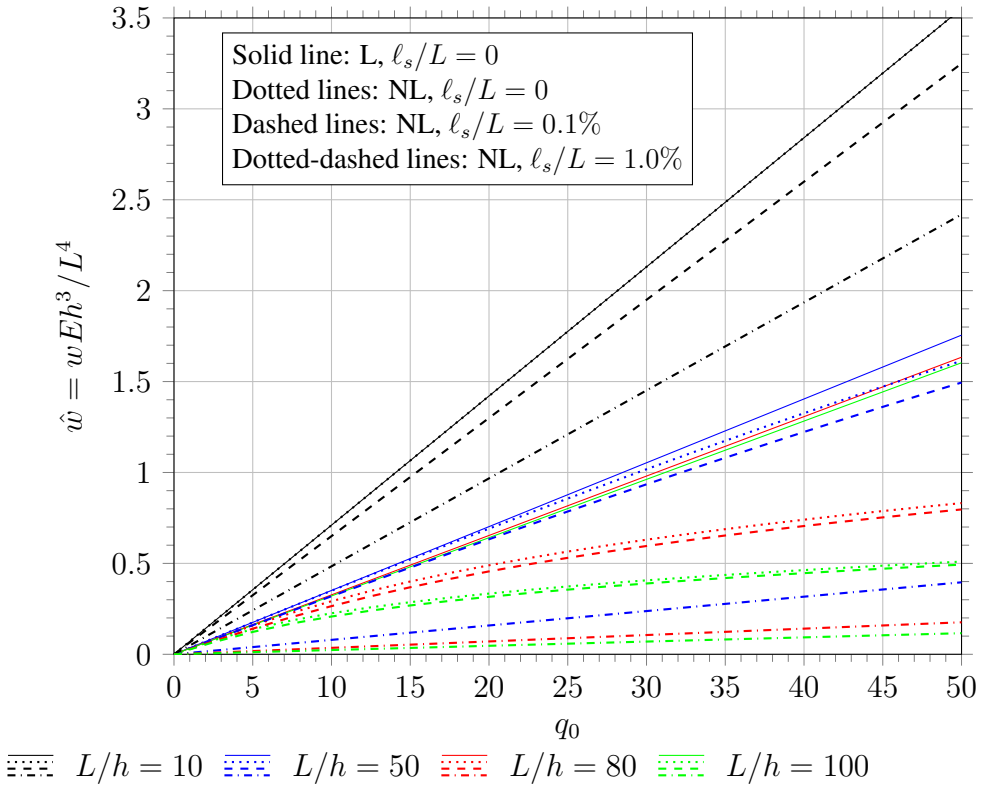

Figure 5.6: Dimensionless linear and nonlinear transverse deflections ($\hat{w}\,(L/2)$) predicted by the RBT for pinned–pinned beams with different L/h ratios, with and without strain gradient effect ($\nu = 0.3$).

5.7 Chapter Summary and Conclusions

In this study a unified beam theory accounting for both strain gradient effect and the von Kármán nonlinearity is formulated and its displacement finite element model is developed. The unified beam theory accounts for micro–structure dependent effects through classical strain gradient theory. Classical strain gradient theory introduces only one material length scale, ℓ_s. The Euler–Bernoulli, the Timoshenko, and the Reddy third–order beam theories are all special cases of the unified beam theory.

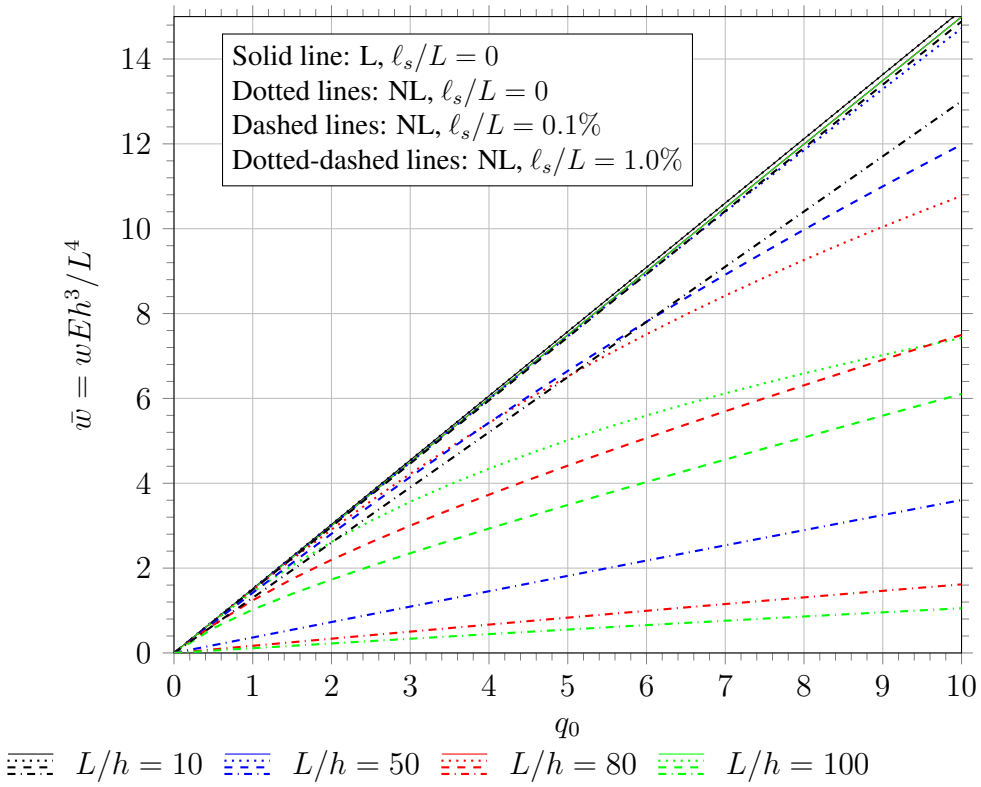

Figure 5.7: Dimensionless linear and nonlinear transverse deflections ($\hat{w}\,(L/2)$) predicted by the RBT for cantilever beams for different L/h ratios, with and without strain gradient ($\nu = 0.3$).

Numerical examples are provided to investigate the effect of nonlinearity and strain gradient terms on the response of different beam theories. The results show that, in general, both the von Kármán nonlinearity and strain gradient effect make the beam stiffer, and consequently reduce the transverse deflections. Due to the fact that thicker beams have higher stiffness as compared to thinner beams, the stiffening effect and nonlinearity are more prominent for thin beams in both cases. An increase in the material length scale parameter, ℓ_s, also makes the beam stiffer. When ℓ_s is increased beyond a point, the beam becomes so stiff that its response is linear.

The unified beam theory can be employed in finite element software to model different beam theories accounting for both the size effect and geometric nonlinearity using one unified formulation. The idea presented in this study can be extended to the study of composite beams, functionally graded beams, and plates.

6. SUMMARY AND CONCLUSIONS

In Chapter 2 a new computational framework for the study of fracture in brittle solids, Graph-based Finite Element Appraoch (GraFEA), is introduced. The two key features of GraFEA are: 1. the network representation of the conventional FEM, and 2. the imposition of discrete edge-based fracture criterion. The network representation of GraFEA moves the focus from the elements (as in conventional FEM) to the edges. The above-mentioned two features allow us to take advantage of the strength of the conventional FEM while making use of edge failure for the study of fracture (similar to bond-breakage models), therefore circumventing the need to deal with the issues of material separation which is common in continuum-based approaches to fracture.

The network representation of GraFEA is capable of handling crack initiation, crack branching, and multiple cracks growing at the same time. These aspects makes GraFEA a suitable computational method for the study of fracture in quasi-brittle materials (such as laminated glass, concrete, etc.). In these type of materials several cracks form simultaneously, resulting in a shattered sample where the size of the small pieces is more or less of the same order. This phenomenon cannot be captured using XFEM or cohesive zone models (which at most can consider only a few number of cracks emanating in the body), or CDM (which considers a diffuse damage assuming several microcracks are spread out over the continuum). However, the network representation of GraFEA is capable of studying such phenomenon, and the introduction of the nonlocal fracture criterion will also introduce a length scale which can account for the sizes of the broken pieces.

The fact that GraFEA builds upon conventional FEM (through the addition of an edge-based damage variable) is one of the points of strength of this method. GraFEA converts to conventional FEM in the case of no damage. Since FEM is the most widely used computational method in the field of solid mechanics, the ability to study fracture using FEM is a significant contribution.

In Chapter 3 the local fracture criterion of Chapter 2 is upgraded to a physically motivated nonlocal fracture criterion. It is shown that the nonlocal fracture criterion eliminates the mesh dependency caused by fracture localization. The mesh dependency studies are performed using a

hierarchical mesh refinement procedure, and the comparisons for different levels of refinement are based upon the global force-displacement relationship. With the local fracture criterion, the peak force at fracture initiation continues to decrease with further mesh refinement. However, for the nonlocal fracture criterion the global responses are shown to be similar.

The length scale parameter, ℓ_c, introduced in the nonlocal fracture criterion will also affect the fracture pattern. By increasing the magnitude of the ℓ_c, the damage pattern moves from a localized fracture to a diffuse damage with complete separation along a certain plane. For a given ℓ_c, differences can be observed for the diffuse part of the damage pattern for different mesh densities, however, it is shown in Chapter 3 that the influence of these variations on the global response is negligible.

In Chapter 4 a unified integro-differential nonlocal model is introduced based on the two-phase Eringen nonlocal model. The proposed model is a linear combination of a local and integral-type nonlocal constitutive models. The kernel function used in the integral part is chosen different from the one resulting in the differential form of Eringen nonlocal model, and it is shown that the kernel function chosen in this study resolves the paradox reported in the literature with regard to the cantilever beams. The differential form of Eringen nonlocal model, which has widely been used in the literature, is incapable of capturing size dependent effects for a cantilever beam. When considering size dependent effects, cantilever beams are an important class of beams because of their wide use as micro/nano actuators and sensors. The model introduced in this study is capable of capturing the softening effect of Eringen nonlocal model (with increasing length scale parameter) for cantilever beams as well as other beams.

In Chapter 5 the influence of including strain gradient effect and von Kármán nonlinearity on the response of familiar beam theories (Euler-Bernoulli beam, Timoshenko beam, Reddy third-order beam) are studied through derivation of displacement-based finite element models. It is shown that both the strain gradient effect and the von Kármán nonlinearity will have a stiffening effect on the beams with a more significant influence on the response of thinner beams.

The findings of Chapter 4 and Chapter 5 were used when choosing the remedy for the mesh

dependency of GraFEA (Chapter 3). Due to the ease of implementation of an integral-type nonlocality (not requiring additional boundary conditions as in the case of gradient theories) and its ability to resolve mesh sensitivity, a nonlocality of the integral form is chosen.

6.1 Future Studies

In this study all of the numerical results on GraFEA are derived using a quasi-static analysis for brittle materials. Although these results are informative, they are reliable up to the point of fracture initiation (peak force in the force-displacement relationship). As soon as a crack is formed in a brittle material, it propagates in a dynamic manner. Dynamic analysis will automatically resolve the issue with the singularity in the stiffness matrix when all of the edges connected to one node are broken (an isolated node). These nodes will serve as the flyaway pieces of a shattered medium in the dynamic analysis.

The nonlocal fracture criterion used in GraFEA (Chapter 3) introduces a length scale parameter into the problem. Studies should be carried out to justify the results from GraFEA with experimental data, and to determine the physics behind the length scale parameter. According to the numerical results from Chapter 3, one assumption is that the length scale parameter is a material property and it might be related to the width of the diffuse damage band. However, more studies are required to determine the source of the length scale parameter, and its value for different materials.

As it has already been discussed, even in nominally similar samples the crack paths are different. These differences can be attributed to changes in the microscale, existing defects, and uncertainty in the experimental setup. Consequently, the focus of any fracture simulation should not be to predict the exact crack path of an experimental sample (which can vary from one sample to another), but to predict the average behavior of a large number of test specimens. In order to accomplish this, one can acquire probabilistic approaches where one can predict the probability of a crack propagating in a certain direction instead of the exact crack paths. The network representation of GraFEA makes it a suitable platform for implementation of probabilistic approaches.

REFERENCES

[1] A. A. Griffith, "The phenomena of rupture and flow in solids," *Philosophical transactions of the royal society of london. Series A, containing papers of a mathematical or physical character*, vol. 221, pp. 163 – 198, 1921.

[2] G. Bansal, W. Duckworth, and D. Niesz, "Strength analysis of brittle materials," tech. rep., BATTELLE COLUMBUS DIV OH, 1977. Final rept. Apr 1973 – Oct 1977.

[3] B. Bergman, "On the variability of the fracture stress of brittle materials," *Journal of materials science letters*, vol. 4, no. 9, pp. 1143 – 1146, 1985.

[4] A. d. S. Jayatilaka and K. Trustrum, "Statistical approach to brittle fracture," *Journal of Materials Science*, vol. 12, no. 7, pp. 1426 – 1430, 1977.

[5] L. M. Kachanov, "Time of the rupture process under creep conditions," *Isv. Akad. Nauk. SSR. Otd Tekh. Nauk*, vol. 8, pp. 26 – 31, 1958.

[6] D. Krajcinovic and G. U. Fonseka, "The continuous damage theory of brittle materials, part 1: general theory," *Journal of applied Mechanics*, vol. 48, no. 4, pp. 809 – 815, 1981.

[7] X.-P. Xu and A. Needleman, "Numerical simulations of fast crack growth in brittle solids," *Journal of the Mechanics and Physics of Solids*, vol. 42, no. 9, pp. 1397 – 1434, 1994.

[8] G. T. Camacho and M. Ortiz, "Computational modelling of impact damage in brittle materials," *International Journal of solids and structures*, vol. 33, no. 20-22, pp. 2899–2938, 1996.

[9] T. Belytschko and T. Black, "Elastic crack growth in finite elements with minimal remeshing," *International Journal for Numerical Methods in Engineering*, vol. 45, no. 5, pp. 601 – 620, 1999.

[10] N. Moës, J. Dolbow, and T. Belytschko, "A finite element method for crack growth without remeshing," *International Journal for Numerical Methods in Engineering*, vol. 46, no. 1, pp. 131 – 150, 1999.

[11] N. Moës and T. Belytschko, "Extended finite element method for cohesive crack growth," *Engineering Fracture Mechanics*, vol. 69, no. 7, pp. 813 – 833, 2002.

[12] G. B. Sinclair, "Stress singularities in classical elasticity – i : Removal, interpretation, and analysis," *Applied Mechanics Reviews*, vol. 57, no. 4, pp. 251 – 298, 2004.

[13] S. A. Silling, "Reformulation of elasticity theory for discontinuities and long-range forces," *Journal of the Mechanics and Physics of Solids*, vol. 48, no. 1, pp. 175 – 209, 2000.

[14] A. E. H. Love, *A treatise on the mathematical theory of elasticity, Dover Publications*. Dover Publications, 1944.

[15] P. Khodabakhshi, J. N. Reddy, and A. Srinivasa, "GraFEA: a graph-based finite element approach for the study of damage and fracture in brittle materials," *Meccanica*, vol. 51, no. 12, pp. 3129 – 3147, 2016.

[16] J. N. Reddy and A. R. Srinivasa, "On the force-displacement characteristics of finite elements for elasticity and related problems," *Finite Elements in Analysis and Design*, vol. 104, pp. 35 – 40, 2015.

[17] W. Weibull, "A statistical theory of the strength of materials," *Ingeniors Vetenskaps Akademien*, 1939.

[18] S. B. Badtorf and H. L. Heinisch, "Weakest link theory reformulated for arbitrary fracture criterion," *Journal of the American Ceramic Society*, vol. 61, no. 7-8, pp. 355 – 358, 1978.

[19] S.-D. Pang, Z. P. Bažant, and J.-L. Le, "Statistics of strength of ceramics: finite weakest-link model and necessity of zero threshold," *International Journal of Fracture*, vol. 154, no. 1, pp. 131 – 145, 2008.

[20] R. Ritchie, J. Knott, and J. Rice, "On the relationship between critical tensile stress and fracture toughness in mild steel," *Journal of the Mechanics and Physics of Solids*, vol. 21, no. 6, pp. 395 – 410, 1973.

[21] T. Lin, A. G. Evans, and R. O. Ritchie, "A statistical model of brittle fracture by transgranular cleavage," *Journal of the Mechanics and Physics of Solids*, vol. 34, no. 5, pp. 477 – 497, 1986.

[22] A. C. Eringen, "Theory of nonlocal elasticity and some applications," *Res mechanica*, vol. 21, no. 4, pp. 313 – 342, 1987.

[23] G. R. Irwin and D. C. Washington, "Analysis of stresses and strains near the end of a crack traversing a plate," *ASME Journal of Applied Mechanics*, vol. 24, pp. 361 – 364, 1957.

[24] G. I. Barenblatt, "Concerning equilibrium cracks forming during brittle fracture. the stability of isolated cracks. relationships with energetic theories," *Journal of Applied Mathematics and Mechanics*, vol. 23, no. 5, pp. 1273 – 1282, 1959.

[25] W. F. Brace, "An extension of the Griffith theory of fracture to rocks," *Journal of Geophysical Research*, vol. 65, no. 10, pp. 3477 – 3480, 1960.

[26] D. S. Dugdale, "Yielding of steel sheets containing slits," *Journal of the Mechanics and Physics of Solids*, vol. 8, no. 2, pp. 100 – 104, 1960.

[27] G. I. Barenblatt, "The mathematical theory of equilibrium cracks in brittle fracture," *Advances in applied mechanics*, vol. 7, no. C, pp. 55 – 129, 1962.

[28] G. R. Irwin and A. A. Wells, "A continuum-mechanics view of crack propagation," *Metallurgical Reviews*, vol. 10, no. 1, pp. 223 – 270, 1965.

[29] J. R. Willis, "A comparison of the fracture criteria of Griffith and Barenblatt," *Journal of the Mechanics and Physics of Solids*, vol. 15, no. 3, pp. 151 – 162, 1967.

[30] H. Tada, P. C. Paris, and G. R. Irwin, "The stress analysis of cracks," *Del Research Corp, Hellertown PA*, 1973.

[31] R. Talreja, "A continuum mechanics characterization of damage in composite materials," in *Proceedings of the Royal Society of London A: Mathematical, Physical and Engineering Sciences*, vol. 399, pp. 195 – 216, The Royal Society, 1985.

[32] J. L. Chaboche, "Continuum damage mechanics: Part I—general concepts," *Journal of Applied Mechanics*, vol. 55, pp. 59 – 64, 1988.

[33] J. L. Chaboche, "Continuum damage mechanics: Part II—damage growth, crack initiation, and crack growth," *Journal of Applied Mechanics*, vol. 55, pp. 65 – 72, 1988.

[34] J. S. Marshall, P. M. Naghdi, and A. R. Srinivasa, "A macroscopic theory of microcrack growth in brittle materials," *Philosophical Transactions of the Royal Society of London A: Mathematical, Physical and Engineering Sciences*, vol. 335, no. 1639, pp. 455 – 485, 1991.

[35] Z. P. Bažant and M. Jirásek, "Nonlocal integral formulations of plasticity and damage: survey of progress," *Journal of Engineering Mechanics*, vol. 128, no. 11, pp. 1119 – 1149, 2002.

[36] T.-P. Fries and T. Belytschko, "The extended/generalized finite element method: an overview of the method and its applications," *International Journal for Numerical Methods in Engineering*, vol. 84, no. 3, pp. 253 – 304, 2010.

[37] K. Park and G. H. Paulino, "Cohesive zone models: A critical review of traction-separation relationships across fracture surfaces," *Applied Mechanics Reviews*, vol. 64, no. 6, pp. 060802: 1 – 20, 2011.

[38] A. Needleman, "Some issues in cohesive surface modeling," *Procedia {IUTAM}*, vol. 10, no. 0, pp. 221 – 246, 2014.

[39] E. Schlangen and J. G. M. Van Mier, "Simple lattice model for numerical simulation of fracture of concrete materials and structures," *Materials and Structures*, vol. 25, no. 9, pp. 534 – 542, 1992.

[40] M. Ostoja-Starzewski, "Lattice models in micromechanics," *Applied Mechanics Reviews*, vol. 55, no. 1, pp. 35 – 60, 2002.

[41] M. Yip, Z. Li, B.-S. Liao, and J. E. Bolander, "Irregular lattice models of fracture of multi-phase particulate materials," *International journal of fracture*, vol. 140, no. 1 – 4, pp. 113 – 124, 2006.

[42] L. Kosteski, I. Iturrioz, R. G. Batista, and A. P. Cisilino, "The truss–like discrete element method in fracture and damage mechanics," *Engineering Computations*, vol. 28, no. 6, pp. 765 – 787, 2011.

[43] L. Kosteski, R. Barrios D'Ambra, and I. Iturrioz, "Crack propagation in elastic solids using the truss-like discrete element method," *International Journal of Fracture*, vol. 174, no. 2, pp. 139 – 161, 2012.

[44] R. W. Macek and S. A. Silling, "Peridynamics via finite element analysis," *Finite Elements in Analysis and Design*, vol. 43, no. 15, pp. 1169 – 1178, 2007.

[45] B. Kilic and E. Madenci, "Coupling of peridynamic theory and the finite element method," *Journal of Mechanics of Materials and Structures*, vol. 5, no. 5, pp. 707 – 733, 2010.

[46] J. A. Mitchell, "A nonlocal, ordinary, state-based plasticity model for peridynamics," *SANDIA Report*, vol. 3166, 2011.

[47] J. Xu, A. Askari, O. Weckner, and S. Silling, "Peridynamic analysis of impact damage in composite laminates," *Journal of Aerospace Engineering*, vol. 21, no. 3, pp. 187 – 194, 2008.

[48] B. Kilic, A. Agwai, and E. Madenci, "Peridynamic theory for progressive damage prediction in center-cracked composite laminates," *Composite Structures*, vol. 90, no. 2, pp. 141 – 151, 2009.

[49] Y. D. Ha and F. Bobaru, "Studies of dynamic crack propagation and crack branching with peridynamics," *International Journal of Fracture*, vol. 162, no. 1, pp. 229 – 244, 2010.

[50] Y. D. Ha and F. Bobaru, "Characteristics of dynamic brittle fracture captured with peridynamics," *Engineering Fracture Mechanics*, vol. 78, no. 6, pp. 1156 – 1168, 2011.

[51] J. N. Reddy, *An Introduction to the Finite Element Method*. New York, NY: McGraw Hill, 2006.

[52] F. Reusch, B. Svendsen, and D. Klingbeil, "Local and non-local Gurson-based ductile damage and failure modelling at large deformation," *European Journal of Mechanics - A/Solids*, vol. 22, no. 6, pp. 779 – 792, 2003.

[53] D. Lasry and T. Belytschko, "Localization limiters in transient problems," *International Journal of Solids and Structures*, vol. 24, no. 6, pp. 581 – 597, 1988.

[54] Z. P. Bažant, "Instability, ductility and size effect in strain–softening concrete," *Journal of the Engineering Mechanics Division, ASCE*, vol. 102, pp. 331 – 344, 1975.

[55] Z. P. Bažant and L. Cedolin, "Finite element modeling of crack band propagation," *Journal of Structural Engineering*, vol. 109, no. 1, pp. 69 – 92, 1983.

[56] Z. P. Bažant and B. H. Oh, "Crack band theory for fracture of concrete," *Matériaux et Construction*, vol. 16, no. 3, pp. 155 – 177, 1983.

[57] A. Needleman, "Material rate dependence and mesh sensitivity in localization problems," *Computer Methods in Applied Mechanics and Engineering*, vol. 67, no. 1, pp. 69 – 85, 1988.

[58] Z. P. Bažant and G. Pijaudier-Cabot, "Nonlocal continuum damage, localization instability and convergence," *Journal of applied mechanics*, vol. 55, no. 2, pp. 287–293, 1988.

[59] N. Triantafyllidis and E. C. Aifantis, "A gradient approach to localization of deformation. i. hyperelastic materials," *Journal of Elasticity*, vol. 16, no. 3, pp. 225 – 237, 1986.

[60] R. Peerlings, R. De Borst, W. Brekelmans, and M. Geers, "Localisation issues in local and nonlocal continuum approaches to fracture," *European Journal of Mechanics – A/Solids*, vol. 21, no. 2, pp. 175 – 189, 2002.

[61] R. H. J. Peerlings, M. G. D. Geers, R. De Borst, and W. A. M. Brekelmans, "A critical comparison of nonlocal and gradient-enhanced softening continua," *International Journal of solids and Structures*, vol. 38, no. 44, pp. 7723 – 7746, 2001.

[62] Z. P. Bažant, T. B. Belytschko, and C. Ta-Peng, "Continuum theory for strain–softening," *Journal of Engineering Mechanics*, vol. 110, no. 12, pp. 1666–1692, 1984.

[63] T. Belytschko, Z. P. Bažant, H. Yul-Woong, and C. Ta-Peng, "Strain–softening materials and finite-element solutions," *Computers & Structures*, vol. 23, no. 2, pp. 163 – 180, 1986.

[64] M. Jirásek, "Nonlocal models for damage and fracture: comparison of approaches," *International Journal of Solids and Structures*, vol. 35, no. 31-32, pp. 4133 – 4145, 1998.

[65] N. Challamel and C. M. Wang, "The small length scale effect for a non-local cantilever beam: a paradox solved," *Nanotechnology*, vol. 19, no. 34, p. 345703(7), 2008.

[66] N. Challamel, "Variational formulation of gradient or/and nonlocal higher-order shear elasticity beams," *Composite Structures*, vol. 105, no. Supplement C, pp. 351 – 368, 2013.

[67] J.-H. Song, H. Wang, and T. Belytschko, "A comparative study on finite element methods for dynamic fracture," *Computational Mechanics*, vol. 42, no. 2, pp. 239 – 250, 2008.

[68] R. de Borst, J. J. C. Remmers, and A. Needleman, "Mesh-independent discrete numerical representations of cohesive-zone models," *Engineering fracture mechanics*, vol. 73, no. 2, pp. 160–177, 2006.

[69] S. A. Silling, M. Epton, O. Weckner, J. Xu, and E. Askari, "Peridynamic states and constitutive modeling," *Journal of Elasticity*, vol. 88, no. 2, pp. 151 – 184, 2007.

[70] S. A. Silling and R. B. Lehoucq, "Convergence of peridynamics to classical elasticity theory," *Journal of Elasticity*, vol. 93, no. 1, pp. 13 – 37, 2008.

[71] E. Emmrich and O. Weckner, "On the well-posedness of the linear peridynamic model and its convergence towards the navier equation of linear elasticity," *Communications in Mathematical Sciences*, vol. 5, pp. 851 – 864, 12 2007.

[72] T. Mengesha and Q. Du, "Nonlocal constrained value problems for a linear peridynamic navier equation," *Journal of Elasticity*, vol. 116, no. 1, pp. 27 – 51, 2014.

[73] P. Seleson, Q. Du, and M. L. Parks, "On the consistency between nearest-neighbor peridynamic discretizations and discretized classical elasticity models," *Computer Methods in Applied Mechanics and Engineering*, vol. 311, pp. 698 – 722, 2016.

[74] X. Tian and Q. Du, "Analysis and comparison of different approximations to nonlocal diffusion and linear peridynamic equations," *SIAM Journal on Numerical Analysis*, vol. 51, no. 6, pp. 3458 – 3482, 2013.

[75] P. D. Seleson, *Peridynamic multi scale models for the mechanics of materials: Cconstitutive relations, upscaling from atomistic systems, and interface problems*. PhD thesis, Florida State university, 2010.

[76] S. F. Henke and S. Shanbhag, "Mesh sensitivity in peridynamic simulations," *Computer Physics Communications*, vol. 185, no. 1, pp. 181 – 193, 2014.

[77] P. Seleson and M. Parks, "On the role of the influence function in the peridynamic theory," *International Journal for Multiscale Computational Engineering*, vol. 9, no. 6, pp. 689 – 706, 2011.

[78] F. Bobaru and G. Zhang, "Why do cracks branch? A peridynamic investigation of dynamic brittle fracture," *International Journal of Fracture*, vol. 196, no. 1, pp. 59 – 98, 2015.

[79] D. Dipasquale, G. Sarego, M. Zaccariotto, and U. Galvanetto, "Dependence of crack paths on the orientation of regular 2d peridynamic grids," *Engineering Fracture Mechanics*, vol. 160, pp. 248 – 263, 2016.

[80] M. Ghajari, L. Iannucci, and P. Curtis, "A peridynamic material model for the analysis of dynamic crack propagation in orthotropic media," *Computer Methods in Applied Mechanics and Engineering*, vol. 276, pp. 431 – 452, 2014.

[81] W. Hu, Y. D. Ha, and F. Bobaru, "Peridynamic model for dynamic fracture in unidirectional fiber-reinforced composites," *Computer Methods in Applied Mechanics and Engineering*, vol. 217–220, pp. 247 – 261, 2012.

[82] Y. Mao, B. Talamini, and L. Anand, "Rupture of polymers by chain scission," *Extreme Mechanics Letters*, vol. 13, pp. 17 – 24, 2017.

[83] G. Pijaudier-Cabot and Z. P. Bažant, "Nonlocal damage theory," *Journal of engineering mechanics*, vol. 113, no. 10, pp. 1512 – 1533, 1987.

[84] J. N. Reddy, *An Introduction to Continuum Mechanics, Second Edition*. New York, NY: Cambridge University Press, 2013.

[85] E. Kröner, "Elasticity theory of materials with long range cohesive forces," *International Journal of Solids and Structures*, vol. 3, no. 5, pp. 731 – 742, 1967.

[86] J. A. Krumhansl, "Some considerations of the relation between solid state physics and generalized continuum mechanics," in *Mechanics of Generalized Continua* (E. Kröner, ed.), IUTAM Symposia, pp. 298 – 311, Springer Berlin Heidelberg, 1968.

[87] I. A. Kunin, "The theory of elastic media with microstructure and the theory of dislocations," in *Mechanics of Generalized Continua* (E. Kröner, ed.), IUTAM Symposia, pp. 321 – 329, Springer Berlin Heidelberg, 1968.

[88] A. C. Eringen, "Nonlocal polar elastic continua," *International Journal of Engineering Science*, vol. 10, no. 1, pp. 1 – 16, 1972.

[89] A. C. Eringen, "Linear theory of nonlocal elasticity and dispersion of plane waves," *International Journal of Engineering Science*, vol. 10, no. 5, pp. 425 – 435, 1972.

[90] A. C. Eringen, "On differential equations of nonlocal elasticity and solutions of screw dislocation and surface waves," *Journal of Applied Physics*, vol. 54, no. 9, pp. 4703 – 4710, 1983.

[91] A. C. Eringen, *Nonlocal Continuum Field Theories.* New York, NY: Springer, 2002.

[92] A. C. Eringen and D. G. B. Edelen, "On nonlocal elasticity," *International Journal of Engineering Science*, vol. 10, no. 3, pp. 233 – 248, 1972.

[93] J. Peddieson, G. R. Buchanan, and R. P. McNitt, "Application of nonlocal continuum models to nanotechnology," *International Journal of Engineering Science*, vol. 41, no. 3–5, pp. 305 – 312, 2003.

[94] R. S. Pereira, "Atomic force microscopy as a novel pharmacological tool," *Biochemical Pharmacology*, vol. 62, no. 8, pp. 975 – 983, 2001.

[95] J. Pei, F. Tian, and T. Thundat, "Glucose biosensor based on the microcantilever," *Analytical Chemistry*, vol. 76, no. 2, pp. 292 – 297, 2004.

[96] K. L. Ekinci and M. L. Roukes, "Nanoelectromechanical systems," *Review of Scientific Instruments*, vol. 76, no. 6, p. 061101(12), 2005.

[97] M. J. S. N. V. Lavrik and P. G. Datskos, "Cantilever transducers as a platform for chemical and biological sensors," *Review of Scientific Instruments*, vol. 75, no. 7, pp. 2229 – 2253, 2004.

[98] L. J. Sudak, "Column buckling of multiwalled carbon nanotubes using nonlocal continuum mechanics," *Journal of Applied Physics*, vol. 94, no. 11, pp. 7281 – 7287, 2003.

[99] P. Lu, H. P. Lee, C. Lu, and P. Q. Zhang, "Dynamic properties of flexural beams using a nonlocal elasticity model," *Journal of Applied Physics*, vol. 99, no. 7, p. 073510(9), 2006.

[100] A. Shakouri, R. M. Lin, and T. Y. Ng, "Free flexural vibration studies of double-walled carbon nanotubes with different boundary conditions and modeled as nonlocal euler beams via the Galerkin method," *Journal of Applied Physics*, vol. 106, no. 9, p. 094307(10), 2009.

[101] C. M. Wang, Y. Y. Zhang, S. S. Ramesh, and S. Kitipornchai, "Buckling analysis of micro- and nano-rods/tubes based on nonlocal Timoshenko beam theory," *Journal of Physics D: Applied Physics*, vol. 39, no. 17, pp. 3904 – 3909, 2006.

[102] C. M. Wang, S. Kitipornchai, C. W. Lim, and M. Eisenberger, "Beam bending solutions based on nonlocal Timoshenko beam theory," *Journal of Engineering Mechanics*, vol. 134, no. 6, pp. 475 – 481, 2008.

[103] Q. Wang and C. M. Wang, "The constitutive relation and small scale parameter of nonlocal continuum mechanics for modelling carbon nanotubes," *Nanotechnology*, vol. 18, no. 7, p. 075702(4), 2007.

[104] Q. Wang and K. M. Liew, "Application of nonlocal continuum mechanics to static analysis of micro- and nano-structures," *Physics Letters A*, vol. 363, no. 3, pp. 236 – 242, 2007.

[105] J. N. Reddy, "Nonlocal theories for bending, buckling and vibration of beams," *International Journal of Engineering Science*, vol. 45, no. 2–8, pp. 288 – 307, 2007.

[106] J. N. Reddy, "Nonlocal nonlinear formulations for bending of classical and shear deformation theories of beams and plates," *International Journal of Engineering Science*, vol. 48, no. 11, pp. 1507 – 1518, 2010.

[107] H.-T. Thai, "A nonlocal beam theory for bending, buckling, and vibration of nanobeams," *International Journal of Engineering Science*, vol. 52, no. 0, pp. 56 – 64, 2012.

[108] H.-T. Thai and T. P. Vo, "A nonlocal sinusoidal shear deformation beam theory with application to bending, buckling, and vibration of nanobeams," *International Journal of Engineering Science*, vol. 54, no. 0, pp. 58 – 66, 2012.

[109] J. N. Reddy and S. El-Borgi, "Eringen's nonlocal theories of beams accounting for moderate rotations," *International Journal of Engineering Science*, vol. 82, no. 0, pp. 159 – 177, 2014.

[110] J. N. Reddy, S. El-Borgi, and J. Romanoff, "Non-linear analysis of functionally graded microbeams using Eringen's non-local differential model," *International Journal of Non-Linear Mechanics*, vol. 67, no. 0, pp. 308 – 318, 2014.

[111] O. Rahmani and O. Pedram, "Analysis and modeling the size effect on vibration of functionally graded nanobeams based on nonlocal timoshenko beam theory," *International Journal of Engineering Science*, vol. 77, no. 0, pp. 55 – 70, 2014.

[112] H. Salehipour, A. Shahidi, and H. Nahvi, "Modified nonlocal elasticity theory for functionally graded materials," *International Journal of Engineering Science*, vol. 90, no. 0, pp. 44 – 57, 2015.

[113] C. Polizzotto, "Nonlocal elasticity and related variational principles," *International Journal of Solids and Structures*, vol. 38, no. 42–43, pp. 7359 – 7380, 2001.

[114] A. A. Pisano and P. Fuschi, "Closed form solution for a nonlocal elastic bar in tension," *International Journal of Solids and Structures*, vol. 40, no. 1, pp. 13 – 23, 2003.

[115] A. A. Pisano, A. Sofi, and P. Fuschi, "Nonlocal integral elasticity: 2D finite element based solutions," *International Journal of Solids and Structures*, vol. 46, no. 21, pp. 3836 – 3849, 2009.

[116] M. Di Paola, G. Failla, A. Sofi, and M. Zingales, "A mechanically based approach to non-local beam theories," *International Journal of Mechanical Sciences*, vol. 53, no. 9, pp. 676 – 687, 2011.

[117] N. Challamel, Z. Zhang, C. M. Wang, J. N. Reddy, Q. Wang, T. Michelitsch, and B. Collet, "On nonconservativeness of Eringen's nonlocal elasticity in beam mechanics: Correction from a discrete-based approach," *Archive of Applied Mechanics*, vol. 84, no. 9 – 11, pp. 1275 – 1292, 2014.

[118] B. Arash and Q. Wang, "A review on the application of nonlocal elastic models in modeling of carbon nanotubes and graphenes," *Computational Materials Science*, vol. 51, no. 1, pp. 303 – 313, 2012.

[119] J. N. Reddy, *Energy principles and variational methods in applied mechanics*. John Wiley & Sons, 2017.

[120] C. Li, L. Yao, W. Chen, and S. Li, "Comments on nonlocal effects in nano-cantilever beams," *International Journal of Engineering Science*, vol. 87, no. 0, pp. 47 – 57, 2015.

[121] J. N. Reddy, "A unified integro-differential nonlocal model with application to beams, presentation made at "Nonlocal Models in Mathematics, Computation, Science, and Engineering", Oak Ridege National Laboratory, Tennessee, 26 October 2015," 2015.

[122] R. D. Mindlin, "Second gradient of strain and surface-tension in linear elasticity," *International Journal of Solids and Structures*, vol. 1, no. 4, pp. 417 – 438, 1965.

[123] B. S. Altan and E. C. Aifantis, "On some aspects in the special theory of elasticity," *Journal of the Mechanical Behaviour of Materials*, vol. 8, no. 3, pp. 231 – 282, 1997.

[124] A. R. Srinivasa and J. N. Reddy, "A model for a constrained, finitely deforming, elastic solid with rotation gradient dependent strain energy, and its specialization to von Kármán plates and beams," *Journal of the Mechanics and Physics of Solids*, vol. 61, no. 3, pp. 873 – 885, 2013.

[125] F. Yang, A. C. M. Chong, D. C. C. Lam, and P. Tong, "Couple stress based strain gradient theory for elasticity," *International Journal of Solids and Structures*, vol. 39, no. 10, pp. 2731 – 2743, 2002.

[126] J. N. Reddy, "Microstructure-dependent couple stress theories of functionally graded beams," *Journal of the Mechanics and Physics of Solids*, vol. 59, no. 11, pp. 2382 – 2399, 2011.

[127] J. N. Reddy and A. Arbind, "Bending relationships between the modified couple stress-based functionally graded Timoshenko beams and homogeneous Bernoulli–Euler beams," *Annals of Solid and Structural Mechanics*, vol. 3, no. 1 – 2, pp. 15 – 26, 2012.

[128] A. Arbind and J. N. Reddy, "Nonlinear analysis of functionally graded microstructure-dependent beams," *Composite Structures*, vol. 98, pp. 272 – 281, 2013.

[129] J. N. Reddy, A. Srinivasa, A. Arbind, and P. Khodabakhshi, "On gradient elasticity and discrete peridynamics with applications to beams and plates," *Advanced Materials Research*, vol. 745, pp. 145 – 154, 2013.

[130] J. N. Reddy and J. Kim, "A nonlinear modified couple stress-based third-order theory of functionally graded plates," *Composite Structures*, vol. 94, no. 3, pp. 1128 – 1143, 2012.

[131] P. Khodabakhshi and J. N. Reddy, "A unified integro-differential nonlocal model," *International Journal of Engineering Science*, vol. 95, pp. 60 – 75, 2015.

[132] R. D. Mindlin and N. N. Eshel, "On first strain-gradient theories in linear elasticity," *International Journal of Solids and Structures*, vol. 4, no. 1, pp. 109 – 124, 1968.

[133] P. Casal, "La theorie du second gradient et la capillarite," *C. R. Acad. Sci.*, vol. A(724), pp. 1571 – 1574, 1972.

[134] D. C. C. Lam, F. Yang, A. C. M. Chong, J. Wang, and P. Tong, "Experiments and theory in strain gradient elasticity," *Journal of the Mechanics and Physics of Solids*, vol. 51, no. 8, pp. 1477 – 1508, 2003.

[135] X. L. Gao and S. K. Park, "Variational formulation of a simplified strain gradient elasticity theory and its application to a pressurized thick-walled cylinder problem," *International Journal of Solids and Structures*, vol. 44, no. 22 – 23, pp. 7486 – 7499, 2007.

[136] B. Akgöz and Ö. Civalek, "Application of strain gradient elasticity theory for buckling analysis of protein microtubules," *Current Applied Physics*, vol. 11, no. 5, pp. 1133 – 1138, 2011.

[137] X. Liang, S. Hu, and S. Shen, "A new Bernoulli–Euler beam model based on a simplified strain gradient elasticity theory and its applications," *Composite Structures*, vol. 111, pp. 317 – 323, 2014.

[138] K. Lazopoulos and A. Lazopoulos, "Bending and buckling of thin strain gradient elastic beams," *European Journal of Mechanics - A/Solids*, vol. 29, no. 5, pp. 837 – 843, 2010.

[139] B. Wang, M. Liu, J. Zhao, and S. Zhou, "A size-dependent Reddy–Levinson beam model based on a strain gradient elasticity theory," *Meccanica*, vol. 49, no. 6, pp. 1427 – 1441, 2014.

[140] B. Akgöz and Ö. Civalek, "Buckling analysis of functionally graded microbeams based on the strain gradient theory," *Acta Mechanica*, vol. 224, no. 9, pp. 2185 – 2201, 2013.

[141] R. Ansari, R. Gholami, and S. Sahmani, "Size-dependent vibration of functionally graded curved microbeams based on the modified strain gradient elasticity theory," *Archive of Applied Mechanics*, vol. 83, no. 10, pp. 1439 – 1449, 2013.

[142] S. Ramezani, "A micro scale geometrically non-linear Timoshenko beam model based on strain gradient elasticity theory," *International Journal of Non-Linear Mechanics*, vol. 47, no. 8, pp. 863 – 873, 2012.

[143] C. W. Lim, G. Zhang, and J. N. Reddy, "A higher-order nonlocal elasticity and strain gradient theory and its applications in wave propagation," *Journal of the Mechanics and Physics of Solids*, vol. 78, pp. 298 – 313, 2015.

[144] S. T. Yaghoubi, S. M. Mousavi, and J. Paavola, "Strain and velocity gradient theory for higher-order shear deformable beams," *Archive of Applied Mechanics*, vol. 85, no. 7, pp. 877 – 892, 2015.

[145] S. M. Mousavi, J. Paavola, and J. Reddy, "Variational approach to dynamic analysis of third-order shear deformable plates within gradient elasticity," *Meccanica*, vol. 50, no. 6, pp. 1537 – 1550, 2015.

[146] X. Li, B. Bhushan, K. Takashima, C.-W. Baek, and Y.-K. Kim, "Mechanical characterization of micro/nanoscale structures for MEMS/NEMS applications using nanoindentation techniques," *Ultramicroscopy*, vol. 97, no. 1 – 4, pp. 481 – 494, 2003. Proceedings of the Fourth International Conference on Scanning Probe Microscopy, Sensors and Nanostructures.

[147] J. N. Reddy, "A simple higher-order theory for laminated composite plates," *Journal of Applied Mechanics, ASME*, vol. 51, no. 4, pp. 747 – 752, 1984.

[148] A. Arbind, J. Reddy, and A. R. Srinivasa, "Modified couple stress-based third-order theory for nonlinear analysis of functionally graded beams," *Latin American Journal of Solids and Structures*, vol. 11, pp. 459 – 487, 05 2014.

[149] J. N. Reddy and A. Srinivasa, "Nonlinear theories of beams and plates accounting for moderate rotations and material length scales," *International Journal of Non-Linear Mechanics*, vol. 66, pp. 43 – 53, 2014.

[150] J. N. Reddy, *An Introduction to Nonlinear Finite Element Analysis: with applications to heat transfer, fluid mechanics, and solid mechanics*. Oxford University Press, 2015.